MULTISCALE SIMULATION OF FAILURE BASED ON SPACE-TIME FINITE ELEMENT METHOD AND NON-ORDINARY STATE-BASED PERIDYNAMICS

by

Shogo Wada

APPROVED BY SUPERVISORY COMMITTEE:

____
Dong Qian, Chair

____
Hongbing Lu

____
Walter E. Voit

____
Ill Ryu

MULTISCALE SIMULATION OF FAILURE BASED ON SPACE-TIME FINITE ELEMENT METHOD AND NON-ORDINARY STATE-BASED PERIDYNAMICS

by

SHOGO WADA, BS, MS

DISSERTATION

Presented to the Faculty of

The University of Texas at Dallas

in Partial Fulfillment

of the Requirements

for the Degree of

DOCTOR OF PHILOSOPHY IN

MECHANICAL ENGINEERING

THE UNIVERSITY OF TEXAS AT DALLAS

December 2017

ACKNOWLEDGMENTS

First of all, I would like to thank my advisor, Dr. Dong Qian for his great support in this work. In the fall of 2014, I joined his group as an international student. From that day on, he has encouraged and motivated me constantly. I could not have accomplished this goal without his great help. I am sincerely grateful for the opportunity of working with him.

I really appreciate the encouragement from my research committee members, Dr. Hongbing Lu, Dr. Walter E. Voit and Dr. Ill Ryu. They have given amazing advice from the different perspectives of my concentration area. From their advice, I got an opportunity to do some experimental work to verify my computational results and further enhance my work.

I would like to thank The University of Texas at Dallas for the great curriculum and financial support. I have learned so many things through the Mechanical Engineering PhD course work and this acquired knowledge became the foundation of my research work. I also appreciate help and friendship given by all my colleagues, especially Dr. Zhong Zhou, Dr. Wenwei Jiang, Clint Nicely, Mohammad Karim Rezaul, Rui Zhang, Yang Wang, Dr. Tao Zhang, Dr. Hossein Pourmatin, Tingge Xu, Xuemin Wang, Xaowei Zhu, Kim Ha Eun, and Satish Krishnasamy Radha.

I sincerely acknowledge a graduate fellowship from the Bridgestone Corporation in Japan. Thanks to the financial support, I was able to focus on my research work without any concern. I am ready to work for Bridgestone in the area of the safe tire applications for automobiles. Again, I would like to thank Bridgestone Corporation for trusting me and giving me the opportunity to study in the United States.

Finally, I thank my parents and three brothers for raising me up and encouraging me to pursue a productive career. I could not reach this stage in my life without their help. I also thank my wife Yu and our twins Chiyoharu and Chiyona. They make my life brilliant and I cannot imagine a life without my family.

September 2017

MULTISCALE SIMULATION OF FAILURE BASED ON SPACE-TIME FINITE ELEMENT METHOD AND NON-ORDINARY STATE-BASED PERIDYNAMICS

Shogo Wada, PhD
The University of Texas at Dallas, 2017

Supervising Professor: Dong Qian

Engineering materials such as rubbers are widely used in industrial applications and are often exposed to cyclic stress and strain conditions while in service. To ensure safety and reliability, quantifying the effect of loads on the life is an important but challenging task, due to the combination of geometric/material nonlinearities and loading conditions for extended time durations. In this work, a novel simulation-based approach based on space-time finite element method (FEM) is presented with a goal to capture fatigue failure in rubbery material subjected to cyclic loads and dynamic fracture in general elastic solids. It is established by integrating the time discontinuous Galerkin (TDG) formulation with either nonlinear material constitutive laws or peridynamics models.

In the first implementation, nonlinear space-time FEM framework is established and integrated with a continuum damage mechanics (CDM) model to account for the damage evolution due to cyclic loading. CDM parameters for synthetic rubber are calibrated based on fatigue experiment. The nonlinear system in space-time FEM is solved using Newton's method in which the system Jacobian is approximated with a finite difference approach. The developed approach is then

employed to solve a set of benchmark problems involving fracture and low cycle fatigue in rubber. Additional tests on notched rubber sheet specimen are carried out to validate the simulation predictions. The simulation predictions yield good agreement with the tests. In addition, it is shown that responses to fatigue load with 10^6 cycles can be captured using the proposed approach.

In the second case, a multiscale method that couples the space-time FEM based on the time discontinuous Galerkin method with non-ordinary state-based peridynamics (NOPD) is developed for dynamic fracture simulation. A concurrent coupling scheme is presented for the coupling, in which the whole domain is discretized by finite elements, and a local domain of interest is simulated with NOPD. The space-time FEM approach allows flexible choice of time step size and this makes the computation more effective. As a meshfree method, NOPD is introduced as a fine scale representation to capture the initiation and propagation of the crack. Through coupling to space-time FEM, NOPD simulation domain moves with the propagating crack front, leading to an adaptive multiscale simulation scheme. The robustness of this methodology is demonstrated through examples of a linear elastic material, in which comparisons are made to the full scale NOPD simulation.

In summary, the proposed space-time approach introduces the key capability to establish approximations in the temporal domain, thus enabling prediction of nonlinear responses that are strongly time-dependent. This is demonstrated in two cases in this dissertation: the first involves fatigue failure prediction at extended time scale, and the second deals with dynamic fracture at small time scale. Based on the implementation and results, it is concluded the established space-time FEM framework is both efficient and accurate, and overcomes the critical limit of the traditional FEM approach using semi-discrete time integration schemes. The presented framework is ideal for many engineering problems featured by a multitude of temporal scales.

TABLE OF CONTENTS

LIST OF FIGURES

LIST OF TABLES

CHAPTER 1

INTRODUCTION

1.1 Background and motivation

1.1.1 Constitutive model and damage model of rubber

Rubbery materials are widely used in industrial products such as tire, engine mount, seismic isolation rubber, sealing, medical equipment etc. The special properties of rubber (large deformation, incompressibility, rate-temperature dependency, stress-strain hysteresis, etc.) cannot be easily replaced by other materials. Under operating environments, parts made of rubber can be subjected to cyclic stress and strain conditions over extended time period. As such, durability is an important aspect in the design of rubber. As an example, a standard automotive tire is a composite that consists of rubber, steel wire and textile and the resultant stress-strain history inside the tire is complex. Failure modes of the tire that initiate from the edge or interface of the reinforcements have been reported [1]. A general review on fatigue failure in rubbery materials can be found in Mars and Fatemi [2].

Fatigue life prediction in rubbery materials is a challenging task due to the lack of understanding on the controlling mechanisms. Most of the life prediction tools employed by the industry today are heavily empirical in nature. They can be broadly classified into two categories based on the parameters chosen to calculate fatigue life, i.e., models based on fatigue crack initiation/propagation (FCIP) and cumulative fatigue damage (CFD). A comprehensive review on the fatigue life prediction models for rubbery materials can be found in Mars and Fatemi [3]. In FCIP approach, maximum principal strain or strain energy density are widely used as the criteria for fatigue failure. As an example, Fielding [4] showed the relationship between uniaxial strain and fatigue life of synthetic rubber. On the other hand, the fatigue crack growth approach is mainly based on strain energy release rate [5, 6] or J-integral [7]. Mars and Fatemi [3] summarized both crack nucleation and growth approaches. In CFD approach, continuum damage mechanics (CDM) theory is introduced in which it is assumed that the internal damage variable is accumulated due to cyclic load. Lemaitre [8] developed this concept for ductile failure of metals. Cantournet and Desmorat et al [9, 10] applied CDM for modelling Mullins effect [11] and cyclic softening of elastomers. For the fatigue life of rubber, Wang et al [12] proposed CDM model as a function of strain amplitude.

To handle the large and highly nonlinear deformation of elastomers while subjected to cyclic loads, numerous constitutive models have been established [13]. Isotropic hyperelastic model have been commonly introduced for rubber in which the strain energy is expressed as a function of the three principal invariants of the Cauchy Green deformation tensor, given as I_1, I_2 and I_3. In this context, Neo-Hookean material model is the simplest form and it can be regarded as an extension of Hooke's law to large deformation. A polynomial form involving the principal invariants was introduced in Rivlin and Saunders [14]. Mooney-Rivlin model [14, 15] is also a standard model that has been widely used for the modeling of rubber. It is described as a combination of first order terms of I_1 and I_2. In Yeoh's model [16], the strain energy potential is a cubic form of the first invariant. Ogden [17, 18] extended the polynomial form of the strain energy by using the summation of non-integer order principal stretches. Arruda and Boyce [19] proposed the stretch based model known as the 8-chain model. Because of incompressibility of the rubber, the volume ratio is theoretically assumed to be one in these hyperelastic models. To enforce the incompressibility constraint, methods of modifying the hyperelastic models have been developed and used [20–22]. In some applications, viscoelastic properties of rubber must also be considered. Simo [23] developed finite strain viscoelastic theory by extending the linear viscoelasticity model. With this formulation, arbitrary hyperelastic material models can be incorporated.

While a great deal of efforts has been devoted to fatigue modeling, relatively little progress has been made towards direct numerical simulation (DNS) of fatigue failure in rubbery materials. The challenges in establishing the DNS tools are mainly due to the temporal scales associated with the application. Fatigue failure in rubber may take from a few thousands to millions of load cycles, Traditional computational tool such as the finite element method (FEM) based on semi-discrete schemes is not well suited for these types of analysis as it lacks the flexibility in establishing approximations in the temporal domain. Semi-discrete time integration schemes such as the center difference or Newmark-β methods are known to suffer from either the time-step constraints or lack of convergence due to the oscillatory nature of the fatigue loading condition. As such, simulating loading conditions with cycles on the order of hundreds of thousands and beyond is generally an impractical task for FEM. On the other hand, there is a great demand for such a computational capability as factors such as stress history and triaxiality, nonlinear coupling among the loads, complex geometry are known to critically influence the fatigue failure in rubber and generally not fully accounted for in the empirical design approaches that are in practice today. In this dissertation, a study is presented on the application of the space-time FEM formulation for failure problems such as due to fatigue. A brief review on the formulation is outlined next.

1.1.2 Space-time FEM

Generally, finite difference approach such as explicit and implicit methods are used for the temporal integration of finite element analysis. These implementations are also referred to as semi-discrete scheme in conventional FEM since only the spatial domain is discretized by finite element mesh. On the other hand, both spatial and temporal domains are discretized and space-time shape function is introduced in space-time FEM. The idea to discretize both spatial and temporal domain had been introduced by Argyris and Scharpf [24], Fried [25] and Oden [26] and this formulation is also called as the time continuous Galerkin (TCG) formulation. An alternative approach is known as time discontinuous Galerkin (TDG) formulation. TDG formulation was introduced by Reed and Hill [27] and Lesaint and Raviart [28] to solve the neuron transport equation. Extensions to solve solid mechanics problems were made in [29–33]. It has been shown that TDG based formulation is both A-stable and higher-order accurate [29, 30]. These works have demonstrated that TDG formulation significantly reduces the artificial oscillations that are commonly associated with semi-discrete time integration schemes in capturing sharp gradients or discontinuities. More recently, it has been proposed that the convergence properties of the regular space-time FEM can be further enhanced by introducing enrichment functions that represents the problem physics [34, 35]. This enriched formulation is referred to as the extended space-time finite element method (XTFEM) [36]. The robustness of XTFEM has been demonstrated in the context of coupled atomistic-continuum simulations of fracture [37], wave dynamics [38] and high cycle fatigue failure in metals [39, 40].

1.1.3 Literature review of peridynamics

In the fracture simulation, prediction of crack initiation and propagation is still a challenging topic though various kinds of computational modeling based on FEM have been developed and applied in recent years [41]. For example, the simplest implementation is the element deletion method. Another way of modeling crack is the inter-element crack method. In this method, cohesive law is prescribed between elements to express the crack separation [42, 43]. Generally, the disadvantage of these fracture simulation based on FEM is that the mesh structure heavily affects the crack path choice and the spatial partial derivative in the theory loses accuracy around the discontinuity coming from cracks. The extended finite element method (XFEM) is originally developed by Belytschko and Black [44] and Moës et al [45]. In XTFEM framework, the enrichment shape function and additional degree of freedoms are introduced to represent the discontinuity at the crack pass. XFEM is innovative approach to express cracks in FEM framework, however, using XFEM for capturing propagation process of multiple and complicated cracks is still an ongoing research topic.

Peridynamics formulation was originally developed by Silling [46] and is a reformulation of the classical continuum theory based on an integral form. Compared with FEM based methods, evaluations of the spatial derivatives are not required in peridynamic equation of motion because of the integral formulation. Peridynamics is nonlocal particle theory and rewriting of the equation of motion is done based of the concept nonlocality. In peridynamic theory, the state of material point is determined by itself and other material points within a constant distance region called horizon and the set of material points is called family. Figure 1 illustrates the horizon and family in peridynamics modeling. In peridynamics formulation, the bond is defined between the material point and a member of its family. Spatial discontinuity like a crack [46–48] can be easily defined as debonding of peridynamic bonds, which makes it quite straightforward in crack modeling. In the present work, peridynamics is regarded as a “fine scale” computational technique as it directly provides information on the crack initiation and propagation.

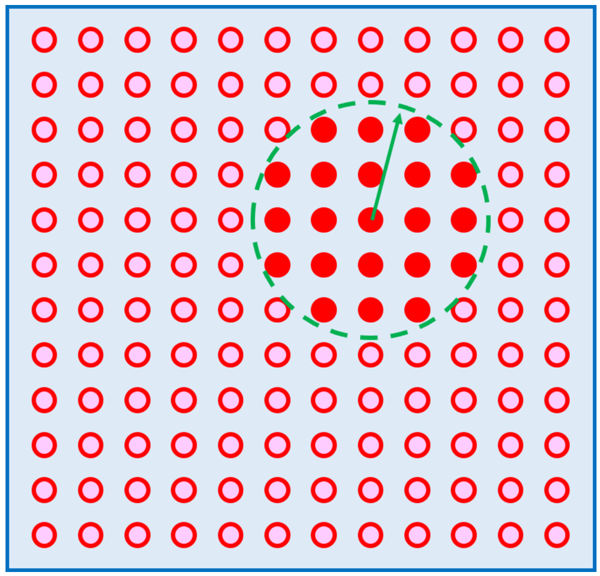

Figure 1. Image of horizon and family in peridynamics.

There exists three types of peridynamics formulation. The first one is called bond-based peridynamics and is proposed in [46]. The bond-based peridynamics theory has been built as a reformulation of elasticity theory. The pairwise bond force vectors between two material points have the same magnitude but opposite directions. Equivalently they can be regarded as two material points connected by a spring. In the bond-based peridynamics theory, the Poisson’s ratio is limited to 0.25. This original peridynamic theory has been generalized and other two types of peridynamics have been proposed in [48]. One is called ordinary state-based peridynamics and the other is non-ordinary state-based peridynamics. In deriving these state-based peridynamics theories, the concepts of some state vectors and correspondence between peridynamic constitutive model and classical continuum theory are introduced. In the ordinary state-based peridynamics, the force state vectors between two material point are parallel, however, not necessarily of the same magnitude. On the other hand, the pair of force state vectors are not necessarily parallel or same magnitude in non-ordinary state-based peridynamics. The image of three types of peridynamic theory is illustrated in Figure 2. In this work, non-ordinary state-based peridynamic theory is used for fracture prediction since continuum constitutive model can be incorporated in the theory. An example of crack propagation simulation of non-ordinary state-based peridynamics is shown in Figure 3.

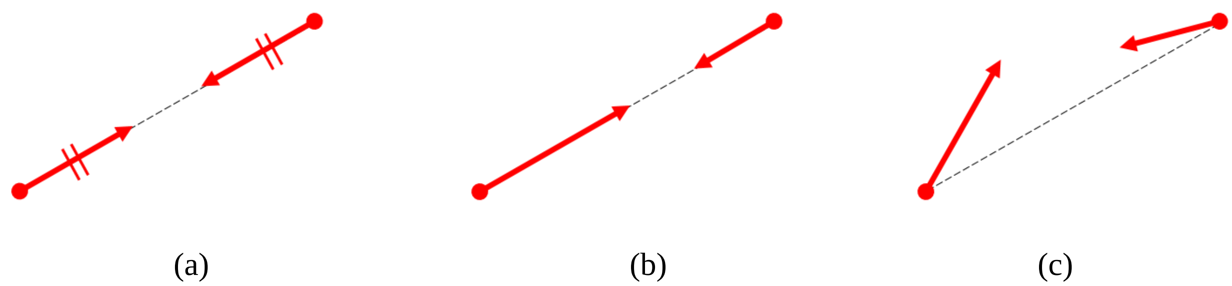

Figure 2. Illustration of force or force state vectors of each types peridynamics. (a) bond-based, (b) ordinary state-based and (c) non-ordinary state-based.

1.2 Objective

This work sets two main technical objectives. The first is to establish a nonlinear TDG-based space-time approach to fatigue failure prediction of rubbery materials. Motivation for the space-time approach is to overcome the limitations associated with the semi-discrete scheme in the finite element method. We note that most of the prior works summarized earlier on TDG

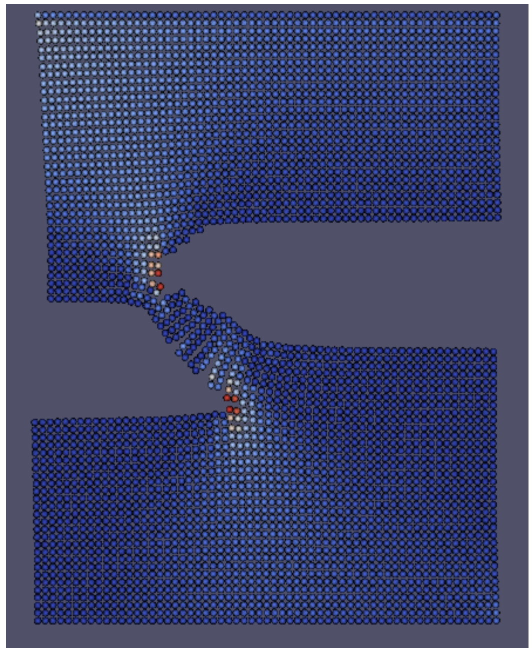

Figure 3. An example of fracture prediction of non-ordinary state-based peridynamics with Mooney-Rivlin hyperelastic constitutive law.

have focused on the linear formulations, and nonlinear TDG-based space-time FEM has not been systematically established and applied for practical application. In this work, the Mooney-Rivlin hyperelastic constitutive model and CDM models are coupled with TDG formulation. This integration leads to a nonlinear space-time FEM implementation that incorporates both geometric and material nonlinearities.

The second objective is to develop a coupled simulation approach in which peridynamics is integrated with space-time FEM. Several works of coupling peridynamic theory and FEM have been developed in recent years [49, 50]. In the current work, peridynamic model was applied to a local region where the failure initiates and propagates, and coupled to space-time FEM prescribed over the entire domain. This coupling approach is more robust in fracture prediction than FEM alone due to the addition of NOPD. Furthermore, it is also more efficient than a full-scale peridynamic simulation. The proposed work can be regarded as an extension to the earlier work in Chirputkar and Qian [36], in which the molecular dynamics in coupled with space-time FEM.

1.3 Outline of the Dissertation

The rest of the dissertation is organized as follows: In Chapter 2, we first review the space-time FEM framework based on time discontinuous Galerkin formulation. We then outline the implementation of space-time FEM with the use of total Lagrangian formulation. This implementation accounts for both geometric and material nonlinearities. The enriched space-time FEM is also described. In Chapter 3, we review several constitutive laws for rubbery materials. These include hyperelasticity, finite strain viscoelasticity and continuum damage mechanics model. Non-ordinary state-based peridynamics theory and implementation are reviewed in Chapter 4. In Chapter 5, we present detailed steps of the multiscale fracture simulation by coupling space-time FEM formulation with peridynamics. The applications of the approaches outlined in Chapter 2, 3, 4 and 5 are demonstrated through a set of numerical examples in Chapter 6. These examples are divided into two categories: One based on the nonlinear space-time FEM with constitutive models of rubber, and the other on multiscale coupled simulation of space-time FEM and non-ordinary state-based peridynamics. Conclusion and future works are presented in Chapter 7.

CHAPTER 2

SPACE-TIME FEM FORMULATION

2.1 Space-time FEM formulation for linear elastic material

In this section, the space-time FEM formulation for linear elasticity based on the updated Lagrangian formulation [51] and TDG formulation [30] is reviewed. The displacement is denoted by $\mathbf{u}(\mathbf{X},t)$, where $\mathbf{X}$ is the spatial coordinate and t is time. The strong form of initial/boundary value problem is defined over spatial domain Ω and temporal domain $I =]0,T[$ and given as follows.

$$\rho\ddot{\mathbf{u}} = \nabla\cdot\boldsymbol{\sigma} + \rho\mathbf{b} \quad \text{on} \quad Q \equiv \Omega\times I\,, \tag{1}$$

$$\mathbf{u} = \bar{\mathbf{u}} \quad \text{on}\ \gamma_u \equiv \Gamma_u \times I\,, \tag{2}$$

$$\mathbf{n}\cdot\boldsymbol{\sigma} = \mathbf{t} \quad \text{on}\ \gamma_t \equiv \Gamma_t \times I\,, \tag{3}$$

$$\mathbf{u}(\mathbf{X},0) = \mathbf{u}_0(\mathbf{X}) \quad \text{on}\ \mathbf{X}\in\Omega\,, \tag{4}$$

$$\mathbf{v}(\mathbf{X},0) = \mathbf{v}_0(\mathbf{X}) \quad \text{on}\ \mathbf{X}\in\Omega\,. \tag{5}$$

Here $\boldsymbol{\sigma}$, $\mathbf{b}$ and ρ represent the spatial Cauchy stress tensor, body force and mass density, respectively. Superimposed dot indicates the time derivative, $\bar{\mathbf{u}}$ and $\mathbf{t}$ are the prescribed displacement and traction over the essential boundary Γ_u and nature boundary Γ_t, respectively. Further, we have $\Gamma = \Gamma_u \cup \Gamma_t$ and $\Gamma_u \cap \Gamma_t = \varnothing$. Finally, $\mathbf{u}_0$ and $\mathbf{v}_0$ are the initial displacement and velocity.

In TDG formulation, the temporal domain $I =]0,T[$ is divided into multiple sub-domains

$I_n = \left]t_{n-1}, t_n\right[$ and each sub-domain and spatial domain are combined as a space-time slab $Q_n = \Omega \times I_n$. In addition, essential and traction boundary conditions are defined on $(\gamma_u)_n = \Gamma_u \times I_n$ and $(\gamma_t)_n = \Gamma_t \times I_n$ respectively. Furthermore, a space-time slab Q_n is discretized into $(n_{el})_n$ space-time slabs $Q_n^e \subset Q_n$ and its boundary is γ_n^e. Figure 4 shows an illustration of space-time discretization.

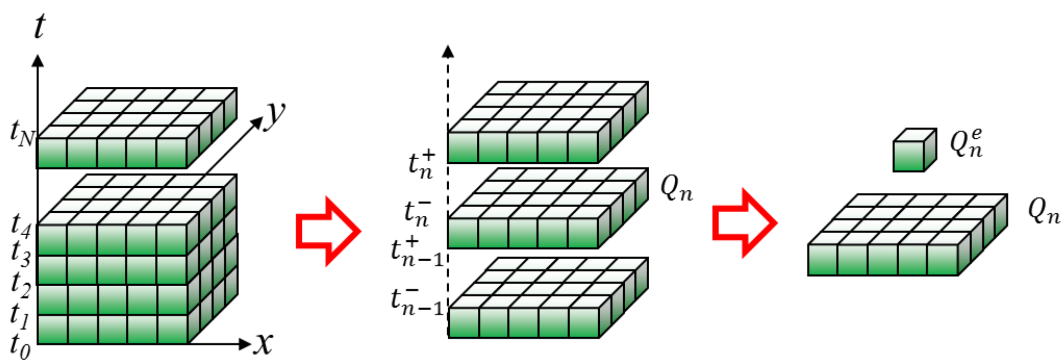

Figure 4. Image of space-time discretization for 2D spatial domain

We further introduce the jump operators to treat the temporal jumps between space-time slabs.

$$[\![\mathbf{u}(t_n)]\!] = \mathbf{u}(t_n^+) - \mathbf{u}(t_n^-) \tag{6}$$

$$\mathbf{u}(t_n^\pm) = \lim_{\varepsilon \to 0^\pm} \mathbf{u}(t_n \pm \varepsilon) \tag{7}$$

In deriving the weak form in TDG formulation, the trial function $\mathbf{u}^h(\mathbf{X}, t)$ and test function $\delta\mathbf{u}^h(\mathbf{X}, t)$ are introduced. The subscript "h" denotes the approximation and both the trial and test function are C^0 continuous.

$$\mathbf{u}^h(\mathbf{X},t) \in \boldsymbol{\mathcal{U}}, \quad \boldsymbol{\mathcal{U}} = \left\{ \mathbf{u}^h(\mathbf{X},t) \middle| \mathbf{u}^h \in C^0\left(\bigcup_{n=1}^{N} Q_n\right), \quad \mathbf{u}^h = \bar{\mathbf{u}} \text{ on } \mathit{\Gamma}_u \right\}, \tag{8}$$

$$\delta\mathbf{u}^h(\mathbf{X},t) \in \boldsymbol{\mathcal{U}}_0, \quad \boldsymbol{\mathcal{U}}_0 = \left\{ \delta\,\mathbf{u}^h(\mathbf{X},t) \middle| \delta\mathbf{u}^h \in C^0\left(\bigcup_{n=1}^{N} Q_n\right), \quad \delta\mathbf{u}^h = \mathbf{0} \text{ on } \mathit{\Gamma}_u \right\}. \tag{9}$$

The TDG weak form is constructed in each space-time slab by using bilinear form expression

$$\mathbf{B}\left(\delta\mathbf{u}^h, \mathbf{u}^h\right)_n = \mathbf{L}\left(\delta\mathbf{u}^h\right)_n \tag{10}$$

with

$$\begin{aligned}\mathbf{B}\left(\delta\mathbf{u}^h, \mathbf{u}^h\right)_n = &\int_{Q_n} \delta\dot{\mathbf{u}}^h \cdot \rho\ddot{\mathbf{u}}^h dQ + \int_{Q_n} \delta\left(\nabla\dot{\mathbf{u}}^h\right) \cdot \boldsymbol{\sigma} dQ \\ &+ \int_{\Omega} \delta\dot{\mathbf{u}}^h\left(t_{n-1}^+\right) \cdot \rho\dot{\mathbf{u}}^h\left(t_{n-1}^+\right) d\Omega + \int_{\Omega} \delta\left(\nabla\mathbf{u}^h\left(t_{n-1}^+\right)\right) \cdot \boldsymbol{\sigma}\left(t_{n-1}^+\right) d\Omega\end{aligned}, \tag{11}$$

$$\begin{aligned}\mathbf{L}\left(\delta\mathbf{u}^h\right)_n = &\int_{\gamma_n} \delta\dot{\mathbf{u}}^h \cdot \mathbf{t} d\gamma + \int_{Q_n} \delta\dot{\mathbf{u}}^h \cdot \rho\mathbf{b} dQ \\ &+ \int_{\Omega} \delta\dot{\mathbf{u}}^h\left(t_{n-1}^+\right) \cdot \rho\dot{\mathbf{u}}^h\left(t_{n-1}^-\right) d\Omega + \int_{\Omega} \delta\left(\nabla\mathbf{u}^h\left(t_{n-1}^+\right)\right) \cdot \boldsymbol{\sigma}\left(t_{n-1}^-\right) d\Omega\end{aligned}. \tag{12}$$

Here the subscript " n " denotes the n-th space-time slab. We can see the detail of this expression in [30]. Equations (10) to (12) leads to

$$\begin{aligned}0 = &\int_{Q_n} \delta\dot{\mathbf{u}}^h \cdot \rho\ddot{\mathbf{u}}^h dQ + \int_{Q_n} \delta\left(\nabla\dot{\mathbf{u}}^h\right) \cdot \boldsymbol{\sigma} dQ \\ &- \int_{\gamma_n} \delta\dot{\mathbf{u}}^h \cdot \mathbf{t} d\gamma - \int_{Q_n} \delta\dot{\mathbf{u}}^h \cdot \rho\mathbf{b} dQ \\ &+ \int_{\Omega} \delta\dot{\mathbf{u}}^h\left(t_{n-1}^+\right) \cdot [\![\rho\dot{\mathbf{u}}^h\left(t_{n-1}\right)]\!] d\Omega \\ &+ \int_{\Omega} \delta\left(\nabla\mathbf{u}^h\left(t_{n-1}^+\right)\right) \cdot [\![\boldsymbol{\sigma}\left(t_{n-1}\right)]\!] d\Omega\end{aligned} \tag{13}$$

To interpolate nodal displacement in spatial and temporal domain, a space-time shape function $\mathbf{N}(\mathbf{X},t)$ is introduced.

$$\mathbf{u}^h\left(\mathbf{X},t\right)=\sum_{I=1}^{n_s}N_I\left(\mathbf{X},t\right)\mathbf{d}_I\ , \tag{14}$$

$$\dot{\mathbf{u}}^h\left(\mathbf{X},t\right)=\sum_{I=1}^{n_s}\dot{N}_I\left(\mathbf{X},t\right)\mathbf{d}_I\ , \tag{15}$$

$$\ddot{\mathbf{u}}^h\left(\mathbf{X},t\right)=\sum_{I=1}^{n_s}\ddot{N}_I\left(\mathbf{X},t\right)\mathbf{d}_I\ , \tag{16}$$

where $\mathbf{d}$ is the element nodal displacement vector. Displacements at temporal jump follows the rule; (i) for $t=t_{n-1}^{-}$, displacements $\mathbf{d}_{n-1}$ from previous space-time slab are used. (ii) for $t=t_{n-1}^{+}$, displacement $\mathbf{d}_n$ from current space-time slab are assumed and obtained by solving equation (13). By assuming linear elastic constitutive model and substituting equations (14) to (16) into equation (13), we have

$$\begin{aligned}0=&\delta\mathbf{d}^T\left(\int_{Q_n}\dot{\mathbf{N}}^T\cdot\rho\ddot{\mathbf{N}}dQ\right)\mathbf{d}_n+\delta\mathbf{d}^T\left(\int_{Q_n}\dot{\mathbf{N}}_{,\mathbf{x}}^T\mathbf{C}\mathbf{N}_{,\mathbf{x}}dQ\right)\mathbf{d}_n\\&-\delta\mathbf{d}^T\int_{\gamma_n}\dot{\mathbf{N}}^T\cdot\mathbf{t}d\gamma-\delta\mathbf{d}^T\int_{Q_n}\dot{\mathbf{N}}^T\cdot\rho\mathbf{b}dQ\\&+\delta\mathbf{d}^T\left(\int_{\Omega}\dot{\mathbf{N}}^T\left(t_{n-1}^{+}\right)\cdot\rho\dot{\mathbf{N}}\left(t_{n-1}^{+}\right)d\Omega\right)\mathbf{d}_n-\delta\mathbf{d}^T\left(\int_{\Omega}\dot{\mathbf{N}}^T\left(t_{n-1}^{+}\right)\cdot\rho\dot{\mathbf{N}}\left(t_{n-1}^{-}\right)d\Omega\right)\mathbf{d}_{n-1}\\&+\delta\mathbf{d}^T\left(\int_{\Omega}\mathbf{N}_{,\mathbf{x}}^T\left(t_{n-1}^{+}\right)\mathbf{C}\mathbf{N}_{,\mathbf{x}}\left(t_{n-1}^{+}\right)d\Omega\right)\mathbf{d}_n-\delta\mathbf{d}^T\left(\int_{\Omega}\mathbf{N}_{,\mathbf{x}}^T\left(t_{n-1}^{+}\right)\mathbf{C}\mathbf{N}_{,\mathbf{x}}\left(t_{n-1}^{-}\right)d\Omega\right)\mathbf{d}_{n-1}\end{aligned}\ , \tag{17}$$

where $\mathbf{C}$ is the constitutive matrix. We can further simplify equation (17) into

$$\begin{aligned}&\left[\int_{Q_n}\dot{\mathbf{N}}^T\cdot\rho\ddot{\mathbf{N}}dQ+\int_{Q_n}\dot{\mathbf{N}}_{,\mathbf{x}}^T\mathbf{C}\mathbf{N}_{,\mathbf{x}}dQ+\begin{pmatrix}\int_{\Omega}\dot{\mathbf{N}}^T\left(t_{n-1}^{+}\right)\cdot\rho\dot{\mathbf{N}}\left(t_{n-1}^{+}\right)d\Omega\\+\int_{\Omega}\mathbf{N}_{,\mathbf{x}}^T\left(t_{n-1}^{+}\right)\mathbf{C}\mathbf{N}_{,\mathbf{x}}\left(t_{n-1}^{+}\right)d\Omega\end{pmatrix}\right]\mathbf{d}_n\\&=\left\{\int_{\gamma_n}\dot{\mathbf{N}}^T\cdot\mathbf{t}d\gamma+\int_{Q_n}\dot{\mathbf{N}}^T\cdot\rho\mathbf{b}dQ+\begin{pmatrix}\int_{\Omega}\dot{\mathbf{N}}^T\left(t_{n-1}^{+}\right)\cdot\rho\dot{\mathbf{N}}\left(t_{n-1}^{-}\right)d\Omega\\+\int_{\Omega}\mathbf{N}_{,\mathbf{x}}^T\left(t_{n-1}^{+}\right)\mathbf{C}\mathbf{N}_{,\mathbf{x}}\left(t_{n-1}^{-}\right)d\Omega\end{pmatrix}\mathbf{d}_{n-1}\right\}\end{aligned}\ . \tag{18}$$

Finally, we can treat equation (18) as a form of linear system

$$\mathscr{K}\mathbf{d}_n=\mathscr{F} \tag{19}$$

where $\mathscr{K}$ is global space-time stiffness matrix and $\mathscr{F}$ is global space-time force vector.

2.2 Implementation of space-time FEM for linear elastic material

For numerical discretization, a multiplicative form of the space-time FEM shape function $\mathbf{N}(\mathbf{X},t)$ is introduced

$$\begin{aligned}\mathbf{N}(\mathbf{X},t) &= \mathbf{N}_t(t)\otimes\mathbf{N}_s(\mathbf{X}) \\ &= \left[N_{t_1}\mathbf{N}_s \cdots N_{t_i}\mathbf{N}_s \cdots N_{t_n}\mathbf{N}_s \right],\end{aligned} \tag{20}$$

where $\mathbf{N}_s$ and $\mathbf{N}_t$ are the spatial and temporal shape functions respectively. Further, the symbol "$\otimes$" denotes the Kronecker product. In this work, the standard 4-node quadrilateral (Q4) element shape function has been adopted for $\mathbf{N}_s$.

$$\mathbf{N}_s = \frac{1}{4}\left[(1-\xi)(1-\eta) \quad (1+\xi)(1-\eta) \quad (1+\xi)(1+\eta) \quad (1-\xi)(1+\eta) \right], \tag{21}$$

Furthermore, a simple 3-node quadratic shape function is used for $\mathbf{N}_t$ and it can be given as a Lagrange form of the interpolation polynomial.

$$\mathbf{N}_t = \left[\frac{(t-t_{n-1/2})(t-t_n)}{(t_{n-1}-t_{n-1/2})(t_{n-1}-t_n)} \quad \frac{(t-t_n)(t-t_{n-1})}{(t_{n-1/2}-t_n)(t_{n-1/2}-t_{n-1})} \quad \frac{(t-t_{n-1})(t-t_{n-1/2})}{(t_n-t_{n-1})(t_n-t_{n-1/2})} \right], \tag{22}$$

where ξ and η are variables for the reference coordinate in the spatial domain. t_{n-1}, $t_{n-1/2}$ and t_n denote equally spaced three temporal nodes, so that

$$t_{n-1/2} = t_{n-1} + \frac{\Delta t}{2}, \tag{23}$$

$$t_n = t_{n-1} + \Delta t\,. \tag{24}$$

Then, the first and second derivatives of temporal shape function $\mathbf{N}_t$ are

$$\dot{\mathbf{N}}_t = \frac{1}{\Delta t^2}\left[\left(4t-4t_{n-1}-3\Delta t\right) \quad \left(-8t+8t_{n-1}+4\Delta t\right) \quad \left(4t-4t_{n-1}-\Delta t\right)\right] \tag{25}$$

$$\ddot{\mathbf{N}}_t = \frac{4}{\Delta t^2}\left[1 \quad -2 \quad 1\right] \tag{26}$$

Using spatial and temporal shape functions, four terms in LHS of equation (18) are rewritten as

$$\begin{aligned}\int_{Q_n} \dot{\mathbf{N}}^T \cdot \rho \ddot{\mathbf{N}} dQ &= \left(\int_{I_n} \dot{\mathbf{N}}_t^T \ddot{\mathbf{N}}_t dt\right) \otimes \left(\int_{\Omega} \mathbf{N}_s^T \rho \mathbf{N}_s d\Omega\right) \\ &= \frac{1}{\Delta t^2}\begin{bmatrix} -4 & 8 & 4 \\ 0 & 0 & 0 \\ 4 & -8 & 4 \end{bmatrix} \otimes \mathbf{M}\end{aligned}, \tag{27}$$

$$\begin{aligned}\int_{Q_n} \dot{\mathbf{N}}_{,\mathbf{x}}^T \mathbf{C} \mathbf{N}_{,\mathbf{x}} dQ &= \left(\int_{I_n} \dot{\mathbf{N}}_t^T \mathbf{N}_t dt\right) \otimes \left(\int_{\Omega} \mathbf{N}_{s,\mathbf{x}}^T \mathbf{C} \mathbf{N}_{s,\mathbf{x}} d\Omega\right) \\ &= \frac{1}{6}\begin{bmatrix} -3 & -4 & 1 \\ 4 & 0 & -4 \\ -1 & 4 & 3 \end{bmatrix} \otimes \mathbf{K}\end{aligned}, \tag{28}$$

$$\begin{aligned}\int_{\Omega} \dot{\mathbf{N}}^T \left(t_{n-1}^+\right) \cdot \rho \dot{\mathbf{N}}\left(t_{n-1}^+\right) d\Omega &= \left(\dot{\mathbf{N}}_t^T \left(t_{n-1}^+\right) \dot{\mathbf{N}}_t \left(t_{n-1}^+\right)\right) \otimes \left(\int_{\Omega} \mathbf{N}_s^T \rho \mathbf{N}_s d\Omega\right) \\ &= \frac{1}{\Delta t^2}\begin{bmatrix} 9 & -12 & 3 \\ -12 & 16 & -4 \\ 3 & -4 & 1 \end{bmatrix} \otimes \mathbf{M}\end{aligned}, \tag{29}$$

$$\begin{aligned}\int_{\Omega} \mathbf{N}_{,\mathbf{x}}^T \left(t_{n-1}^+\right) \mathbf{C} \mathbf{N}_{,\mathbf{x}} \left(t_{n-1}^+\right) d\Omega &= \left(\mathbf{N}_t^T \left(t_{n-1}^+\right) \mathbf{N}_t \left(t_{n-1}^+\right)\right) \otimes \left(\int_{\Omega} \mathbf{N}_{s,\mathbf{x}}^T \mathbf{C} \mathbf{N}_{s,\mathbf{x}} d\Omega\right) \\ &= \begin{bmatrix} 1 & 0 & 0 \\ 0 & 0 & 0 \\ 0 & 0 & 0 \end{bmatrix} \otimes \mathbf{K}\end{aligned}. \tag{30}$$

$\mathbf{M} = \int_{\Omega} \mathbf{N}_s^T \rho \mathbf{N}_s d\Omega$ and $\mathbf{K} = \int_{\Omega} \mathbf{N}_{s,\mathbf{x}}^T \mathbf{C} \mathbf{N}_{s,\mathbf{x}} d\Omega$ are mass matrix and stiffness matrix in the spatial domain. By combining equations (27) to (30), final expression for global space-time stiffness matrix $\mathscr{K}$ is obtained as

$$\mathscr{K} = \begin{bmatrix} \frac{5\mathbf{M}}{\Delta t^2} + \frac{\mathbf{K}}{2} & -\frac{4\mathbf{M}}{\Delta t^2} - \frac{2\mathbf{K}}{3} & -\frac{\mathbf{M}}{\Delta t^2} + \frac{\mathbf{K}}{6} \\ -\frac{12\mathbf{M}}{\Delta t^2} + \frac{2\mathbf{K}}{3} & \frac{16\mathbf{M}}{\Delta t^2} & -\frac{4\mathbf{M}}{\Delta t^2} - \frac{2\mathbf{K}}{3} \\ \frac{7\mathbf{M}}{\Delta t^2} - \frac{\mathbf{K}}{6} & -\frac{12\mathbf{M}}{\Delta t^2} + \frac{2\mathbf{K}}{3} & \frac{5\mathbf{M}}{\Delta t^2} + \frac{\mathbf{K}}{2} \end{bmatrix} \tag{31}$$

Similarly, the expression for the part of $\mathscr{F}$ in RHS of equation (18) can be derived as

$$\begin{aligned} \int_{\Omega} \dot{\mathbf{N}}^T \left(t_{n-1}^{+}\right) \cdot \rho \dot{\mathbf{N}}\left(t_{n-1}^{-}\right) d\Omega &= \left(\dot{\mathbf{N}}_t^T \left(t_{n-1}^{+}\right) \dot{\mathbf{N}}_t \left(t_{n-1}^{-}\right)\right) \otimes \left(\int_{\Omega} \mathbf{N}_s^T \rho \mathbf{N}_s d\Omega\right) \\ &= \frac{1}{\Delta t^2} \begin{bmatrix} -3 & 12 & -9 \\ 4 & -16 & 12 \\ -1 & 4 & -3 \end{bmatrix} \otimes \mathbf{M} \end{aligned}, \tag{32}$$

$$\begin{aligned} \int_{\Omega} \mathbf{N}_{,\mathbf{x}}^T \left(t_{n-1}^{+}\right) \mathbf{C} \mathbf{N}_{,\mathbf{x}} \left(t_{n-1}^{-}\right) d\Omega &= \left(\mathbf{N}_t^T \left(t_{n-1}^{+}\right) \mathbf{N}_t \left(t_{n-1}^{-}\right)\right) \otimes \left(\int_{\Omega} \mathbf{N}_{s,\mathbf{x}}^T \mathbf{C} \mathbf{N}_{s,\mathbf{x}} d\Omega\right) \\ &= \begin{bmatrix} 0 & 0 & 1 \\ 0 & 0 & 0 \\ 0 & 0 & 0 \end{bmatrix} \otimes \mathbf{K} \end{aligned}. \tag{33}$$

Then, we can define the matrix $\mathscr{H}$ as

$$\begin{aligned} \mathscr{H} &= \int_{\Omega} \dot{\mathbf{N}}^T \left(t_{n-1}^{+}\right) \cdot \rho \dot{\mathbf{N}}\left(t_{n-1}^{-}\right) d\Omega + \int_{\Omega} \mathbf{N}_{,\mathbf{x}}^T \left(t_{n-1}^{+}\right) \mathbf{C} \mathbf{N}_{,\mathbf{x}} \left(t_{n-1}^{-}\right) d\Omega \\ &= \begin{bmatrix} -\frac{3\mathbf{M}}{\Delta t^2} & \frac{12\mathbf{M}}{\Delta t^2} & -\frac{9\mathbf{M}}{\Delta t^2} + \mathbf{K} \\ \frac{4\mathbf{M}}{\Delta t^2} & -\frac{16\mathbf{M}}{\Delta t^2} & \frac{12\mathbf{M}}{\Delta t^2} \\ -\frac{\mathbf{M}}{\Delta t^2} & \frac{4\mathbf{M}}{\Delta t^2} & -\frac{3\mathbf{M}}{\Delta t^2} \end{bmatrix} \end{aligned}. \tag{34}$$

Finally, the current space-time displacement vector $\mathbf{d}_n$ can be solved as follows.

$$\begin{aligned} \mathbf{d}_n &= \mathscr{K}^{-1} \mathscr{F} \\ &= \mathscr{K}^{-1} \left(\int_{\gamma_n} \dot{\mathbf{N}}^T \cdot \mathbf{t} d\gamma + \int_{Q_n} \dot{\mathbf{N}}^T \cdot \rho \mathbf{b} dQ + \mathscr{H} \mathbf{d}_{n-1} \right) \end{aligned}. \tag{35}$$

The integration parts come from traction and body force can be computed numerically. If the function forms of these terms are known, we can also integrate them analytically. The implementation steps are provided as follows.

1. Discretize the spatial and temporal domain.
2. Build the regular spatial mass matrix $\mathbf{M}$ and stiffness matrix $\mathbf{K}$ by Gauss quadrature integration.
3. To obtain the matrices $\mathscr{K}$ and $\mathscr{H}$, assemble $\mathbf{M}$ and $\mathbf{K}$ by following equations (31) and (34). Apply boundary condition for $\mathscr{K}$ and compute $\mathscr{K}^{-1}$ in advance of starting time step loop. ($\mathscr{K}$ and $\mathscr{H}$ are constant unless the spatial or temporal mesh change.)
4. Start the time step loop.

   (i) Perform space-time integration regarding traction boundary $\int_{\gamma_n} \dot{\mathbf{N}}^T \cdot \mathbf{t} d\gamma$ and body force $\int_{Q_n} \dot{\mathbf{N}}^T \cdot \rho \mathbf{b} dQ$ in RHS of equation (35).

   (ii) Compute $\mathscr{F}$ in equation (35) and apply boundary conditions.

   (iii) Solve the space-time displacement vector $\mathbf{d}_n = \mathscr{K}^{-1}\mathscr{F}$.

   (iv) Store the displacement vector $\mathbf{d}_n$ as $\mathbf{d}_{n-1}$ for the next step.
5. End the time step loop.

2.3 Nonlinear space-time FEM formulation

The space-time FEM formulation and implementation shown in section 2.1 and 2.2 are applicable only for linear elastic constitutive model. In this and following section, the formulation and implementation for nonlinear space-time FEM are developed. Based on this nonlinear space-time FEM framework, dynamic problems including material and geometrical nonlinearly can be solved.

Nonlinear space-time FEM formulation is derived by following total Lagrangian formulation [51]. Then, the nominal stress tensor $\mathbf{P}$ is used instead of the Cauchy stress tensor $\boldsymbol{\sigma}$ to handle large deformation problems. The strong form of initial/boundary value problem is defined over spatial domain Ω_0 and temporal domain $I = \left]0,T\right[$ and is given as follows.

$$\nabla_{\mathbf{X}} \cdot \mathbf{P} + \rho_0 \mathbf{b} = \rho_0 \ddot{\mathbf{u}} \quad \text{on} \;\; Q \equiv \Omega_0 \times I \,, \tag{36}$$

$$\mathbf{u} = \bar{\mathbf{u}} \quad \text{on} \;\gamma_u \equiv \Gamma_u^0 \times I \,, \tag{37}$$

$$\mathbf{n}_0 \cdot \mathbf{P} = \mathbf{t}_0 \quad \text{on} \;\gamma_t \equiv \Gamma_t^0 \times I \,, \tag{38}$$

$$\mathbf{u}(\mathbf{X},0) = \mathbf{u}_0(\mathbf{X}) \quad \text{on} \;\mathbf{X} \in \Omega_0 \,, \tag{39}$$

$$\mathbf{v}(\mathbf{X},0) = \mathbf{v}_0(\mathbf{X}) \quad \text{on} \;\mathbf{X} \in \Omega_0 \,, \tag{40}$$

where the subscript zero denotes the material configuration so that, for example, $\mathbf{n}_0$ is normal vector of undeformed traction boundary Γ_t^0. Also, the essential boundary Γ_u^0 and nature boundary Γ_t^0 have relationship $\Gamma^0 = \Gamma_u^0 \cup \Gamma_t^0$ and $\Gamma_u^0 \cap \Gamma_t^0 = \varnothing$. Figure 4 in section 2.1 shows an illustration of space-time discretization.

Similarly to the linear elastic material case, we introduce jump operators in equations (6) and (7). The trial function and test function are given as well.

$$\mathbf{u}^h(\mathbf{X},t) \in \boldsymbol{\mathcal{U}}, \quad \boldsymbol{\mathcal{U}} = \left\{ \mathbf{u}^h(\mathbf{X},t) \middle| \mathbf{u}^h \in C^0\left(\bigcup_{n=1}^{N} Q_n\right), \quad \mathbf{u}^h = \bar{\mathbf{u}} \text{ on } \Gamma_u^0 \right\}, \tag{41}$$

$$\delta\mathbf{u}^h(\mathbf{X},t)\in\mathcal{U}_0, \quad \mathcal{U}_0=\left\{\delta\mathbf{u}^h(\mathbf{X},t)\middle|\delta\mathbf{u}^h\in C^0\left(\bigcup_{n=1}^{N}Q_n\right), \quad \delta\mathbf{u}^h=\mathbf{0}\text{ on }\Gamma_u^0\right\}. \tag{42}$$

The nonlinear TDG weak form is constructed in each space-time slab, e.g.

$$\mathbf{B}\left(\delta\mathbf{u}^h,\mathbf{u}^h\right)_n=\mathbf{L}\left(\delta\mathbf{u}^h\right)_n \tag{43}$$

with

$$\begin{aligned}\mathbf{B}\left(\delta\mathbf{u}^h,\mathbf{u}^h\right)_n&=\int_{Q_n}\delta\dot{\mathbf{u}}^h\cdot\rho_0\ddot{\mathbf{u}}^h dQ+\int_{Q_n}\delta\left(\nabla_{\mathbf{X}}\dot{\mathbf{u}}^h\right)\cdot\mathbf{P}dQ\\&\quad+\int_{\Omega_0}\delta\dot{\mathbf{u}}^h\left(t_{n-1}^+\right)\cdot\rho_0\dot{\mathbf{u}}^h\left(t_{n-1}^+\right)d\Omega_0+\int_{\Omega_0}\delta\left(\nabla_{\mathbf{X}}\mathbf{u}^h\left(t_{n-1}^+\right)\right)\cdot\mathbf{P}\left(t_{n-1}^+\right)d\Omega_0\end{aligned} \tag{44}$$

$$\begin{aligned}\mathbf{L}\left(\delta\mathbf{u}^h\right)_n&=\int_{\gamma_n}\delta\dot{\mathbf{u}}^h\cdot\mathbf{t}_0 d\gamma+\int_{Q_n}\delta\dot{\mathbf{u}}^h\cdot\rho_0\mathbf{b}dQ\\&\quad+\int_{\Omega_0}\delta\dot{\mathbf{u}}^h\left(t_{n-1}^+\right)\cdot\rho_0\dot{\mathbf{u}}^h\left(t_{n-1}^-\right)d\Omega_0+\int_{\Omega_0}\delta\left(\nabla_{\mathbf{X}}\mathbf{u}^h\left(t_{n-1}^+\right)\right)\cdot\mathbf{P}\left(t_{n-1}^-\right)d\Omega_0\end{aligned} \tag{45}$$

Combining equations (43) to (45) leads to

$$\begin{aligned}0&=\int_{Q_n}\delta\dot{\mathbf{u}}^h\cdot\rho_0\ddot{\mathbf{u}}^h dQ+\int_{Q_n}\delta\left(\nabla_{\mathbf{X}}\dot{\mathbf{u}}^h\right)\cdot\mathbf{P}dQ\\&\quad-\int_{\gamma_n}\delta\dot{\mathbf{u}}^h\cdot\mathbf{t}_0 d\gamma-\int_{Q_n}\delta\dot{\mathbf{u}}^h\cdot\rho_0\mathbf{b}dQ\\&\quad+\int_{\Omega_0}\delta\dot{\mathbf{u}}^h\left(t_{n-1}^+\right)\cdot\left[\!\left[\rho_0\dot{\mathbf{u}}^h\left(t_{n-1}\right)\right]\!\right]d\Omega_0\\&\quad+\int_{\Omega_0}\delta\left(\nabla_{\mathbf{X}}\mathbf{u}^h\left(t_{n-1}^+\right)\right)\cdot\left[\!\left[\mathbf{P}\left(t_{n-1}\right)\right]\!\right]d\Omega_0\end{aligned}. \tag{46}$$

It can then be seen from equation (46) that the integrations over Q_n (first, second and fourth term) enforces the conservation of linear momentum, traction boundary condition is enforced through the integration over γ_n, and the last two integrals enforces the continuities for the velocity and displacement, respectively.

To interpolate nodal displacement in spatial and temporal domain, space-time shape function $\mathbf{N}(\mathbf{X},t)$ is introduced. Displacement, velocity and acceleration approximation is given in equations (14) to (16). Substitution of these interpolation formulations into equation (46) leads to

$$
\begin{aligned}
0 = {} & \delta \mathbf{d}^T \left(\int_{Q_n} \dot{\mathbf{N}}^T \cdot \rho \ddot{\mathbf{N}} dQ \right) \mathbf{d}_n + \delta \mathbf{d}^T \left(\int_{Q_n} \dot{\mathbf{N}}_{,\mathbf{x}}^T \mathbf{P} dQ \right) \\
& - \delta \mathbf{d}^T \int_{\gamma_n} \dot{\mathbf{N}}^T \cdot \mathbf{t} d\gamma - \delta \mathbf{d}^T \int_{Q_n} \dot{\mathbf{N}}^T \cdot \rho \mathbf{b} dQ \\
& + \delta \mathbf{d}^T \left(\int_{\Omega} \dot{\mathbf{N}}^T \left(t_{n-1}^+ \right) \cdot \rho \dot{\mathbf{N}} \left(t_{n-1}^+ \right) d\Omega \right) \mathbf{d}_n - \delta \mathbf{d}^T \left(\int_{\Omega} \dot{\mathbf{N}}^T \left(t_{n-1}^+ \right) \cdot \rho \dot{\mathbf{N}} \left(t_{n-1}^- \right) d\Omega \right) \mathbf{d}_{n-1} \\
& + \delta \mathbf{d}^T \left(\int_{\Omega} \mathbf{N}_{,\mathbf{x}}^T \left(t_{n-1}^+ \right) \mathbf{P} \left(t_{n-1}^+ \right) d\Omega \right) - \delta \mathbf{d}^T \left(\int_{\Omega} \mathbf{N}_{,\mathbf{x}}^T \left(t_{n-1}^+ \right) \mathbf{P} \left(t_{n-1}^- \right) d\Omega \right)
\end{aligned}
\quad . \tag{47}
$$

Unlike in the case of space-time FEM for linear elastic material, we cannot take displacement vector out from nominal stress tensor. In other words, we cannot solve equation (47) as a linear system directly. Therefore, we introduce residual vector $\mathbf{G}$ as following.

$$
\mathbf{G} = \mathbf{G}_{int} + \mathbf{G}_{kin} - \mathbf{G}_{ext} = \mathbf{0} \tag{48}
$$

in which $\mathbf{G}_{int}$, $\mathbf{G}_{kin}$ and $\mathbf{G}_{ext}$ represent the contributions from the internal, kinetic and external forcing terms respectively and are given as

$$
\mathbf{G}_{int} = \int_{Q_n} \dot{\mathbf{N}}_{,\mathbf{X}}^T \mathbf{P} dQ_n + \int_{\Omega_0} \mathbf{N}_{,\mathbf{X}}^T \left(t_{n-1}^+ \right) \mathbf{P} \left(t_{n-1}^+ \right) d\Omega_0 \, , \tag{49}
$$

$$
\mathbf{G}_{kin} = \left(\int_{Q_n} \dot{\mathbf{N}}^T \cdot \rho_0 \ddot{\mathbf{N}} dQ_n + \int_{\Omega_0} \dot{\mathbf{N}}^T \left(t_{n-1}^+ \right) \cdot \rho_0 \dot{\mathbf{N}} \left(t_{n-1}^+ \right) d\Omega_0 \right) \mathbf{d}_n \, , \tag{50}
$$

$$
\begin{aligned}
\mathbf{G}_{ext} = {} & \int_{\gamma_n} \dot{\mathbf{N}}^T \cdot \mathbf{t}_0 d\gamma_n + \int_{Q_n} \dot{\mathbf{N}}^T \cdot \rho_0 \mathbf{f} dQ_n \\
& + \int_{\Omega_0} \mathbf{N}_{,\mathbf{X}}^T \left(t_{n-1}^+ \right) \mathbf{P} \left(t_{n-1}^- \right) d\Omega_0 \\
& + \left(\int_{\Omega_0} \dot{\mathbf{N}}^T \left(t_{n-1}^+ \right) \cdot \rho_0 \dot{\mathbf{N}} \left(t_{n-1}^- \right) d\Omega_0 \right) \mathbf{d}_{n-1}
\end{aligned}
\quad . \tag{51}
$$

2.4 Implementation of nonlinear space-time FEM

Similar to the case of space-time FEM for linear elasticity, a multiplicative form of the space-time FEM shape function $\mathbf{N}(\mathbf{X},t)$ is introduced for numerical discretization.

$$\begin{aligned}\mathbf{N}(\mathbf{X},t) &= \mathbf{N}_t \otimes \mathbf{N}_s \\ &= \begin{bmatrix} N_{t_1}\mathbf{N}_s & \cdots & N_{t_i}\mathbf{N}_s & \cdots & N_{t_k}\mathbf{N}_s \end{bmatrix}\end{aligned}. \tag{52}$$

For the numerical examples shown in this dissertation, the standard 4-node quadrilateral (Q4) element spatial shape function and a simple 3-node quadratic temporal shape function is used for $\mathbf{N}_s$ and $\mathbf{N}_t$ as shown in equations (21) and (22).

The form of $\mathbf{N}(\mathbf{X},t)$ shown in equation (52) leads to independent evaluation of the integrals over the spatial and temporal domains as shown in equations (49) to (51). To handle incompressibility, the selective reduced integration scheme [51] has been implemented. We first decompose the nominal stress tensor into hydrostatic and deviatoric components:

$$\mathbf{P} = \mathbf{P}^{hyd} + \mathbf{P}^{dev}, \tag{53}$$

$$\mathbf{P}^{hyd} = J\mathbf{F}^{-1}\boldsymbol{\sigma}^{hyd}, \tag{54}$$

$$\mathbf{P}^{dev} = J\mathbf{F}^{-1}\boldsymbol{\sigma}^{dev}, \tag{55}$$

$$\boldsymbol{\sigma}^{hyd} = \frac{1}{3}\operatorname{tr}(\boldsymbol{\sigma})\cdot\mathbf{1}, \tag{56}$$

$$\boldsymbol{\sigma}^{dev} = \boldsymbol{\sigma} - \boldsymbol{\sigma}^{hyd}, \tag{57}$$

where $\boldsymbol{\sigma}^{hyd}$ and $\boldsymbol{\sigma}^{dev}$ are hydrostatic and deviatoric part of Cauchy stress tensor $\boldsymbol{\sigma}$, $\mathbf{F}$ is deformation gradient tensor, $J = \det(\mathbf{F})$ is the Jacobian determinant and $\mathbf{1}$ is the identity tensor. The deformation gradient $\mathbf{F}$ is computed based on displacement vector. Accordingly, one point integration is employed for the terms related to the hydrostatic component to avoid locking [51], while full quadrature is carried out for the deviatoric components. In the case of a single space-time element using Q4 for $\mathbf{N}_s$,

$$\begin{aligned}\mathbf{G}_{int} = \sum_{i=1}^{n_t}\left\{\left[\dot{\mathbf{N}}_t^T\left(t_i\right)w_t\left(t_i\right)\right]\otimes\left[\begin{array}{l}\sum_{Q=1}^{n_Q}\mathbf{B}_0^T\left(\boldsymbol{\xi}_Q\right)\mathbf{P}^{dev}\left(\boldsymbol{\xi}_Q,t_i\right)J_{\xi}\left(\boldsymbol{\xi}_Q\right)w_s \\ +\mathbf{B}_0^T\left(\mathbf{0}\right)\mathbf{P}^{hyd}\left(\mathbf{0},t_i\right)J_{\xi}\left(\mathbf{0}\right)w_s\left(\mathbf{0}\right)\end{array}\right]\right\} \\ +\left[\mathbf{N}_t^T\left(t_{n-1}^+\right)\right]\otimes\left[\begin{array}{l}\sum_{Q=1}^{n_Q}\mathbf{B}_0^T\left(\boldsymbol{\xi}_Q\right)\mathbf{P}^{dev}\left(\boldsymbol{\xi}_Q,t_{n-1}^+\right)J_{\xi}\left(\boldsymbol{\xi}_Q\right)w_s\left(\boldsymbol{\xi}_Q\right) \\ +\mathbf{B}_0^T\left(\mathbf{0}\right)\mathbf{P}^{hyd}\left(\mathbf{0},t_{n-1}^+\right)J_{\xi}\left(\mathbf{0}\right)w_s\left(\mathbf{0}\right)\end{array}\right]\end{aligned} \tag{58}$$

in which i and Q are introduced as the index for the temporal and spatial quadrature points, and n_t and n_Q denote the number of the temporal and spatial quadrature points, respectively. The associated quadrature weights are w_t and w_s. For the spatial Q4 element, the element coordinate $\boldsymbol{\xi}$ is introduced. The Jacobian for the spatial element and its determinant are given as $\mathbf{J}_{\xi} = \frac{\partial \mathbf{X}}{\partial \boldsymbol{\xi}}$ and $J_{\xi} = \det\left(\mathbf{J}_{\xi}\right)$. The strain-displacement matrix is then evaluated as $\mathbf{B}_0 = \frac{\partial \mathbf{N}_s}{\partial \mathbf{X}} = \frac{\partial \mathbf{N}_s}{\partial \boldsymbol{\xi}}\frac{\partial \boldsymbol{\xi}}{\partial \mathbf{X}} = \mathbf{N}_{s,\xi}\mathbf{X}_{,\xi}^{-1} = \mathbf{N}_{s,\xi}\mathbf{J}_{\xi}^{-1}$.

The kinetic contribution $\mathbf{G}_{kin}$ in equation (50) is given by following the procedure similar to the case of linear space-time FEM. By referring equations (27) and (29), we have

$$\begin{aligned}\mathbf{G}_{kin} &= \left[\left(\int_{I_n}\dot{\mathbf{N}}_t^T\ddot{\mathbf{N}}_t dt + \dot{\mathbf{N}}_t^T\left(t_{n-1}^+\right)\dot{\mathbf{N}}_t\left(t_{n-1}^+\right)\right)\otimes\int_{\Omega_0}\mathbf{N}_s^T\cdot\rho_0\mathbf{N}_s d\Omega_0\right]\mathbf{d}_n \\ &= \left(\frac{1}{\Delta t^2}\begin{bmatrix} 5 & -4 & -1 \\ -12 & 16 & -4 \\ 7 & -12 & 5\end{bmatrix}\otimes\mathbf{M}\right)\mathbf{d}_n\end{aligned}. \tag{59}$$

Again, $\mathbf{M} = \int_{\Omega_0}\mathbf{N}_s^T\cdot\rho_0\mathbf{N}_s d\Omega_0$ is the spatial mass matrix.

The term related to the external force part $\mathbf{G}_{ext}$ in equation (51) of the residual vector $\mathbf{G}$ is given as

$$\begin{aligned}\mathbf{G}_{ext} = &\int_{I_n} \dot{\mathbf{N}}_t^T \otimes \left(\int_{\Gamma_t^0} \mathbf{t}_0 \left(\mathbf{X}, t \right) d\Gamma_0 \right) dt \\ &+ \int_{I_n} \dot{\mathbf{N}}_t^T \otimes \left(\int_{\Omega_0} \rho_0 \mathbf{b} \left(\mathbf{X}, t \right) d\Omega_0 \right) dt \\ &+ \mathbf{N}_t^T \left(t_{n-1}^+ \right) \otimes \int_{\Omega_0} \mathbf{B}_0^T \mathbf{P} \left(t_{n-1}^- \right) d\Omega_0 \\ &+ \left[\left\{ \dot{\mathbf{N}}_t^T \left(t_{n-1}^+ \right) \dot{\mathbf{N}}_t \left(t_{n-1}^- \right) \right\} \otimes \mathbf{M} \right] \mathbf{d}_{n-1}\end{aligned} \tag{60}$$

in which the first and second terms come from the traction boundary condition and body force. The third term represents the jump term related to the internal force. It can be evaluated by using a similar procedure as the corresponding jump term in $\mathbf{G}_{int}$, i.e.,

$$\begin{aligned}&\mathbf{N}_t^T \left(t_{n-1}^+ \right) \otimes \int_{\Omega_0} \mathbf{B}_0^T \mathbf{P} \left(t_{n-1}^- \right) d\Omega_0 \\ &= \left\{ \mathbf{N}_t^T \left(t_{n-1}^+ \right) \right\} \otimes \left\{ \begin{aligned} &\sum_{Q=1}^{n_Q} \mathbf{B}_0^T \left(\boldsymbol{\xi}_Q \right) \mathbf{P}^{dev} \left(\boldsymbol{\xi}_Q, t_{n-1}^- \right) J_\xi \left(\boldsymbol{\xi}_Q \right) w_s \left(\boldsymbol{\xi}_Q \right) \\ &+ \mathbf{B}_0^T \left(\mathbf{0} \right) \mathbf{P}^{hyd} \left(\mathbf{0}, t_{n-1}^- \right) J_\xi \left(\mathbf{0} \right) w_s \left(\mathbf{0} \right) \end{aligned} \right\}.\end{aligned} \tag{61}$$

The multiplication of temporal shape functions in the fourth term of equation (60) can be shown to be

$$\dot{\mathbf{N}}_t^T \left(t_{n-1}^+ \right) \dot{\mathbf{N}}_t \left(t_{n-1}^- \right) = \frac{1}{\Delta t^2} \begin{bmatrix} -3 & 12 & -9 \\ 4 & -16 & 12 \\ -1 & 4 & -3 \end{bmatrix}. \tag{62}$$

With the evaluations of the $\mathbf{G}_{int}$, $\mathbf{G}_{kin}, \mathbf{G}_{ext}$ as shown above, the final space-time equation (48) is generally a nonlinear equation and is solved by employing Newton's method [52], i.e.,

$$\left[\frac{\partial \mathbf{G}}{\partial \mathbf{d}_n} \right]_m \cdot \Delta \mathbf{d}_m \approx \mathbf{G}_m, \quad m = 0, 1, 2, \cdots, \tag{63}$$

$$\mathbf{d}_n^{m+1} \approx \mathbf{d}_n^m - \left[\frac{\partial \mathbf{G}}{\partial \mathbf{d}_n}\right]_m^{-1} \cdot \mathbf{G}_m, \tag{64}$$

where m is the iterative index. The Jacobian matrix of Newton's method $\left[\frac{\partial \mathbf{G}}{\partial \mathbf{d}_n}\right]$ can be estimated by numerical differentiation methods, e.g., the finite difference scheme. In this work, the forward difference method is used [52],

$$\frac{\partial G_i}{\partial d_j} \approx \frac{G_i\left(d_1, d_2, \cdots, d_j + \Delta d_j, \cdots\right) - G_i\left(d_1, d_2, \cdots, d_j, \cdots\right)}{\Delta d_j}. \tag{65}$$

The linear system of equation (64) is solved by using a sparse direct solver intel MKL PARDISO [53]. The iterative step as indicated from equation (64) continues until the following criterion is satisfied:

$$\min\left(\left\|\mathbf{G}_m\right\|_2, \left\|\Delta \mathbf{d}_m\right\|_2\right) / N_{DOF} < \varepsilon \tag{66}$$

where $\|\bullet\|_2 = \sqrt{\bullet \cdot \bullet}$ is the L2 norm and N_{DOF} is the total number of degree of freedom with regard to space-time nodes. For the present application, the tolerance value $\varepsilon = 10^{-3}$ is used. Finally, the implementation flow is shown as follows.

1. Discretize the spatial and temporal domain.

2. Start the time step loop.

    (i) Give an initial guess for the displacement vector $\mathbf{d}_n^0$.

    (ii) Start Newton's method loop to solve $\mathbf{d}_n$ that satisfies $\mathbf{G} = \mathbf{0}$.

        [a] Compute $\mathbf{G}_{kin}$ and $\mathbf{G}_{int}$ in equations (58) and (59) based on the current

displacement vector $\mathbf{d}_n^m$. The nominal stress tensor $\mathbf{P}$ in $\mathbf{G}_{int}$ is evaluated by nonlinear material constitutive law.

[b] Compute $\mathbf{G}_{ext}$ in equation (60) based on traction boundary, body force and the displacement at previous time step $\mathbf{d}_{n-1}$.

[c] Assemble residual vectors and obtain $\mathbf{G}_m$.

[d] Compute the Jacobian matrix of Newton's method $\left[\frac{\partial \mathbf{G}_m}{\partial \mathbf{d}_n}\right]$ based on equation (65).

[e] Compute $\mathbf{d}_n^{m+1}$ based on equation (64). If the criterion (66) is satisfied, $\mathbf{d}_n^m$ is the solution and exit the Newton's method loop. Otherwise, repeat [a] to [e].

(iii) Store the displacement vector $\mathbf{d}_n$ as $\mathbf{d}_{n-1}$ for the next time step.

3. End the time step loop.

2.5 Extended space-time FEM formulation and implementation

In the previous sections, the temporal domain of each space-time slab is discretized using the standard quadratic shape function. In this section, enrichment is introduced into the space-time shape function. The idea of enriching shape function in FEM with the function that represents the problem physics has been developed in extended finite element method (XFEM) [45] or generalized finite element method (GFEM) [54]. Both XFEM and GFEM are based on the partition of unity finite element method developed by Melenk and Babuška [34]. The extended space-time FEM (XTFEM) is developed by applying enrichment for temporal domain too. Chessa and Belytschko [35] applied XFEM concept for temporal domain to capture the discontinuity in time as well as space. Chirputkar, Qian [36, 37] and Yang [38] used XTFEM for coupled molecular dynamics and FEM simulation. Bhamare et al [39] proposed the computational framework to predict high cycle fatigue life of linear elastic material by combining XTFEM with damage model based of continuous damage mechanics (CDM) [8, 10]. In Bhamare's work, harmonic function is used as the enrichment of temporal shape function [39] to capture the deformation at cyclic loading. In this work, the XFEM formulation [45] was extended to deal with nonlinear problems.

The form of enriched space-time FEM approximation is

$$\mathbf{u}^h(\mathbf{X},t) = \sum_I N_I(\mathbf{X},t)\mathbf{d}_I + \sum_J \tilde{N}_J(\mathbf{X},t)\mathbf{a}_J\ , \tag{67}$$

where $\mathbf{d}_I$ and $\mathbf{a}_J$ are the space-time displacement vector and additional degree of freedom of the enriched part. The first term of RHS is regular space-time interpolation and $N_I(\mathbf{X},t)$ is a component of space-time shape function that is introduced in equation (14). The enriched shape function in the second term is,

$$\tilde{N}_J(\mathbf{X},t) = N_J(\mathbf{X},t)\Psi_J(\mathbf{X},t) \tag{68}$$

In the case of crack modeling, the shifted Heaviside function is used to express the strong discontinuity of the crack and only spatial domain is enriched so that,

$$\Psi_J(\mathbf{X},t) = H(\phi(\mathbf{X})) - H(\phi(\mathbf{X}_J)) \tag{69}$$

$$H(\alpha) = \begin{cases} 1, & \alpha \geq 0 \\ 0, & \alpha < 0 \end{cases} \tag{70}$$

$\phi(\mathbf{X})$ is the signed distance function regarding the crack. Figure 5 shows the relationship of the position and value of $\phi(\mathbf{X})$ in crack enrichment.

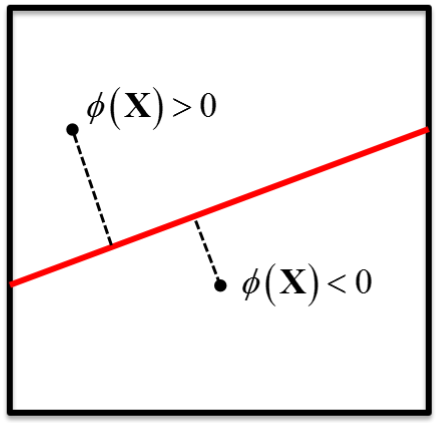

Figure 5. Image of crack enriched element and signed distance function.

Next, the case of the sinusoidal enrichment in temporal domain is shown. In the case of crack enrichment of spatial domain, we only enrich the element with crack. However, temporal enrichment is implemented over the whole space-time slab. If we chose quadratic temporal shape function for regular space-time FEM part and use the same temporal nodal position for both the regular and enriched parts, we have

$$\begin{aligned}\mathbf{u}^h(\mathbf{X},t) &= \begin{bmatrix} N_{t_1}\mathbf{N}_s & N_{t_2}\mathbf{N}_s & N_{t_3}\mathbf{N}_s & \tilde{N}_{t_1}\mathbf{N}_s & \tilde{N}_{t_2}\mathbf{N}_s & \tilde{N}_{t_3}\mathbf{N}_s \end{bmatrix}\begin{Bmatrix}\mathbf{d}\\ \mathbf{a}\end{Bmatrix} \\ &= \sum_I N_I(\mathbf{X},t)\mathbf{d}_I + \sum_I \tilde{N}_I(\mathbf{X},t)\mathbf{a}_I\end{aligned} \tag{71}$$

where N_{t_i} is the regular temporal shape function given in equation (22). In the case of sinusoidal enrichment, we define the enrichment function $\Psi_J(\mathbf{X},t)$ in equation (68) as

$$\Psi_J(\mathbf{X},t) = \sin(\omega t) - \sin(\omega t_J) \tag{72}$$

where ω is the angular frequency of sinusoidal function and t_J is the temporal enriched node. Therefore, $\tilde{N}_{t_i}$ is in equation (71) is given as

$$\tilde{N}_{t_1} = N_{t_1}\Psi_1 = \frac{\left(t - t_{n-1/2}\right)\left(t - t_n\right)}{\left(t_{n-1} - t_{n-1/2}\right)\left(t_{n-1} - t_n\right)}\left\{\sin\left(\omega t\right) - \sin\left(\omega t_{n-1}\right)\right\}, \tag{73}$$

$$\tilde{N}_{t_2} = N_{t_2}\Psi_2 = \frac{\left(t - t_n\right)\left(t - t_{n-1}\right)}{\left(t_{n-1/2} - t_n\right)\left(t_{n-1/2} - t_{n-1}\right)}\left\{\sin\left(\omega t\right) - \sin\left(\omega t_{n-1/2}\right)\right\}, \tag{74}$$

$$\tilde{N}_{t_3} = N_{t_3}\Psi_3 = \frac{\left(t - t_{n-1}\right)\left(t - t_{n-1/2}\right)}{\left(t_n - t_{n-1}\right)\left(t_n - t_{n-1/2}\right)}\left\{\sin\left(\omega t\right) - \sin\left(\omega t_n\right)\right\}. \tag{75}$$

Figure 6 shows the comparison of the regular and enriched shape function. This sinusoidal enrichment captures the deformation of cyclic loading with large time step and enables us to do direct numerical simulation of high cycle fatigue problem by coupling XTFEM with the two scale damage model [39].

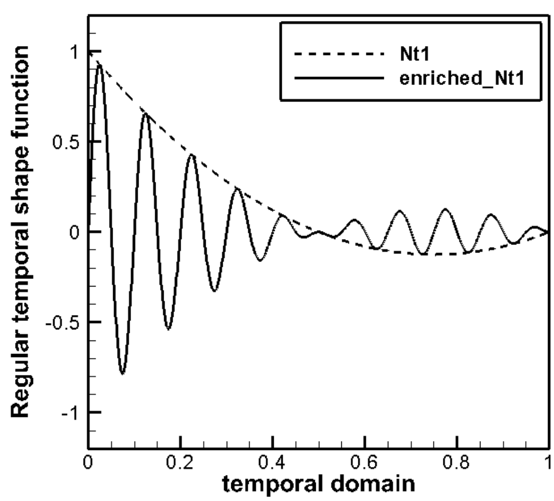

Figure 6. Regular and enriched temporal shape function (The example case: $\tilde{N}_{t_1}(t) = N_{t_1}(t)\left\{\sin\left(20\pi t\right) - \sin\left(20\pi t_1\right)\right\}$)

By assuming linear elastic material and discretizing TDG weak form with sinusoidal temporal enrichment shape function, we can derive the form of linear system below, using the similar procedure outlined in section 2.1 and 2.2.

$$\begin{bmatrix} \left(\int_{I_n} \begin{bmatrix} \dot{\mathbf{N}}_t^T \\ \dot{\tilde{\mathbf{N}}}_t^T \end{bmatrix} \begin{bmatrix} \ddot{\mathbf{N}}_t & \ddot{\tilde{\mathbf{N}}}_t \end{bmatrix} dt + \begin{bmatrix} \dot{\mathbf{N}}_t^T \left(t_{n-1}^+\right) \\ \dot{\tilde{\mathbf{N}}}_t^T \left(t_{n-1}^+\right) \end{bmatrix} \begin{bmatrix} \dot{\mathbf{N}}_t \left(t_{n-1}^+\right) & \dot{\tilde{\mathbf{N}}}_t \left(t_{n-1}^+\right) \end{bmatrix} \right) \otimes \mathbf{M} \\ + \left(\int_{I_n} \begin{bmatrix} \dot{\mathbf{N}}_t^T \\ \dot{\tilde{\mathbf{N}}}_t^T \end{bmatrix} \begin{bmatrix} \mathbf{N}_t & \tilde{\mathbf{N}}_t \end{bmatrix} dt + \begin{bmatrix} \mathbf{N}_t^T \left(t_{n-1}^+\right) \\ \tilde{\mathbf{N}}_t^T \left(t_{n-1}^+\right) \end{bmatrix} \begin{bmatrix} \mathbf{N}_t \left(t_{n-1}^+\right) & \tilde{\mathbf{N}}_t \left(t_{n-1}^+\right) \end{bmatrix} \right) \otimes \mathbf{K} \end{bmatrix} \begin{Bmatrix} \mathbf{d}_n \\ \mathbf{a}_n \end{Bmatrix}$$
$$= \begin{Bmatrix} \int_{\gamma_n} \begin{bmatrix} \dot{\mathbf{N}} & \dot{\tilde{\mathbf{N}}} \end{bmatrix}^T \cdot \mathbf{t} d\gamma + \int_{Q_n} \begin{bmatrix} \dot{\mathbf{N}} & \dot{\tilde{\mathbf{N}}} \end{bmatrix}^T \cdot \rho \mathbf{b} dQ \\ + \begin{pmatrix} \begin{bmatrix} \dot{\mathbf{N}}_t^T \left(t_{n-1}^+\right) \\ \dot{\tilde{\mathbf{N}}}_t^T \left(t_{n-1}^+\right) \end{bmatrix} \begin{bmatrix} \dot{\mathbf{N}}_t \left(t_{n-1}^-\right) & \dot{\tilde{\mathbf{N}}}_t \left(t_{n-1}^-\right) \end{bmatrix} \otimes \mathbf{M} \\ + \begin{bmatrix} \mathbf{N}_t^T \left(t_{n-1}^+\right) \\ \tilde{\mathbf{N}}_t^T \left(t_{n-1}^+\right) \end{bmatrix} \begin{bmatrix} \mathbf{N}_t \left(t_{n-1}^-\right) & \tilde{\mathbf{N}}_t \left(t_{n-1}^-\right) \end{bmatrix} \otimes \mathbf{K} \end{pmatrix} \begin{Bmatrix} \mathbf{d}_{n-1} \\ \mathbf{a}_{n-1} \end{Bmatrix} \end{Bmatrix} . \tag{76}$$

Again, $\mathbf{M}$ and $\mathbf{K}$ are spatial mass matrix and stiffness matrix. Equation (76) can be simplified as

$$\begin{bmatrix} \mathscr{K}_{rr} & \mathscr{K}_{re} \\ \mathscr{K}_{er} & \mathscr{K}_{ee} \end{bmatrix} \begin{Bmatrix} \mathbf{d}_n \\ \mathbf{a}_n \end{Bmatrix} = \begin{Bmatrix} \mathscr{F}_r \\ \mathscr{F}_e \end{Bmatrix}, \tag{77}$$

where the subscript "*r*" and "*e*" indicate regular and enriched part. $\mathscr{K}_{rr}$ is same as the space-time stiffness matrix $\mathscr{K}$ shown in equation (31). The other block matrices in LHS and force vectors in RHS include derivatives and integrations with enriched terms and the expressions can be complicated depending on the enrichment function. In some cases, they can be evaluated analytically. If the enrichment function is too complicated to get the exact form, we can still evaluate them by numerical integration.

The approach shown in equation (76) is limited to the case of linear elastic material with sinusoidal loading. In the case of nonlinear material, the cyclic response cannot be captured by single enrichment function even if the loading is given as exact sinusoidal. In this case, the displacement field is approximated by using superposition of multiple sinusoidal functions with different angular frequency like Fourier series. With the use of multiple enrichment functions, the enriched temporal shape function is given as,

$$\left[\mathbf{N}_t^{en}\right]=\left[\mathbf{N}_t \quad \tilde{\mathbf{N}}_t^1 \quad \tilde{\mathbf{N}}_t^2 \quad \cdots\right] \tag{78}$$

$$\tilde{N}_{t_i}^m = N_{t_i}\Psi_i^m\left(t\right) \tag{79}$$

For cyclic response of nonlinear material, the enrichment function can be chosen as, for example,

$$\Psi_i^m\left(t\right)=\sin\left(m\omega t\right)-\sin\left(m\omega t_i\right), \tag{80}$$

or

$$\Psi_i^m\left(t\right)=\cos\left(m\omega t\right)-\cos\left(m\omega t_i\right). \tag{81}$$

The interpolation of displacement is then given as,

$$\mathbf{u}^h\left(\mathbf{X},t\right)=\sum_{I=1}^{n_s}\mathbf{N}_I\left(\mathbf{X},t\right)\mathbf{d}_I+\sum_{J=1}^{n_e^1}\tilde{\mathbf{N}}_J^1\left(\mathbf{X},t\right)\mathbf{a}_J^1+\sum_{J=1}^{n_e^2}\tilde{\mathbf{N}}_J^2\left(\mathbf{X},t\right)\mathbf{a}_J^2+\cdots \tag{82}$$

CHAPTER 3

CONSTITUTIVE MODEL FOR RUBBER

3.1 Linear elastic material

The linear elastic constitutive law is widely used for many kind of materials and the detail of theory can be shown, for example, in [55, 56].

Generally, the linear elastic constitutive low is known as Hooke's law

$$\boldsymbol{\sigma} = \mathbf{C} : \boldsymbol{\varepsilon} \tag{83}$$

where $\boldsymbol{\sigma}$ is the Cauchy stress tensor, $\boldsymbol{\varepsilon}$ is infinitesimal strain tensor and $\mathbf{C}$ is the fourth order elasticity tensor. If the material is isotropic,

$$C_{ijkl} = \lambda \delta_{ij} \delta_{kl} + \mu \left(\delta_{ik} \delta_{jl} + \delta_{il} \delta_{jk} \right) \tag{84}$$

where λ and μ are Lamé's constants. It is also known that the constitutive model can be expressed by the combination of two constants from Young' modulus E, Poisson's ratio ν, Bulk modulus K and two Lamé's constants. In the case of rubber, ν is very close to a half and K becomes very large because rubber shows high incompressibility.

In the case of 2D plane condition, the Hooke's law can be simplified as followings.

Plane stress condition ($\sigma_{zz} = 0$):

$$\begin{Bmatrix} \sigma_{xx} \\ \sigma_{yy} \\ \tau_{xy} \end{Bmatrix} = \frac{E}{1-\nu^2} \begin{bmatrix} 1 & \nu & 0 \\ \nu & 1 & 0 \\ 0 & 0 & \dfrac{1-\nu}{2} \end{bmatrix} \begin{Bmatrix} \varepsilon_{xx} \\ \varepsilon_{yy} \\ \gamma_{xy} \end{Bmatrix}. \tag{85}$$

Plane strain condition ($\varepsilon_{zz} = 0$):

$$\begin{Bmatrix} \sigma_{xx} \\ \sigma_{yy} \\ \tau_{xy} \end{Bmatrix} = \frac{E}{(1+\nu)(1-2\nu)} \begin{bmatrix} 1-\nu & \nu & 0 \\ \nu & 1-\nu & 0 \\ 0 & 0 & \frac{1-2\nu}{2} \end{bmatrix} \begin{Bmatrix} \varepsilon_{xx} \\ \varepsilon_{yy} \\ \gamma_{xy} \end{Bmatrix}. \tag{86}$$

where γ_{xy} is the engineering shear strain.

3.2 Hyperelastic material

The theory of the hyperelastic constitutive model is briefly reviewed in this section. Reviewing of constitutive models of rubber elasticity can be found in Boyce and Arruda [13]. Firstly, Rivlin and Saunders [14] developed a hyperelastic constitutive model by using polynomial form of invariants of the stretch tensor as the strain energy potential.

$$W = \sum_{i,j}^{\infty} C_{ij} \left(I_1 - 3\right)^i \left(I_2 - 3\right)^j \tag{87}$$

where C_{ij} is the constant, I_i is the invariant of the right Cauchy Green deformation tensor $\mathbf{C} = \mathbf{F}^T\mathbf{F}$, and $\mathbf{F}$ is the deformation gradient tensor. Invariant I_i can be expressed by combination of principal stretches.

$$\begin{aligned} I_1 &= \mathrm{tr}(\mathbf{C}) \\ &= \lambda_1^2 + \lambda_2^2 + \lambda_3^2 \end{aligned}, \tag{88}$$

$$\begin{aligned} I_2 &= \frac{1}{2}\left[\left\{\mathrm{tr}(\mathbf{C})\right\}^2 - \mathrm{tr}\left(\mathbf{C}^2\right)\right] \\ &= \lambda_1^2\lambda_2^2 + \lambda_2^2\lambda_3^2 + \lambda_3^2\lambda_1^2 \end{aligned}, \tag{89}$$

$$\begin{aligned} I_3 &= \det(\mathbf{C}) \\ &= \left\{\det(\mathbf{F})\right\}^2 . \\ &= \lambda_1^2 \lambda_2^2 \lambda_3^2 \end{aligned} \tag{90}$$

If the material is completely incompressible, $I_3 = 1$ so that I_3 does not appear in equation (87).

The Neo-Hookean model is the simplest form and uses only one term of equation (87).

$$W = C_{10}\left(I_1 - 3\right). \tag{91}$$

The Neo-Hookean model can be considered as extension of Hooke's law to finite strain.

Mooney-Rivlin model [14, 15] is one of the most widely used model that has been used for elastomers. It is described as a combination of first order terms of I_1 and I_2.

$$W = C_{10}\left(I_1 - 3\right) + C_{01}\left(I_2 - 3\right). \tag{92}$$

In Yeoh model [16], the strain energy potential is given as a cubic form of I_1.

$$W = \sum_{i=1}^{3} C_{i0}\left(I_1 - 3\right)^i . \tag{93}$$

Ogden [17, 18] extended the polynomial form of the strain energy (87) to the series of non-integer order principal stretches,

$$W = \sum_{n=1}^{N} \frac{\mu_n}{\alpha_n}\left(\lambda_1^{\alpha_n} + \lambda_2^{\alpha_n} + \lambda_3^{\alpha_n} - 3\right) \tag{94}$$

where N is number of terms, μ_n and α_n are constants. It can be said that Neo-Hookean model is the case of $N = 1$ and $\alpha_1 = 1$.Also, the Mooney-Rivlin model is that of $N = 2$, $\alpha_1 = 2$ and $\alpha_2 = -2$. Therefore, these two models are included in the Ogden model.

Arruda and Boyce [19] proposed the stretch based model known as the 8-chain model, since it has been developed by introducing a cubic model with eight springs that are connected with its center and corners.

$$W = \mu \sum_{i=1}^{5} \frac{C_i}{\lambda_m^{2i-2}} \left(I_1^i - 3^i \right) \tag{95}$$

where μ is a constant, $C_1 = 1/2$, $C_2 = 1/20$, $C_3 = 11/1050$, $C_4 = 19/7000$ and $C_5 = 519/673750$. The coefficient λ_m is called locking stretch because the stress-strain curve slope rises drastically. The initial shear modulus μ_0 is given as

$$\mu_0 = \mu \left(1 + \frac{3}{5\lambda_m^2} + \frac{99}{175\lambda_m^4} + \frac{513}{875\lambda_m^6} + \frac{42039}{67635\lambda_m^8} \right) \tag{96}$$

and $\lambda_m = 7$ is often used as a typical value [22].

From the strain energy potential of hyperelastic constitutive law, the second Piola-Kirchhoff stress tensor $\mathbf{S}$ is computed as below. (See the detail in [51]).

$$\begin{aligned} \mathbf{S} &= \frac{\partial W}{\partial \mathbf{E}} \\ &= 2\frac{\partial W}{\partial \mathbf{C}} \end{aligned} \tag{97}$$

where $\mathbf{E} = \frac{1}{2}(\mathbf{C} - \mathbf{1})$ is the Green strain tensor and again $\mathbf{C}$ is the right Cauchy Green deformation tensor. By using the chain rule, we obtain

$$\begin{aligned} \mathbf{S} &= 2\frac{\partial W}{\partial \mathbf{C}} \\ &= 2\left\{ \frac{\partial W}{\partial I_1}\frac{\partial I_1}{\partial \mathbf{C}} + \frac{\partial W}{\partial I_2}\frac{\partial I_2}{\partial \mathbf{C}} + \frac{\partial W}{\partial I_3}\frac{\partial I_3}{\partial \mathbf{C}} \right\}. \end{aligned} \tag{98}$$

We can recall the properties of the derivatives of invariants,

$$\frac{\partial I_1}{\partial \mathbf{C}} = \mathbf{1}, \tag{99}$$

$$\frac{\partial I_2}{\partial \mathbf{C}} = I_1 \mathbf{1} - \mathbf{C}^T, \tag{100}$$

$$\frac{\partial I_3}{\partial \mathbf{C}} = I_3 \mathbf{C}^{-T}, \tag{101}$$

and then, we obtain the final expression of $\mathbf{S}$. We can also obtain Cauchy stress tensor $\boldsymbol{\sigma}$ and nominal stress tensor $\mathbf{P}$ by using following equations of conversion.

$$\boldsymbol{\sigma} = J^{-1} \mathbf{F} \cdot \mathbf{S} \cdot \mathbf{F}^T \tag{102}$$

$$\mathbf{P} = \frac{\partial W}{\partial \mathbf{F}^T} = \frac{\partial W}{\partial \mathbf{C}} : \frac{\partial \mathbf{C}}{\partial \mathbf{F}^T} = \mathbf{S} \cdot \mathbf{F}^T \tag{103}$$

For example, by substituting Mooney-Rivlin model (92) into equation (98), we have

$$\mathbf{S} = 2\left\{ C_{10} \mathbf{1} + C_{01} \left(I_1 \mathbf{1} - \mathbf{C} \right) \right\}. \tag{104}$$

At the undeformed condition so that $\mathbf{C} = \mathbf{1}$ and $I_1 = 3$, we obtain

$$\mathbf{S} = 2\left(C_{10} + 2C_{01} \right) \mathbf{1}. \tag{105}$$

This means the stress value is not zero in the case of no deformation and it is inconsistent obviously. To avoid this problem, several modification methods are proposed [13]. In this work, the following modified Mooney-Rivlin model is used and this model is also used in the commercial FEM software ABAQUS [22]. In the modified model, the strain energy potential is given as

$$\begin{aligned} W(\mathbf{C}) &= \overline{W}\left(\overline{\mathbf{C}}\right) + U(J) \\ &= C_{10}\left(\overline{I}_1 - 3\right) + C_{01}\left(\overline{I}_2 - 3\right) + \frac{1}{2} k \left(J - 1\right)^2 \end{aligned}, \tag{106}$$

$$\bar{\mathbf{C}} = \bar{\mathbf{F}}^T \bar{\mathbf{F}}, \tag{107}$$

$$\bar{\mathbf{F}} = J^{-\frac{1}{3}} \mathbf{F}, \tag{108}$$

where $J = \det \mathbf{F}$, $\bar{I}_1$ and $\bar{I}_2$ are two invariants of $\bar{\mathbf{C}}$. Since $\det\left(\bar{\mathbf{F}}\right) = 1$, $\bar{W}\left(\bar{\mathbf{C}}\right)$ does not depend on volume change J and is called the isovolumetric part of the strain energy density. On the other hand, $U\left(J\right)$ is considered as volume changing part. k is also a constant and a large number is chosen to enforce quasi-incompressibility.

3.3 Finite strain viscoelastic model

Simo's finite strain viscoelastic material model [23] has already been implemented in some FEM commercial codes [22]. In this section, this model is briefly reviewed. The details of the theory are described in [23]. For this finite strain viscoelastic model, the strain energy potential for instantaneous responses $W_0\left(\mathbf{C}\right)$ is given as arbitrary hyperelastic constitutive model. The hyperelastic constitutive law is combined with the Prony series, given as

$$\gamma\left(t\right) = \gamma_\infty + \sum_{i=1}^{N} \gamma_i \exp\left(-\frac{t}{\tau_i}\right), \tag{109}$$

$$\gamma_\infty + \sum_{i=1}^{N} \gamma_i = 1, \quad 0 \le \gamma_\infty \le 1, \quad 0 \le \gamma_i \le 1, \tag{110}$$

where γ_∞ and γ_i are parameters of Prony series and τ_i is the relaxation time. We can consider that $\gamma_\infty = 1$ and $\gamma_i = 0$ for hyperelastic case.

The second Piola-Kirchhoff stress tensor $\mathbf{S}$ is given as below by introducing internal variable tensors $\mathbf{Q}_i$ with regard to viscos parts.

$$\mathbf{S} = \mathbf{S}_0 - J^{-\frac{2}{3}} \,\mathrm{DEV}\left[\sum_{i=1}^{N} \mathbf{Q}_i\right], \tag{111}$$

$$\mathbf{S}_0 = 2\frac{\partial W_0}{\partial \mathbf{C}}, \tag{112}$$

$$\dot{\mathbf{Q}}_i + \frac{1}{\tau_i}\mathbf{Q}_i = \frac{\gamma_i}{\tau_i}\mathrm{DEV}\left[2\frac{\partial \bar{W}_0\left(\bar{\mathbf{C}}\right)}{\partial \bar{\mathbf{C}}}\right], \quad \mathbf{Q}_i\big|_{t=0} = \mathbf{0}, \tag{113}$$

$$\mathrm{DEV}\left[\bullet\right] = \left(\bullet\right) - \frac{1}{3}\left\{\mathbf{C}:\left(\bullet\right)\right\}\mathbf{C}^{-1}, \tag{114}$$

where the hyperelastic strain energy potential $W_0\left(\mathbf{C}\right)$ can be decomposed into the isovolumetric and volume changing part similar to equation (106), so that

$$W_0\left(\mathbf{C}\right) = \bar{W}_0\left(\bar{\mathbf{C}}\right) + U_0\left(J\right). \tag{115}$$

By solving (113) and substituting $\mathbf{Q}_i$ into (111), the final form of the second Piola-Kirchhoff stress tensor $\mathbf{S}$ is given as,

$$\mathbf{S} = J\frac{dU_0}{dJ}\mathbf{C}^{-1} + \gamma_\infty J^{-\frac{2}{3}}\,\mathrm{DEV}\left[2\frac{\partial \bar{W}_0\left(\bar{\mathbf{C}}\right)}{\partial \bar{\mathbf{C}}}\right] + J^{-\frac{2}{3}}\,\mathrm{DEV}\left[\sum_{i=1}^{N}\gamma_i \mathbf{H}_i\right], \tag{116}$$

$$\mathbf{H}_i = \int_0^t \exp\left(-\frac{t-\xi}{\tau_i}\right)\frac{d}{d\xi}\left\{\mathrm{DEV}\left[2\frac{\partial \bar{W}_0\left(\bar{\mathbf{C}}\right)}{\partial \bar{\mathbf{C}}}\right]\right\}d\xi, \tag{117}$$

or

$$\mathbf{S} = J\frac{dU_0}{dJ}\mathbf{C}^{-1} + J^{-\frac{2}{3}}\,\mathrm{DEV}\left[\int_0^t \gamma\left(t-\xi\right)\frac{d}{d\xi}\left\{\mathrm{DEV}\left[2\frac{\partial \bar{W}_0\left(\bar{\mathbf{C}}\right)}{\partial \bar{\mathbf{C}}}\right]\right\}d\xi\right]. \tag{118}$$

To avoid cumbersome computation of convolution integral, the tensor $\mathbf{H}_i$ in equation (117) is updated by following equation.

$$
\begin{aligned}
\mathbf{H}_i(t+\Delta t) &= \int_0^{t+\Delta t} \exp\left(-\frac{t+\Delta t-\xi}{\tau_i}\right)\frac{d}{d\xi}\left\{\mathrm{DEV}\left[2\frac{\partial \bar{W}_0\left(\bar{\mathbf{C}}(\xi)\right)}{\partial \bar{\mathbf{C}}}\right]\right\}d\xi \\
&= \mathbf{H}_i(t)\cdot\exp\left(-\frac{\Delta t}{\tau_i}\right)+\int_t^{t+\Delta t} \exp\left(-\frac{t+\Delta t-\xi}{\tau_i}\right)\frac{d}{d\xi}\left\{\mathrm{DEV}\left[2\frac{\partial \bar{W}_0\left(\bar{\mathbf{C}}(\xi)\right)}{\partial \bar{\mathbf{C}}}\right]\right\}d\xi \\
&\cong \mathbf{H}_i(t)\cdot\exp\left(-\frac{\Delta t}{\tau_i}\right)+\int_t^{t+\Delta t} \exp\left(-\frac{t+\Delta t-\xi}{\tau_i}\right)d\xi\cdot\left\{\begin{array}{l}\mathrm{DEV}\left[2\dfrac{\partial \bar{W}_0\left(\bar{\mathbf{C}}(t+\Delta t)\right)}{\partial \bar{\mathbf{C}}}\right] \\ -\mathrm{DEV}\left[2\dfrac{\partial \bar{W}_0\left(\bar{\mathbf{C}}(t)\right)}{\partial \bar{\mathbf{C}}}\right]\end{array}\right\}\frac{1}{\Delta t} \\
&\cong \mathbf{H}_i(t)\cdot\exp\left(-\frac{\Delta t}{\tau_i}\right)+\exp\left(-\frac{\Delta t}{2\tau_i}\right)\cdot\left\{\mathrm{DEV}\left[2\frac{\partial \bar{W}_0\left(\bar{\mathbf{C}}(t+\Delta t)\right)}{\partial \bar{\mathbf{C}}}\right]-\mathrm{DEV}\left[2\frac{\partial \bar{W}_0\left(\bar{\mathbf{C}}(t)\right)}{\partial \bar{\mathbf{C}}}\right]\right\}
\end{aligned} \tag{119}
$$

Note that the mean value theorem evaluates the derivative in the first approximation. Also, the midpoint rule integration is used in the second approximation. By using equation (119), $\mathbf{H}_i$ can be updated gradually.

3.4 Damage model based on continuous damage mechanics

Rubber often shows mechanical behaviors that are due to the damage from the previous loading history. Mullins effect [11] is one of the most well-known and studied phenomena in rubbery material. The continuum damage mechanics (CDM) theory can be applied for fatigue modeling by expressing damage evolution as a function of either time or load cycles. Kachanov [57] established CDM by correlating the damage at micro-scale to macro-scale through damage variables. Lemaitre developed damage theory within the exiting elastoplastic framework and proposed model for ductile failure [8, 58]. Applications of CDM approaches for rubbery can be found in material [23, 59]. In this work, an attempt has been made in incorporating CDM model developed by Cantournet and Desmorat [9, 10] into space-time FEM. The details of the theory is described in [10]. The formulation of CDM for damage and fatigue of elastomers is briefly outlined here.

The potential energy of hyperelasticity with internal friction coupled with damage is given as,

$$W = (1-D)\left\{W_1(\mathbf{E}) + W_2\left(\mathbf{E}-\mathbf{E}^{\pi}\right)\right\} + \frac{1}{2}C_x \boldsymbol{\alpha}:\boldsymbol{\alpha} \tag{120}$$

where $W_1(\mathbf{E})$ is a hyperelastic energy potential and $\mathbf{E}$ is the Green-Lagrange strain tensor. It can be seen that W_1 can be equivalently expressed as a function of the Right Cauchy-Green tensor. In this case, the modified Mooney-Rivlin model (106) has been introduced for W_1. The term $W_2\left(\mathbf{E}-\mathbf{E}^{\pi}\right)$ is a second order term of the energy potential and depends on $\mathbf{E}$ and inelastic strain $\mathbf{E}^{\pi}$. C_x is material parameter and $\boldsymbol{\alpha}$ is introduced as internal sliding variable. D is defined as the isotropic damage variable and $0 \le D \le D_c < 1$ where D_c is the damage value at the failure. The term $W_2\left(\mathbf{E}-\mathbf{E}^{\pi}\right)$ is further expressed as

$$\begin{aligned} W_2\left(\mathbf{E}-\mathbf{E}^{\pi}\right) &= 4C_{20}\left\{\mathrm{tr}\left(\mathbf{E}-\mathbf{E}^{\pi}\right)\right\}^2 \\ &= C_{20}\left\{I_1 - 2\,\mathrm{tr}\left(\mathbf{E}^{\pi}\right) - 3\right\}^2 . \end{aligned} \tag{121}$$

Here C_{20} is a material parameter. $\mathbf{E}$, $\mathbf{E}^{\pi}$, $\boldsymbol{\alpha}$ and D are state variables. $\mathbf{E}$ is observable and the others are internal variables. The constitutive equations between a state variable $\mathbf{A}$ and an associated variable $\mathbf{B}$ are given as $\mathbf{B} = \frac{\partial W}{\partial \mathbf{A}}$. Then, we have

$$\mathbf{S} = \frac{\partial W}{\partial \mathbf{E}} = (1-D)\frac{\partial\left(W_1 + W_2\right)}{\partial \mathbf{E}} \ , \tag{122}$$

$$\mathbf{S}^{\pi} = -\frac{\partial W}{\partial \mathbf{E}^{\pi}} = (1-D)\frac{\partial W_2}{\partial \mathbf{E}}, \tag{123}$$

$$\mathbf{Q} = \frac{\partial W}{\partial \boldsymbol{\alpha}} = C_x \boldsymbol{\alpha}, \tag{124}$$

$$Y = -\frac{\partial W}{\partial D} = W_1 + W_2, \tag{125}$$

where $\mathbf{S}^{\pi}$ is the stress tensor associated with $\mathbf{E}^{\pi}$, $\mathbf{Q}$ is the residual micro-stress tensor and Y is the energy density release rate. The sets of state variables and associated variables are summarized in Table 1. By substituting equation (121) into (123), we also have

$$\begin{aligned} \mathbf{S}^{\pi} &= 8C_{20}(1-D)\,\mathrm{tr}\left(\mathbf{E}-\mathbf{E}^{\pi}\right)\mathbf{1} \\ &= 4C_{20}(1-D)\left\{I_1 - 2\,\mathrm{tr}\left(\mathbf{E}^{\pi}\right) - 3\right\}\mathbf{1} \end{aligned}. \tag{126}$$

This means that the stress tensor $\mathbf{S}^{\pi}$ associated with inelastic strain $\mathbf{E}^{\pi}$ is given as isotropic tensor in this case.

Table 1. Sets of state variables and associated variables

Mechanism	Type	State variables $\mathbf{A}$		Associated variables $\mathbf{B}$
		Observable	Internal	
Elasticity	Tensor	$\mathbf{E}$ Green Lagrange strain	---	$\mathbf{S}$ The second Piola-Kirchhoff stress
Internal sliding	Tensor	---	$\mathbf{E}^{\pi}$ Inelastic strain	$-\mathbf{S}^{\pi}$
	Tensor	---	$\boldsymbol{\alpha}$	$\mathbf{Q}$ Micro residual stress
Damage	Scalar	---	D Fatigue damage	$-Y$ Energy density release late

Furthermore, the reversibility criterion is given as

$$\begin{aligned} f &= \left\| \tilde{\mathbf{S}}^{\pi} - \mathbf{Q} \right\| - \sigma_s \\ &= \sqrt{\left(\tilde{\mathbf{S}}^{\pi} - \mathbf{Q}\right) : \left(\tilde{\mathbf{S}}^{\pi} - \mathbf{Q}\right)} - \sigma_s \end{aligned} \tag{127}$$

where σ_s is the reversibility limit and $\tilde{\mathbf{S}}^{\pi}$ is the effective stress of $\mathbf{S}^{\pi}$. $\tilde{\mathbf{S}}^{\pi}$ is defined as,

$$\tilde{\mathbf{S}}^{\pi} = \frac{\mathbf{S}^{\pi}}{1-D} \tag{128}$$

If the reversibility criterion satisfies the consistency condition $f = 0$ and $\dot{f} = 0$, then the internal friction occurs. Otherwise if $f < 0$ or $\dot{f} \neq 0$, then internal friction does not occur and the material stays hyperelastic.

The dissipation potential is defined as

$$F = f + F_{\mathbf{Q}} + F_D , \tag{129}$$

$$F_{\mathbf{Q}} = \frac{\gamma}{2C_x} \mathbf{Q} : \mathbf{Q} , \tag{130}$$

$$F_D = \frac{S}{(s+1)(1-D)} \left(\frac{Y}{S} \right)^{s+1} , \tag{131}$$

where γ, S and s are material parameters.

Evolutions laws of each internal variable can be derived from the normality rule

$\mathbf{A} = -\dot{\mu} \dfrac{\partial F}{\partial \mathbf{B}}$ as followings.

$$\dot{\mathbf{E}}^{\pi} = \dot{\mu} \frac{\partial F}{\partial \mathbf{S}^{\pi}} , \tag{132}$$

$$\dot{\boldsymbol{\alpha}} = -\dot{\mu} \frac{\partial F}{\partial \mathbf{Q}} , \tag{133}$$

$$\dot{D} = \dot{\mu}\frac{\partial F}{\partial Y}, \tag{134}$$

where $\dot{\mu}$ is the internal friction multiplier determined from the consistency condition. By substituting equation (129) into equations (132) to (134), we have

$$\dot{\mathbf{E}}^{\pi} = \frac{\dot{\mu}}{1-D}\frac{\tilde{\mathbf{S}}^{\pi} - \mathbf{Q}}{\left\|\tilde{\mathbf{S}}^{\pi} - \mathbf{Q}\right\|}, \tag{135}$$

$$\dot{\mathbf{Q}} = C_x\left(1-D\right)\dot{\mathbf{E}}^{\pi} - \gamma\dot{\mu}\mathbf{Q}, \tag{136}$$

$$\dot{D} = \frac{\dot{\mu}}{1-D}\left(\frac{Y}{S}\right)^{s}. \tag{137}$$

Also, if necessary, the cumulative measure π can be introduced.

$$\pi = \int_0^t \left\|\dot{\mathbf{E}}^{\pi}\right\| d\tau \tag{138}$$

If $\pi < \pi_D$, the damage evolution does not occur ($\dot{D} = 0$).

From equation (126), we can recall that $\mathbf{S}^{\pi}$ is an isotropic tensor. Then, by assuming $\mathbf{E}^{\pi} = \mathbf{0}$ and $\mathbf{Q} = \mathbf{0}$ at the initial state, and considering equations (124), (135) and (136), we can easily guess that the tensors related to internal sliding $\mathbf{E}^{\pi}$, $\boldsymbol{\alpha}$ and $\mathbf{Q}$ are all isotropic. So that,

$$\mathbf{E}^{\pi} = E^{\pi} \cdot \mathbf{1}, \tag{139}$$

$$\mathbf{Q} = Q \cdot \mathbf{1}, \tag{140}$$

$$\boldsymbol{\alpha} = \frac{Q}{C_x} \cdot \mathbf{1}, \tag{141}$$

where E^{π} and Q are scalar values. Since $\left\|\mathbf{1}\right\| = \sqrt{\mathbf{1}:\mathbf{1}} = \sqrt{3}$, equation (135) can be rewritten as

$$\dot{E}^{\pi} = \frac{\dot{\mu}}{\sqrt{3}(1-D)} \operatorname{sign}\left(\tilde{S}^{\pi} - Q\right) \tag{142}$$

where S^{π} is scalar so that $\mathbf{S}^{\pi} = S^{\pi} \cdot \mathbf{1}$. Also, equation (136) will be

$$\dot{Q} = C_x \left(1-D\right) \dot{E}^{\pi} - \gamma\dot{\mu}Q \,. \tag{143}$$

In addition, the reversibility criterion (127) can be written again,

$$\begin{aligned} f &= \left\|\tilde{\mathbf{S}}^{\pi} - \mathbf{Q}\right\| - \sigma_s \\ &= \sqrt{3} \cdot \left|\tilde{S}^{\pi} - Q\right| - \sigma_s \end{aligned} . \tag{144}$$

By checking equation (144), if $f < 0$, the material behaves hyperelastic and we do not need to consider internal variables evolution. Otherwise we should enforce it to satisfy the consistency condition $f = 0$, $\dot{f} = 0$ and equations (137), (142) and (143). The mid-point rule and Newton's method [52] are used to solve these equations numerically. Firstly, following residual equations are defined based on equations (142), (143) and (137).

$$g_{E^{\pi}} = \Delta E^{\pi} - \frac{\Delta\mu}{\sqrt{3}\left(1-D_{1/2}\right)} \operatorname{sign}\left(\tilde{S}^{\pi}_{1/2} - Q_{1/2}\right) = 0 \,, \tag{145}$$

$$g_Q = \Delta Q - C_x \left(1-D_{1/2}\right) \Delta E^{\pi} + \gamma Q_{1/2} \Delta\mu = 0 \,, \tag{146}$$

$$g_D = \Delta D - \frac{\Delta\mu}{1-D_{1/2}} \left(\frac{Y_{1/2}}{S}\right)^{s} = 0 \,. \tag{147}$$

Note that the subscripts and increment of each variable have following relationship.

$$\tilde{S}^{\pi}_{\theta} = \tilde{S}^{\pi}\left(\mathbf{E}_{\theta} - \mathbf{E}^{\pi}_{\theta}\right), \tag{148}$$

$$Y_{\theta} = W_1\left(\mathbf{E}_{\theta}\right) + W_2\left(\mathbf{E}_{\theta} - \mathbf{E}^{\pi}_{\theta}\right), \tag{149}$$

$$E_{\theta} = E_0 + \theta \cdot \Delta E \,, \tag{150}$$

$$E_{\theta}^{\pi} = E_0^{\pi} + \theta \cdot \Delta E^{\pi} , \tag{151}$$

$$Q_{\theta} = Q_0 + \theta \cdot \Delta Q , \tag{152}$$

$$D_{\theta} = D_0 + \theta \cdot \Delta D . \tag{153}$$

where $0 \le \theta \le 1$ and the subscript zero indicates the value from previous time step. Therefore, equations (145) to (147) require that the corresponding residuals become zero at the middle point of time step points ($\theta = \frac{1}{2}$) because mid-point rule gives more accurate results than Euler method. However, in the case of the consistency condition, $f = 0$ is solved at $\theta = 1$ because the condition should be satisfied at the end of time steps. So that,

$$g_f = \sqrt{3} \cdot \left| \tilde{S}_1^{\pi} - Q_1 \right| - \sigma_s = 0 . \tag{154}$$

If 2D plane stress condition is assumed, the component of the second Piola-Kirchhoff stress tensor in z -direction should be zero.

$$g_{S_{zz}} = S_{zz} = \frac{\partial W\left(\mathbf{E}_1, \mathbf{E}_1^{\pi}\right)}{\partial E_{zz}} = 0 . \tag{155}$$

Finally, we solve equations (145) to (147), (154) and (155). The undetermined variables in these equations are $\Delta\mu$, ΔE^{π}, ΔQ, ΔD and the increment of z -direction component of deformation gradient ΔF_{zz}. Then, we can define the residual vector $\mathbf{g}$ and the unknown variables vector $\mathbf{v}$ as below in the case of 2D plane stress condition.

$$\mathbf{g} = \begin{Bmatrix} g_{E^{\pi}} \\ g_Q \\ g_D \\ g_f \\ g_{S_{zz}} \end{Bmatrix} , \tag{156}$$

$$\mathbf{v} = \begin{Bmatrix} \Delta\mu \\ \Delta E^{\pi} \\ \Delta Q \\ \Delta D \\ \Delta F_{zz} \end{Bmatrix}. \tag{157}$$

By using Newton's method, $\mathbf{g} = \mathbf{0}$ can be solved.

$$\mathbf{v}_{m+1} = \mathbf{v}_m - \left[\frac{\partial \mathbf{g}}{\partial \mathbf{v}}\right]^{-1} \cdot \mathbf{g}, \tag{158}$$

where m indicates the number of step of the Newton's method. The iteration is repeated until the L2 norms $\|\mathbf{g}\|_2$ and $\|\Delta\mathbf{v}\|_2 = \|\mathbf{v}_{m+1} - \mathbf{v}_m\|$ become enough small.

In the case of fatigue damage computation, since the damage grows very slowly, the damage increment ΔD in unknown vector $\mathbf{v}$ (equation (157)) is often much smaller than the values of other unknowns. This causes instability in solving the equation because the Jacobian matrix of the Newton's method $\left[\frac{\partial \mathbf{g}}{\partial \mathbf{v}}\right]$ becomes very close to singular and the solution diverges in equation (158). To avoid this problem, the rows of g_D and ΔD can be removed from the residual vector $\mathbf{g}$ (equation (156)) and the unknown variables vector $\mathbf{v}$ (equation (157)). Then, the damage variable D can be integrated separately based on equations (147) and (153) after solving $\mathbf{g} = \mathbf{0}$ with the constant damage variable $D = D_0$. Alternatively, two-scale damage model approach can help to simplify the problem solution. The two-scale damage model was proposed by Lemaitre [60, 61]. In the two-scale damage model approach, it is assumed that the damage only occurs in micro scale region and it does not affect deformation in macro scale level. In this case, we can treat the damage D as zero in macro scale computation. Then, the damage evolution in micro scale is evaluated independently based on equations (147) and (153).

The following equations are the components of the Jacobian matrix $\left[\frac{\partial \mathbf{g}}{\partial \mathbf{v}}\right]$ with the constant damage $D = D_0$. If we use the two-scale damage model, D_0 can be replaced with zero.

$$\frac{\partial g_{E^\pi}}{\partial \Delta\mu} = -\frac{1}{\sqrt{3}\left(1-D_0\right)}\operatorname{sign}\left(\tilde{S}^\pi_{1/2} - Q_{1/2}\right), \tag{159}$$

$$\frac{\partial g_{E^\pi}}{\partial \Delta E^\pi} = 1, \tag{160}$$

$$\frac{\partial g_{E^\pi}}{\partial \Delta Q} = 0, \tag{161}$$

$$\frac{\partial g_{E^\pi}}{\partial \Delta F_{zz}} = 0, \tag{162}$$

$$\frac{\partial g_{Q}}{\partial \Delta\mu} = \gamma Q_{1/2}, \tag{163}$$

$$\frac{\partial g_{Q}}{\partial \Delta E^\pi} = -C_x\left(1-D_0\right), \tag{164}$$

$$\frac{\partial g_{Q}}{\partial \Delta Q} = 1 + \frac{1}{2}\gamma\Delta\mu, \tag{165}$$

$$\frac{\partial g_{Q}}{\partial \Delta F_{zz}} = 0, \tag{166}$$

$$\frac{\partial g_{f}}{\partial \Delta\mu} = 0, \tag{167}$$

$$\frac{\partial g_{f}}{\partial \Delta E^\pi} = -24\sqrt{3}C_{20}\cdot\operatorname{sign}\left(\tilde{S}^\pi_{1} - Q_{1}\right), \tag{168}$$

$$\frac{\partial g_f}{\partial \Delta Q} = -\sqrt{3} \cdot \operatorname{sign}\left(\tilde{S}_1^\pi - Q_1\right), \tag{169}$$

$$\frac{\partial g_f}{\partial \Delta F_{zz}} = 8\sqrt{3} C_{20} F_{zz}^1 \operatorname{sign}\left(\tilde{S}_1^\pi - Q_1\right), \tag{170}$$

$$\frac{\partial g_{S_{zz}}}{\partial \Delta \mu} = 0, \tag{171}$$

$$\frac{\partial g_{S_{zz}}}{\partial \Delta E^\pi} = -24 C_{20}, \tag{172}$$

$$\frac{\partial g_{S_{zz}}}{\partial \Delta Q} = 0, \tag{173}$$

$$\frac{\partial g_{S_{zz}}}{\partial \Delta F_{zz}} = \frac{\partial S_{zz}}{\partial \Delta F_{zz}}, \tag{174}$$

where F_{zz}^1 is the z component of deformation gradient at $\theta = 1$. The value of equation (174) depends on the hyperelastic constitutive model of $W_1(\mathbf{E})$. From equations (159) to (174), we can find that many components of Jacobian matrix $\left[\frac{\partial \mathbf{g}}{\partial \mathbf{v}}\right]$ are constant and we can easily derive the analytical form of inverse matrix $\left[\frac{\partial \mathbf{g}}{\partial \mathbf{v}}\right]^{-1}$. This leads to efficient implementation of the Newton iteration (158).

In summary, the computational algorithm for solving the combined hyperelastic/CDM model is given as follows:

1. At each quadrature point, compute $\tilde{\mathbf{S}}^\pi$ (equations (126) and (128)) based on the displacement solution at current step and $\mathbf{E}^\pi$, $\mathbf{Q}$ and D from the previous step

(calculated from 3. Case(ii) below).

2. Compute the reversibility criterion value f (equations (127) and (144)).

3. Case (i) $f \leq 0$.

There is no damage evolution and the material is assumed to be hyperelastic. Stress values are updated according to equation (122). No update is implemented for $\mathbf{E}^{\pi}$, $\mathbf{Q}$ and D.

Case (ii) $f > 0$.

Undetermined variables should be updated to satisfy the consistency condition $f = 0$ and $\dot{f} = 0$. This is accomplished by solving the residual vector $\mathbf{g} = \mathbf{0}$ (equation (156)) by using Newton's method (equation (158)) to get $\dot{\mathbf{E}}^{\pi}$, $\dot{\mathbf{Q}}$, $\dot{D}$ and $\dot{\mu}$. Update $\mathbf{E}^{\pi}$, $\mathbf{Q}$ and D according to the rates obtained.

4. Check if $D \geq D_c$. If this is the case, then crack is initiated. Otherwise damage will continue to evolve according to the constitutive solver.

CHAPTER 4

NON-ORDINARY STATE-BASED PERIDYNAMICS

4.1 Non-ordinary state-based peridynamics formulation

In this section, the theory of non-ordinary state-based peridynamics is reviewed. For detailed description on the subjects, we refer to [48, 62]. In non-ordinary state-based peridynamics theory, the deformation gradient and related stress values of each point are evaluated nonlocally by introducing subregion of the body called horizon $H_{\mathbf{X}}$. The horizon $H_{\mathbf{X}}$ is defined as a spherical region of the constant distance δ from the center material point $\mathbf{X}$. Then, the bond between two material points is defined as

$$\boldsymbol{\xi} = \mathbf{X}' - \mathbf{X}, \tag{175}$$

where $\mathbf{X}'$ is a material point in $H_{\mathbf{X}}$. Figure 7 shows the image of the bond and horizon in a body.

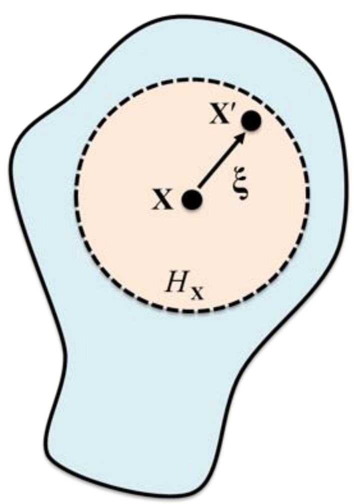

Figure 7. Bond $\boldsymbol{\xi}$ and horizon $H_{\mathbf{X}}$

Similarly, the deformation state $\underline{\mathbf{Y}}\langle\xi\rangle$ is defined as

$$\begin{aligned}\underline{\mathbf{Y}}\langle\xi\rangle &= \mathbf{x}'(\mathbf{X}',t)-\mathbf{x}(\mathbf{X},t)\\ &= \{\mathbf{X}'+\mathbf{u}'(\mathbf{X}',t)\}-\{\mathbf{X}+\mathbf{u}(\mathbf{X},t)\},\\ &= \boldsymbol{\xi}+\boldsymbol{\eta}\end{aligned} \tag{176}$$

where $\mathbf{x}$ and $\mathbf{x}'$ are deformed configuration of $\mathbf{X}$ and $\mathbf{X}'$, $\mathbf{u}$ and $\mathbf{u}'$ are displacement, and $\boldsymbol{\eta}=\mathbf{u}'-\mathbf{u}$. The deformation state $\underline{\mathbf{Y}}\langle\xi\rangle$ is the deformation image of the original bond $\boldsymbol{\xi}$.

Silling et al. [48] introduced peridynamics equation of motion as below.

$$\rho(\mathbf{X})\ddot{\mathbf{u}}(\mathbf{X},t)=\int_{H_{\mathbf{X}}}\left\{\underline{\mathbf{T}}[\mathbf{X},t]\langle\mathbf{X}'-\mathbf{X}\rangle-\underline{\mathbf{T}}[\mathbf{X}',t]\langle\mathbf{X}-\mathbf{X}'\rangle\right\}dV_{\mathbf{X}'}+\mathbf{b}(\mathbf{X},t), \tag{177}$$

where $\rho(\mathbf{X})$ and $\mathbf{b}(\mathbf{X},t)$ are the mass density and body force density field, $\underline{\mathbf{T}}[\mathbf{X},t]$ is the vector state called force state. By comparing equation (177) with the equation of motion for continuum (equation (1)), it is found that the term of partial derivative of stress tensor has been replaced with integration of force state. This allows us to avoid computing derivative near the discontinuous or singular point like crack and makes peridynamics more robust in predicting crack propagation.

In non-ordinary state-based peridynamics theory, the nonlocal deformation gradient $\bar{\mathbf{F}}(\mathbf{X},t)$ is given as nonlocal approximation of the deformation gradient based on the original bond $\boldsymbol{\xi}$ and the deformation state $\underline{\mathbf{Y}}\langle\xi\rangle$.

$$\bar{\mathbf{F}}(\mathbf{X},t)=\left[\int_{H_{\mathbf{X}}}\omega(|\xi|)\left(\underline{\mathbf{Y}}\langle\xi\rangle\otimes\xi\right)dV_{\mathbf{X}'}\right]\cdot\bar{\mathbf{K}}^{-1}(\mathbf{X}), \tag{178}$$

$$\bar{\mathbf{K}}(\mathbf{X})=\left[\int_{H_{\mathbf{X}}}\omega(|\xi|)(\xi\otimes\xi)dV_{\mathbf{X}'}\right], \tag{179}$$

where $\omega(|\xi|)$ is the influence function and it can express the effect of the original bond distance.

How to determine the influence function is still an ongoing research topic [63]. In many cases, the influence function is simply given as the unity. The symbol $\otimes$ denotes the dyadic product of vectors and $V_{\mathbf{X}'}$ is the volume associated with point $\mathbf{X}'$. $\bar{\mathbf{K}}(\mathbf{X})$ is the nonlocal shape tensor which is symmetric. Force state $\underline{\mathbf{T}}[\mathbf{X},t]$ is given as

$$\underline{\mathbf{T}}[\mathbf{X},t]\langle\mathbf{X}'-\mathbf{X}\rangle = \omega(|\mathbf{X}'-\mathbf{X}|)\bar{\mathbf{F}}\cdot\bar{\mathbf{S}}\cdot\bar{\mathbf{K}}^{-1}\cdot(\mathbf{X}'-\mathbf{X}), \tag{180}$$

where $\bar{\mathbf{S}}$ is the nonlocal second Piola-Kirchhoff strain tensor which is symmetric. Then, $\bar{\mathbf{F}}\cdot\bar{\mathbf{S}}$ can be considered as the nonlocal first Piola-Kirchhoff stress tensor [51]. $\bar{\mathbf{S}}$ or $\bar{\mathbf{F}}\cdot\bar{\mathbf{S}}$ can be evaluated by the material constitutive law and the nonlocal deformation gradient $\bar{\mathbf{F}}$.

4.2 Implementation of non-ordinary state-based peridynamics

In this section, the numerical implementation of the non-ordinary state-based peridynamics theory [62] is reviewed. At first, the nonlocal deformation gradient $\bar{\mathbf{F}}$ and nonlocal shape tensor $\bar{\mathbf{K}}$ given in (178) and (179) are discretized with regard to the particle j that is the center particle of horizon as follows.

$$\bar{\mathbf{F}}(\mathbf{X}_j,t) = \left[\sum_{n=1}^{m}\omega(|\mathbf{X}_n-\mathbf{X}_j|)\left\{\underline{\mathbf{Y}}\langle\mathbf{X}_n-\mathbf{X}_j\rangle\otimes(\mathbf{X}_n-\mathbf{X}_j)\right\}V_n\right]\cdot\bar{\mathbf{K}}^{-1}(\mathbf{X}_j) \tag{181}$$

$$\bar{\mathbf{K}}(\mathbf{X}_j) = \sum_{n=1}^{m}\omega(|\mathbf{X}_n-\mathbf{X}_j|)\left\{(\mathbf{X}_n-\mathbf{X}_j)\otimes(\mathbf{X}_n-\mathbf{X}_j)\right\}V_n \tag{182}$$

where m is the number of particles within the horizon of particle j.

Then, the equation of motion (177) is discretized as

$$\rho(\mathbf{X}_j)\ddot{\mathbf{u}}(\mathbf{X}_j,t) = \sum_{n=1}^{m}\left\{\underline{\mathbf{T}}[\mathbf{X}_j,t]\langle\mathbf{X}_n-\mathbf{X}_j\rangle - \underline{\mathbf{T}}[\mathbf{X}_n,t]\langle\mathbf{X}_j-\mathbf{X}_n\rangle\right\}V_n + \mathbf{b}(\mathbf{X}_j,t). \tag{183}$$

Finally, we obtain the acceleration vector $\ddot{\mathbf{u}}\left(\mathbf{X}_j, t\right)$ and update the velocity $\dot{\mathbf{u}}\left(\mathbf{X}_j, t\right)$ and displacement $\mathbf{u}\left(\mathbf{X}_j, t\right)$ by finite difference scheme like, for example, the central difference or velocity Verlet.

Silling and Askari [47] discussed how to estimate the critical time step size in the peridynamic model. The Courant-Friedrichs-Lewy (CFL) condition [64] can be used to estimate a proper maximum time step size, i.e., $\Delta t \le l/c$ where l is the particle spacing and c is the speed of sound in the solid.

4.3 Stabilization of non-ordinary state-based peridynamics

It is known that non-ordinary state-based peridynamics has an inherent problem called zero-energy mode. This is a phenomenon similar to that of finite element method, also called hour glass mode. The zero-energy mode causes instability in results. To control the zero-energy model, several approaches have been proposed, for example, in [65–68]. In this work, the stabilization method proposed by Silling [68] is used to reduce instability coming from zero-energy mode. Here, the theory of the stabilization is reviewed. The detail can be seen in [68].

At first, the nonuniform part of the deformation state $\underline{\mathbf{z}}\langle\xi\rangle$ is introduced as

$$\underline{\mathbf{z}}\langle\xi\rangle = \underline{\mathbf{Y}}\langle\xi\rangle - \bar{\mathbf{F}} \cdot \xi . \tag{184}$$

Recall that $\underline{\mathbf{Y}}\langle\xi\rangle$ is deformation state given by equation (176) and $\bar{\mathbf{F}}$ is the nonlocal deformation gradient in equation (178). From equations (178), (179) and (184), it can be seen that

$$
\begin{aligned}
&\left[\int_{H_{\mathbf{x}}} \omega(|\xi|)\left(\underline{\mathbf{z}}\langle\xi\rangle \otimes \xi\right) dV_{\mathbf{x}'}\right] \cdot \bar{\mathbf{K}}^{-1} \\
&=\left[\int_{H_{\mathbf{x}}} \omega(|\xi|)\left(\underline{\mathbf{Y}}\langle\xi\rangle \otimes \xi\right) dV_{\mathbf{x}'}\right] \cdot \bar{\mathbf{K}}^{-1}-\bar{\mathbf{F}} \cdot\left[\int_{H_{\mathbf{x}}} \omega(|\xi|)(\xi \otimes \xi) dV_{\mathbf{x}'}\right] \cdot \bar{\mathbf{K}}^{-1} . \\
&=\bar{\mathbf{F}}-\bar{\mathbf{F}} \cdot \bar{\mathbf{K}} \cdot \bar{\mathbf{K}}^{-1} \\
&=\mathbf{0}
\end{aligned}
\tag{185}
$$

This fact shows that the deformation state $\underline{\mathbf{Y}}\langle\xi\rangle$ is not unique even if the deformation gradient approximation $\bar{\mathbf{F}}$ is same.

In this stabilization method, the force vector state $\underline{\mathbf{T}}\langle\xi\rangle$ (equation (180)) is replaced with $\hat{\underline{\mathbf{T}}}\langle\xi\rangle$ and it is defined as

$$
\hat{\underline{\mathbf{T}}}\langle\xi\rangle=\omega(|\xi|)\left\{\bar{\mathbf{F}} \cdot \bar{\mathbf{S}} \cdot \bar{\mathbf{K}}^{-1} \cdot \xi+\frac{GC}{\omega_0} \underline{\mathbf{z}}\langle\xi\rangle\right\}, \tag{186}
$$

$$
\omega_0=\int_{H_{\mathbf{x}}} \omega(|\xi|) dV_{\mathbf{x}'}, \tag{187}
$$

where G is positive constant and C is given as follows [69].

$$
C=\begin{cases}
\dfrac{18k}{\pi\delta^4} & \text{if 3D} \\
\dfrac{12k'}{\pi h\delta^3} & \text{if 2D} \\
\dfrac{2E}{A\delta^2} & \text{if 1D}
\end{cases}, \tag{188}
$$

where δ is the radius of horizon, k is the bulk modulus, h is the thickness and A is the cross sectional area. Also, k' is the bulk modulus in 2D and given as

$$
k'=\begin{cases}
\dfrac{E}{2(1-\nu)} & \text{if plane stress} \\
\dfrac{E}{2(1+\nu)(1-2\nu)} & \text{if plane strain}
\end{cases}. \tag{189}
$$

CHAPTER 5

COUPLING PERIDYNAMICS WITH SPACE-TIME FEM

5.1 Multiscale crack propagation simulation by coupling non-ordinary state-based peridynamics coupling with space-time FEM

As shown in section 4.1, since peridynamics is nonlocal and partial derivative of stress tensor is replaced with integration of force state in the equation of motion in continuum (equation (177)), peridynamics can be employed for crack simulation. However, the computational cost is not small because we need to compute nonlocal deformation gradient as a value of combination of particles in each horizon. Therefore, to make computation more efficient, one solution is to couple peridynamics with FEM frame work, for example, in [49, 70]. In this work, the non-ordinary state-based peridynamics is coupled with space-time FEM based on the time discontinuous Galerkin formulation to solve dynamic crack propagation problems.

Here, the framework of coupling non-ordinary state-based peridynamics with space-time FEM is presented. For spatial domain, direct coupling between space-time FEM and non-ordinary state-based peridynamics is implemented. First of all, the whole spatial domain is discretized by finite elements. If there exists initial cracks, the elements with a crack are enriched by using XFEM methodology [45, 71]. In this work, the Heaviside step enrichment function (equations (67) to (70) in section 2.5) is applied to represent the crack in the global domain. Secondly, peridynamics simulation region overlaps the finite elements in the region surrounding the crack tip. The boundary conditions for peridynamics is obtained from the interpolation by using space-time FEM (equations (14) and (67)) shape functions in the patch region. The number of patch region layer is determined by considering the horizon size δ. Figure 8 shows an illustration of configuration of FEM mesh and peridynamics particles in the spatial domain. The advantage of using space-time FEM is that the shape functions can be employed to obtain the spatial and temporal information at any particle location within the problem domain. It is then possible to develop an adaptive scheme such as the NOPD simulation domain moves with the crack front.

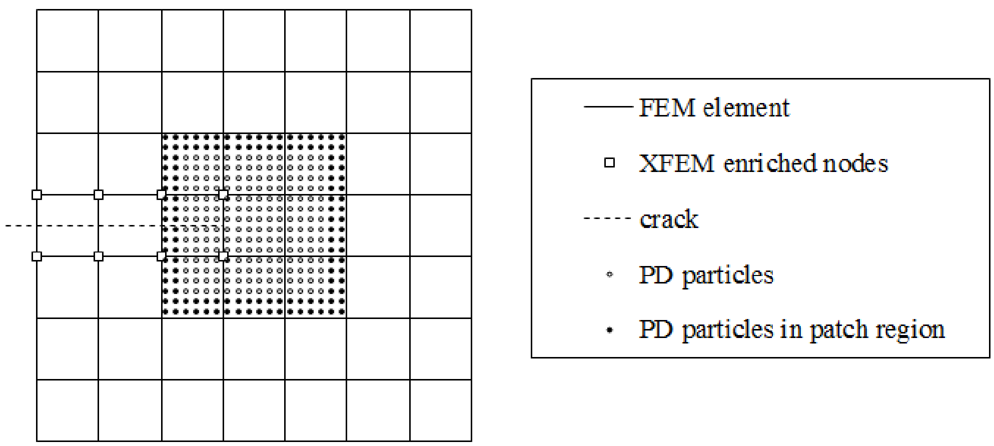

Figure 8. An illustration of coupling finite element and peridynamics region for a crack problem.

For temporal domain, time subcyling is used in which two different time increments are used for space-time FEM and peridynamics. At first, a temporal domain for space-time FEM is assumed as $I_n =]t_{n-1}, t_n[$ and the time increment is defined as $\Delta t_{ST} = t_n - t_{n-1}$. Then, we divide Δt_{ST} into m subdomains and define $\Delta t_{PD} = \Delta t_{ST} / m$. Δt_{PD} is used for local peridynamics simulation. Figure 9 shows an image of the coupling of peridynamics and space-time FEM in temporal domain.

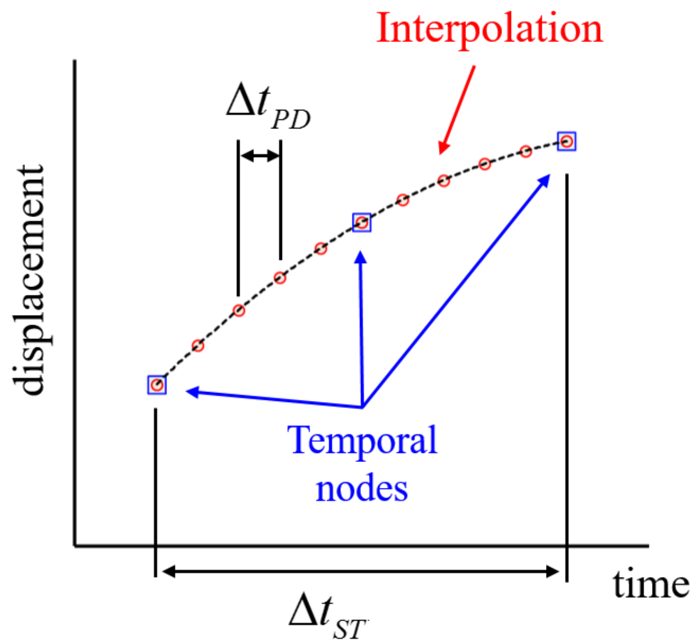

Figure 9. An illustration of coupling space-time FEM with peridynamics in temporal domain.

The crack propagation is predicted in peridynamics region based on the given boundary conditions from space-time FEM. If the crack grows over an element, the information of crack position is fed back to space-time FEM region and the XFEM enrichment is applied for the new cracked element. In addition, the coupled region will be advanced to be around the new crack tip. Figure 10 shows an image of crack propagation in FEM and peridynamics region.

5.2 Non-ordinary state-based peridynamics with the time integration based on time discontinuous Galerkin formulation

In this section, the peridynamics theory is coupled with space-time formulation based on the time discontinuous Galerkin (TDG) approach. The TDG formulation is already reviewed in chapter 2.

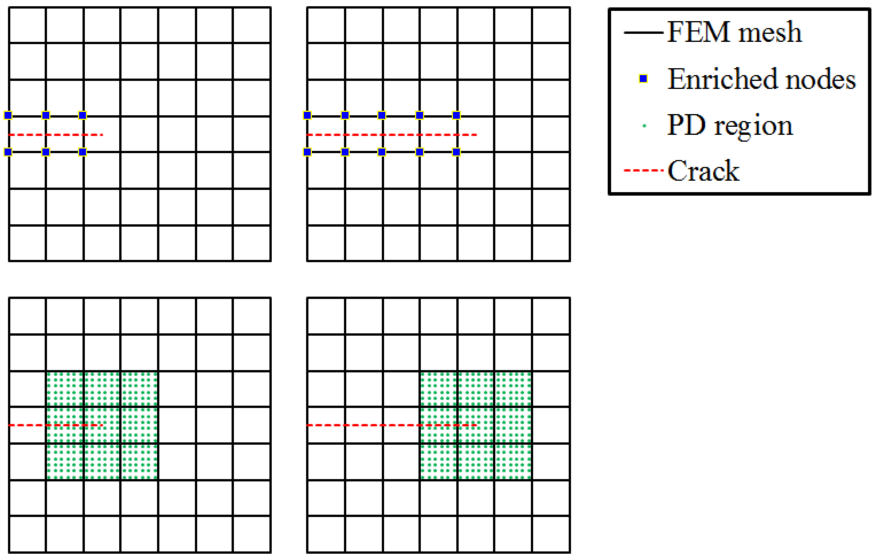

Figure 10. Image of crack propagation in coupling scheme.

From the weak form of the TDG formulation (10)-(12) and the non-ordinary state-based peridynamics equation of motion (177), the weak form for space-time peridynamics can be derived as

$$\begin{aligned}\mathbf{0} &= \mathbf{B}\left(\delta\mathbf{u}^h,\mathbf{u}^h\right)_n - \mathbf{L}\left(\delta\mathbf{u}^h\right)_n \\ &= \int_{Q_n}\delta\dot{\mathbf{u}}^h\cdot\rho\ddot{\mathbf{u}}^h dQ + \int_{Q_n}\delta\dot{\mathbf{u}}^h\cdot\left(-\mathbf{f}_{int}\right)dQ - \int_{Q_n}\delta\dot{\mathbf{u}}^h\cdot\mathbf{b}dQ \\ &+\delta\dot{\mathbf{u}}^h\left(t_{n-1}^+\right)\cdot\left[\!\left[\int_\Omega\rho\dot{\mathbf{u}}^h\left(t_{n-1}\right)d\Omega\right]\!\right] + \delta\mathbf{u}^h\left(t_{n-1}^+\right)\cdot\left[\!\left[\int_\Omega\left(-\mathbf{f}_{int}\left(t_{n-1}\right)\right)d\Omega\right]\!\right]\end{aligned}, \tag{190}$$

$$\begin{aligned}\mathbf{B}\left(\delta\mathbf{u}^h,\mathbf{u}^h\right)_n &= \int_{Q_n}\delta\dot{\mathbf{u}}^h\cdot\rho\ddot{\mathbf{u}}^h dQ + \int_{Q_n}\delta\dot{\mathbf{u}}^h\cdot\left(-\mathbf{f}_{int}\right)dQ \\ &+\delta\dot{\mathbf{u}}^h\left(t_{n-1}^+\right)\cdot\int_\Omega\rho\dot{\mathbf{u}}^h\left(t_{n-1}^+\right)d\Omega + \delta\mathbf{u}^h\left(t_{n-1}^+\right)\cdot\int_\Omega\left(-\mathbf{f}_{int}\left(t_{n-1}^+\right)\right)d\Omega\end{aligned}, \tag{191}$$

$$\begin{aligned}\mathbf{L}\left(\delta\mathbf{u}^h\right)_n &= \int_{Q_n}\delta\dot{\mathbf{u}}^h\cdot\mathbf{b}dQ \\ &+\delta\dot{\mathbf{u}}\left(t_{n-1}^+\right)\cdot\int_\Omega\rho\dot{\mathbf{u}}^h\left(t_{n-1}^-\right)d\Omega + \delta\mathbf{u}^h\left(t_{n-1}^+\right)\cdot\int_\Omega\left(-\mathbf{f}_{int}\left(t_{n-1}^-\right)\right)d\Omega\end{aligned}, \tag{192}$$

$$\mathbf{f}_{int} = \int_{H_\mathbf{X}}\left\{\mathbf{T}\left[\mathbf{X},t\right]\left\langle\mathbf{X}'-\mathbf{X}\right\rangle - \mathbf{T}\left[\mathbf{X}',t\right]\left\langle\mathbf{X}-\mathbf{X}'\right\rangle\right\}dV_{\mathbf{X}'}\ . \tag{193}$$

By following the procedure shown in section 2.1, equation (190) can be rewritten as

$$\begin{aligned}&\left\{\int_{t_{n-1}}^{t_n}\dot{\mathbf{N}}_t^T\ddot{\mathbf{N}}_t dt+\dot{\mathbf{N}}_t^T\left(t_{n-1}^+\right)\dot{\mathbf{N}}_t\left(t_{n-1}^+\right)\right\}\otimes\left(\int_\Omega \rho d\Omega\right)\cdot\mathbf{d}_n\\&+\int_Q\dot{\mathbf{N}}_t^T\otimes\left(-\mathbf{f}_{int}\right)dQ+\mathbf{N}_t^T\left(t_{n-1}^+\right)\otimes\left\{-\mathbf{f}_j^{int}\left(t_{n-1}^+\right)\right\}\\&=\int_Q\dot{\mathbf{N}}_t^T\otimes\mathbf{b}dQ+\dot{\mathbf{N}}_t^T\left(t_{n-1}^+\right)\dot{\mathbf{N}}_t\left(t_{n-1}^-\right)\cdot\mathbf{d}_{n-1}+\mathbf{N}_t^T\left(t_{n-1}^+\right)\otimes\left\{-\mathbf{f}_j^{int}\left(t_{n-1}^-\right)\right\}\end{aligned}, \qquad (194)$$

where $\mathbf{N}_t$ is the quadratic temporal shape function (equation (22)). $\mathbf{d}_n$ and $\mathbf{d}_{n-1}$ are the displacement vector of current and previous time step. The displacement vector includes the particle displacement data at all temporal nodes.

Generally, $\mathbf{d}_n$ can be solved by setting the residual vector and using Newton's method similar to the procedure shown in section 2.4. In the case of linear elasticity, we obtain the linear system in the form of $\mathscr{K}\mathbf{d}_n=\mathscr{F}$, similar to space-time FEM shown in section 2.2. In the case of coupling TDG formulation and non-ordinary state-based peridynamics case, the system matrix $\mathscr{K}$ is given as

$$\mathscr{K}=\begin{bmatrix}\frac{5\mathbf{M}_{PD}}{\Delta t^2}+\frac{\mathbf{K}_{PD}}{2} & -\frac{4\mathbf{M}_{PD}}{\Delta t^2}-\frac{2\mathbf{K}_{PD}}{3} & -\frac{\mathbf{M}_{PD}}{\Delta t^2}+\frac{\mathbf{K}_{PD}}{6}\\ -\frac{12\mathbf{M}_{PD}}{\Delta t^2}+\frac{2\mathbf{K}_{PD}}{3} & \frac{16\mathbf{M}_{PD}}{\Delta t^2} & -\frac{4\mathbf{M}_{PD}}{\Delta t^2}-\frac{2\mathbf{K}_{PD}}{3}\\ \frac{7\mathbf{M}_{PD}}{\Delta t^2}-\frac{\mathbf{K}_{PD}}{6} & -\frac{12\mathbf{M}_{PD}}{\Delta t^2}+\frac{2\mathbf{K}_{PD}}{3} & \frac{5\mathbf{M}_{PD}}{\Delta t^2}+\frac{\mathbf{K}_{PD}}{2}\end{bmatrix}. \qquad (195)$$

This is the same form as equation (31), however, the mass and stiffness matrix in non-ordinary state-based peridynamics is different from those of the finite element method. For example, in 1D case, the mass matrix $\mathbf{M}_{PD}$ is given as

$$\mathbf{M}_{PD} = \int_{\Omega} \rho d\Omega = \rho \begin{bmatrix} V_1 & & & & \\ & V_2 & & O & \\ & & \ddots & & \\ & O & & \ddots & \\ & & & & V_N \end{bmatrix}, \tag{196}$$

where N is number of particles and V_i is the volume associated with the i-th particle. In general, the form of the stiffness matrix $\mathbf{K}_{PD}$ is complicated due to the effects of the particle spacing, horizon size and influence function. A particular form of $\mathbf{K}_{PD}$ of the 1D spatial case is derived by assuming that the particles are evenly spaced, the influence function is constant of value of one and the horizon size is one particle distance. First, from equation (182),

$$\bar{K}(X_i) = \begin{cases} \Delta X^2 \cdot \Delta V & \text{if } i = 1 \text{ or } N \\ 2\Delta X^2 \cdot \Delta V & \text{otherwise} \end{cases}, \tag{197}$$

where ΔX and ΔV are the distance of neighbor particles and volume of a particle. Note that the number of family of a particle is two or less since the horizon size is one particle spacing. Then, from equation (180) we have

$$\underline{T}[X_i]\langle X_{i-1} - X_i \rangle = \frac{E \cdot (u_{i-1} - u_i)}{\bar{K}_i}, \tag{198}$$

$$\underline{T}[X_i]\langle X_{i+1} - X_i \rangle = \frac{E \cdot (u_{i+1} - u_i)}{\bar{K}_i}, \tag{199}$$

where E is the Young's modulus and u_i is the displacement of i-th particle. Then, the approximation of the integration of the force state is given as

$$\int_{H_X} \underline{T}[X] - \underline{T}[X']dV \approx \begin{cases} \dfrac{2E \cdot (u_2 - u_1)}{\Delta X^2} & \text{if } i = 1 \\ \dfrac{2E \cdot (u_{N-1} - u_N)}{\Delta X^2} & \text{if } i = N \\ \dfrac{E \cdot (u_{i+1} - 2u_i + u_{i-1})}{\Delta X^2} & \text{otherwise} \end{cases} . \tag{200}$$

Finally, the stiffness matrix is given as

$$\mathbf{K}_{PD} = \int_\Omega (-f_{int}) d\Omega = \frac{E \cdot \Delta V}{\Delta X^2} \begin{bmatrix} -2 & 2 & & & & & \\ 1 & -2 & 1 & & & O & \\ & 1 & -2 & 1 & & & \\ & & \ddots & \ddots & \ddots & & \\ & & & 1 & -2 & 1 & \\ & O & & & 1 & -2 & 1 \\ & & & & & 2 & -2 \end{bmatrix} . \tag{201}$$

For other conditions, $\mathbf{K}_{PD}$ can be numerically evaluated by a similar procedure.

CHAPTER 6

RESULTS AND DISCUSSIONS

6.1 Nonlinear space-time FEM with hyperelastic constitutive model

6.1.1 Plate subjected to uniaxial cyclic tension

To verify the proposed nonlinear space-time FEM framework, we first consider the problem of a thin rectangular plate subjected to uniaxial tension with hyperelastic constitutive model. Spatial domain of the problem is modelled with Q4 elements and plane stress condition is assumed. The dimension, boundary conditions, and spatial mesh of the model are shown in Figure 11. As described earlier, three nodes are assigned along the temporal axis for each space-time slab and a quadratic function is used as the temporal shape function for the space-time FEM. The material is assumed to be isotropic hyperelastic and modelled with the modified Mooney-Rivlin constitutive model (106). The material parameters are given as $C_{10} = 1.0\,[\text{MPa}]$, $C_{01} = 0.5\,[\text{MPa}]$ and $k = 5.0 \times 10^{2}\,[\text{MPa}]$ and mass density is $\rho = 930\,[\text{kg/m}^3]$. For verification and comparison purposes, the same problem is also solved using the commercial FEM code ABAQUS employing both explicit and implicit time integration algorithms. For explicit time integration, standard center difference scheme is employed and Newmark time integration algorithm ($\beta = 0.28$, $\gamma = 0.55$) is chosen for the implicit time integration.

In terms of the loading condition, a pressure $p(t) = 2.0 \times (1 - \cos 2\pi ft)\,[\text{MPa}]$ is applied on the top of the plate, where $f = 1/T = 10\,[\text{Hz}]$ is the frequency of the cyclic loading and T is the period. The time step for the explicit method is determined by the Courant-Friedrichs-Lewy (CFL) condition [64] and $dt = 3.0 \times 10^{-6}\,[\text{s}]$ is used. For the implicit method, different time step sizes of Δt were tried and it is found that maximum allowable time increment in ABAQUS is $dt = 1.0\times10^{-2}$ [s]. On the other hand, for nonlinear space-time FEM, time steps of $dt = T/4, T/8, T/16 = 2.5\times10^{-2}, 1.25\times10^{-2}, 6.25\times10^{-3}$ [s] are examined.

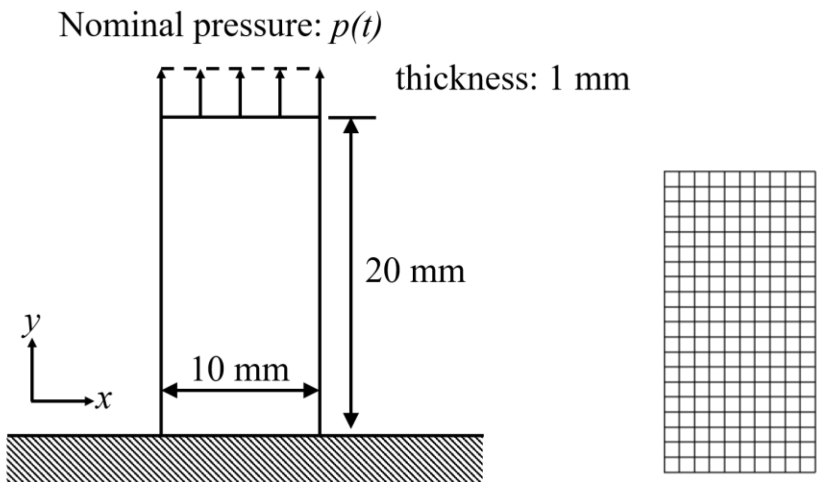

Figure 11. 2D FEM model and dimension for rubber plate under cyclic pressure.

Figure 12 shows a comparison of displacement solutions at the top edge of the plate obtained from three different approaches. It can be seen that the results from $dt = T/8, T/16$ in space-time FEM show good agreement with the predictions obtained from regular FEM. These time increments are at least three orders of magnitude larger than that of FEM explicit integration. The largest time increment tried in space-time FEM is $dt = T/4$ and discrepancies are observed for the peak displacement in this case, which is an indication that the temporal mesh is too coarse to capture the responses. The temporal resolution can be further improved by either *p*- or *h*-type of adaptive refinement in the temporal domain. The implementation is relatively straightforward due to the multiplicative form of the shape functions that are introduced.

It is also observed that FEM implicit method can solve the problem with larger time increment. However, the information between the time steps are lost due to the finite difference nature of the time integration. In contrast, information at any time point can be obtained based on interpolation using the temporal shape functions in space-time FEM. This capability is critical in handling time or history dependent constitutive models such as viscoelasticity, plasticity or damage models and often leads to a local-global coupling scheme. In this type of coupling scheme, constitutive models are resolved based on the interpolation from the space-time shape function at discrete temporal quadrature points to ensure that material responses are accurately accounted for.

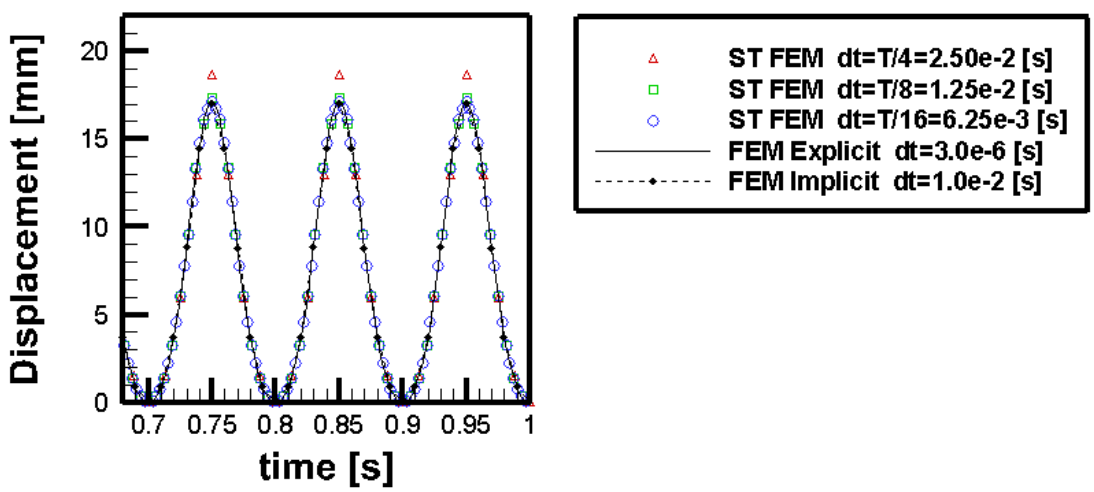

Figure 12. Displacement histories of the top side of the plate with cyclic loading by regular FEM implemented on ABAQUS (explicit and implicit) and nonlinear space-time FEM with different time steps.

6.1.2 Shear and bending deformation of the bar

To demonstrate the accuracy of more complex deformation patterns, other example problems are solved in this and next section. The problem shown in Figure 13 is considered to check the capability of nonlinear space-time FEM to express the shear, bending and rotational deformation. The time dependent shear stress $\tau = 0.1t\,[\mathrm{MPa}]$ is applied on the top surface of the bar. The material model is same as that of the previous one. Figure 14 shows the deformation results by the regular FEM (ABAQUS) and nonlinear space-time FEM. Since the both results show good agreement, it is found that the nonlinear space-time FEM can capture the complex deformation from the combination of shear and bending.

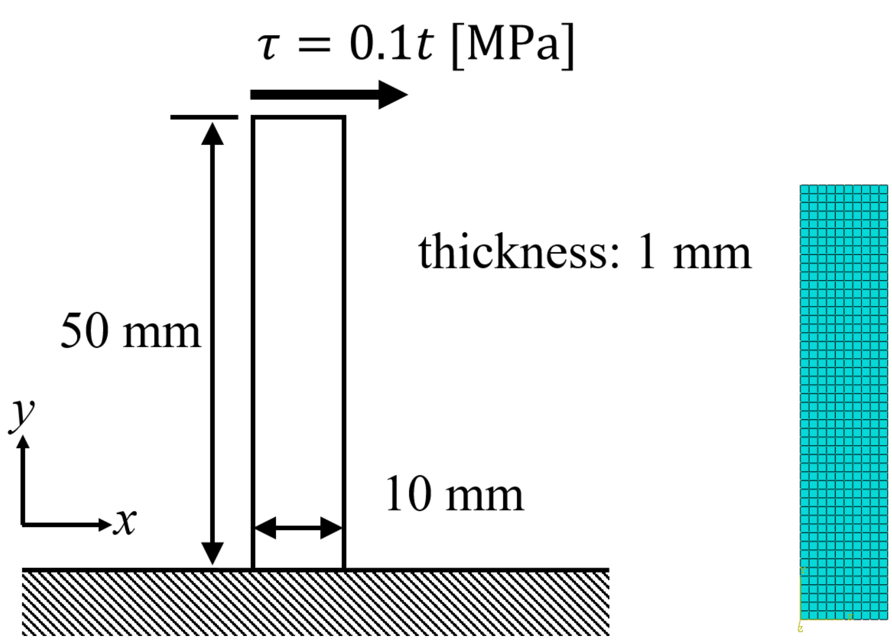

Figure 13. 2D bar FEM model (500 elements, 561 nodes) and its dimension.

6.1.3 Buckling deformation of the arch bar

Next, the buckling deformation is checked by using the arch model shown in Figure 15. An arch like model in [72] is used for reference. The both ends of arch bar are pinned and

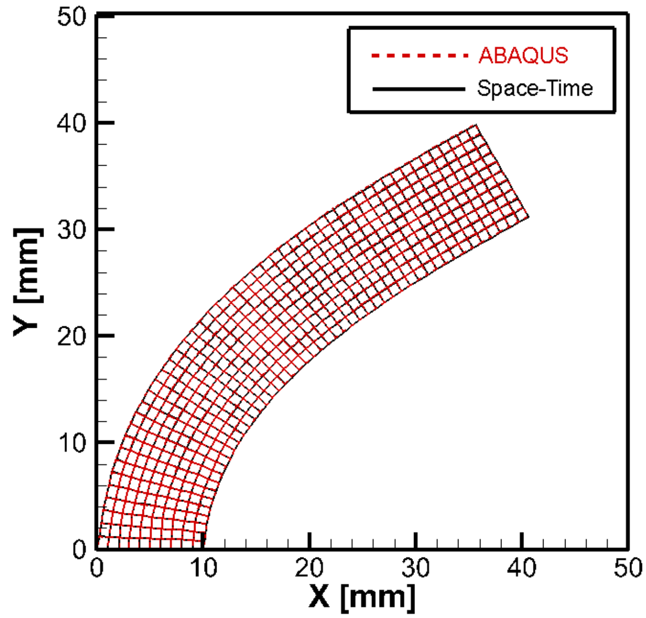

Figure 14. 2D bar with shear stress (deformation at $t = 1.0\,[\mathrm{s}]$).

indentation displacement $U_y = -1.0\left[\mathrm{mm/s}\right]$ is prescribed on the top. Hyperelasticity with the modified Mooney-Rivlin constitutive model (106) is assumed as the material. The material parameter is given as $C_{10} = 1000\,[\mathrm{MPa}]$, $C_{01} = -700\,[\mathrm{MPa}]$ and $k = 5.0\times 10^2\,[\mathrm{MPa}]$. Also, the mass density is $\rho = 1.21\,[\mathrm{g/cm^3}]$. Figure 16 demonstrates the buckling deformation results from nonlinear space-time FEM. Figure 17 shows the equilibrium paths of the displacement and reaction force at the top point. It is found that nonlinear space-time FEM and regular FEM show good agreement. The region between local maximum and minimum force is the unstable solution and it cannot be obtained by load control scheme because of snap through buckling behavior. From these results, it can be said that nonlinear space-time FEM is able to capture the buckling deformation.

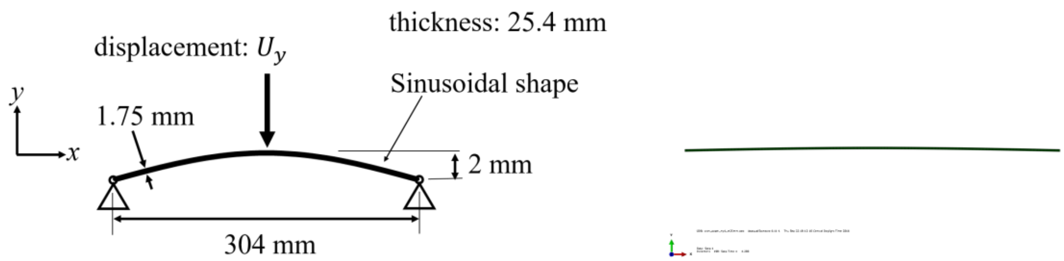

Figure 15. 2D arch model (2000 elements, 2505 nodes) for buckling deformation.

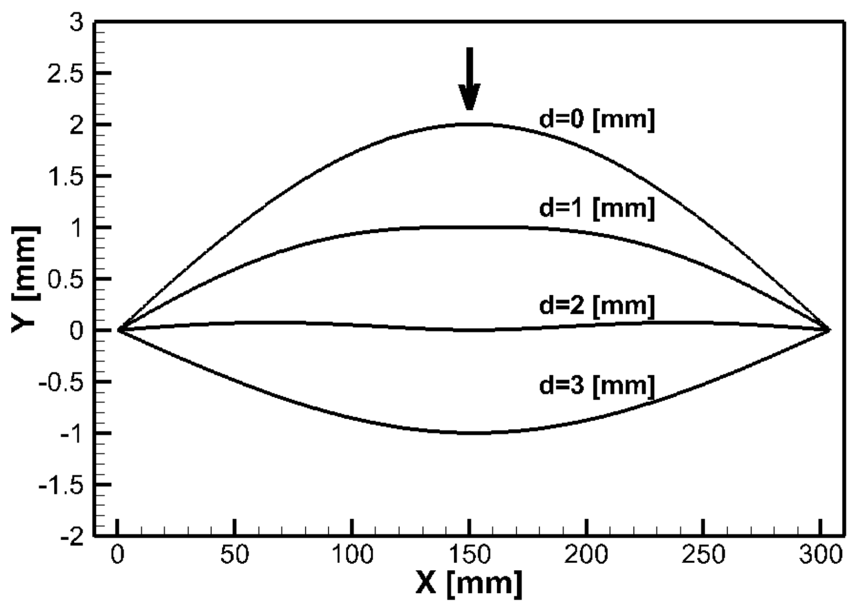

Figure 16. Buckling deformation of the ache bar from the nonlinear space-time FEM (Only the center line of the bar is visualized).

6.1.4 Transverse beam problem in the nonlinear space-time FEM

To demonstrate the robustness of nonlinear space-time FEM in handling more complicated loading condition, we consider the case of a beam with a span of $10[\mathrm{m}]$ subjected to transversal pressure as shown in Figure 18. Both sides of the beam are fully clamped and the pressure load is given as $p(t) = -0.128\sin(2\pi ft)[\mathrm{MPa}]$ in which "-" indicates downwards

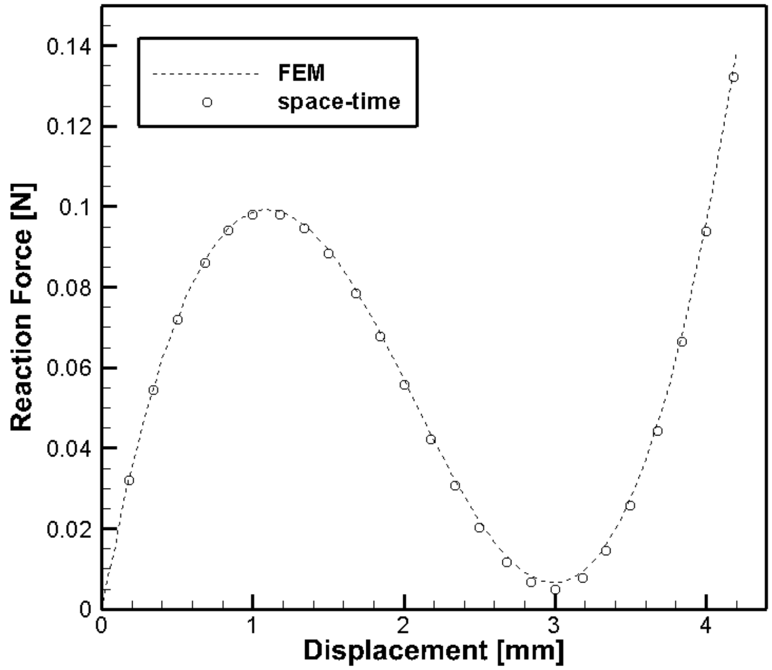

Figure 17. The equiliburium path of the displacement and reaction force at the top of the arch.

direction and f is the load frequency.

The FEM model consists from 256 Q4 elements (Evenly spaced 64 elements in length and 4 elements in width direction) in spatial domain. Modified Mooney-Rivlin constitutive model (equation (106)) is used and the material parameters are given as $C_{10} = 100[\text{MPa}]$, $C_{01} = 50\,[\text{MPa}]$ and $k = 1.0\times10^4\,[\text{MPa}]$. The mass density is $\rho = 930\,[\text{kg/m}^3]$.

Figure 19 provides a comparison on the mid-span vertical displacement history between nonlinear space-time FEM and regular FEM for the case of load frequency $f = 1.0[\text{Hz}]$. It can be first observed that the displacement is a nonlinear function of time due to the inherent coupling of the nonlinear material model with finite deformation. The good agreement between nonlinear space-time FEM ($dt = 10^{-2}\,[\text{s}]$) and explicit FEM with very refined time step of $dt = 10^{-6}\,[\text{s}]$

indicates that space-time FEM fully captures the nonlinear dynamics. On the other hand, two time step sizes ($dt = 10^{-2}$ [s] and 10^{-3} [s]) are tried in FEM with implicit method. It is observed that prediction from the case of $dt = 10^{-2}$ [s] is inaccurate by comparing with the same from space-time FEM, explicit time integration and implicit time integration using time step of 10^{-3} [s]. This example again demonstrates the robustness of the nonlinear space-time FEM approach in capturing nonlinear time-dependent deformation.

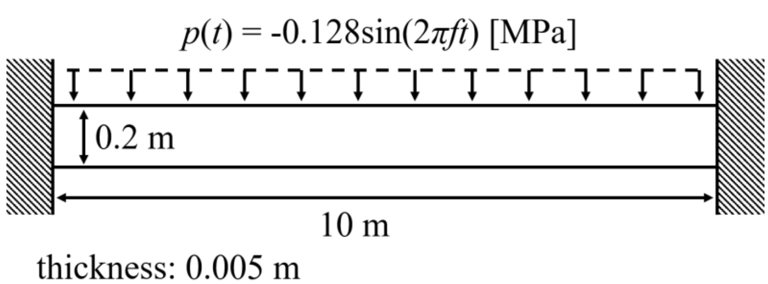

Figure 18. 2D transverse beam with cyclic loading.

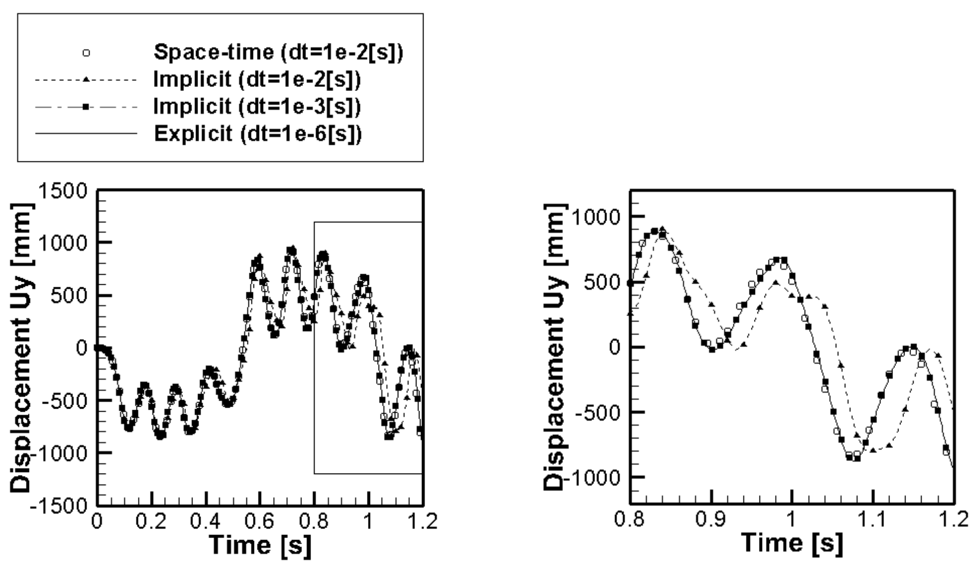

Figure 19. Comparison of displacement histories of nonlinear space-time FEM and regular FEM (Explicit and Implicit) ($f = 1.0$ [Hz]).

6.1.5 Numerical performance of nonlinear XTFEM

In this subsection, the capability of XTFEM is demonstrated. FEM model and material parameters used here are the same as in subsection 6.1.1. First, we consider the case of cyclic pressure $p(t) = 2.0 \times (1 - \cos 2\pi t)$ [MPa] applied to the top side of the plate in Figure 11. To capture the deformation that comes from material nonlinearity, we employed the following enrichment function

$$\Psi_i^m(t) = \cos(2\pi m t) - \cos(2\pi m t_i) \tag{202}$$

where $m = 1, 2, 3, 4$ are used as the temporal enrichment function in the XTFEM formulation. Figure 20 shows the results of XTFEM with hyperelastic constitutive model and regular FEM (ABAQUS, implicit). The XTFEM and regular FEM shows good agreement. This indicates that XTFEM can take very large time increment $dt = 100.0$ [s] and still provide accurate result. This is in contrast with the time increment of the order of 10^{-6} [s] or less in the FEM explicit time integration algorithm. It is very hard for explicit computation to get accurate results because of the error accumulation and the solution diverges as a result.

Next, the case of the cyclic loading with multiple frequencies are considered. The pressure $p(t) = 2.0 \times (1 - 0.6\cos 2\pi t - 0.4\cos 4\pi t)$ is prescribed to the top of the plate in Figure 11. The results are shown in Figure 21. It can be seen that nonlinear XTFEM can capture the large deformation from complicated cyclic loading with very large time increment. From these results, the nonlinear XTFEM demonstrates the capability in simulating response of hyperelastic materials subjected to cyclic loading condition.

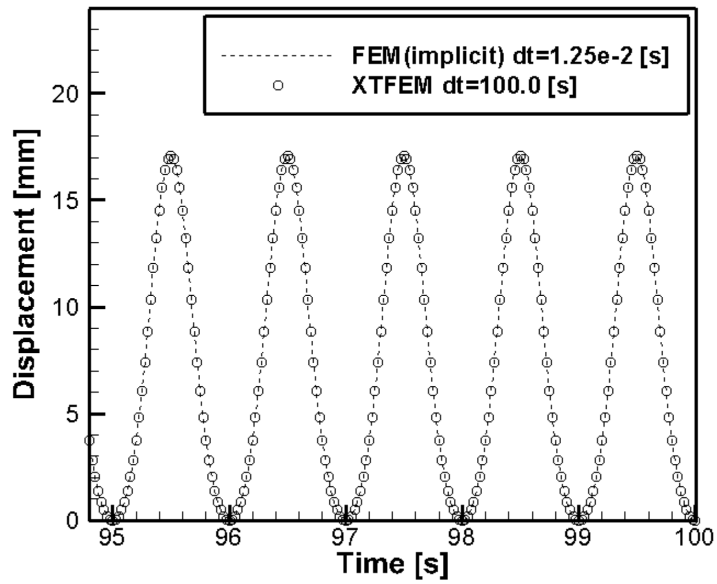

Figure 20. Displacement histories of the top side of the plate with cyclic loading by regular FEM (ABAQUS, implicit) and nonlinear XTFEM.

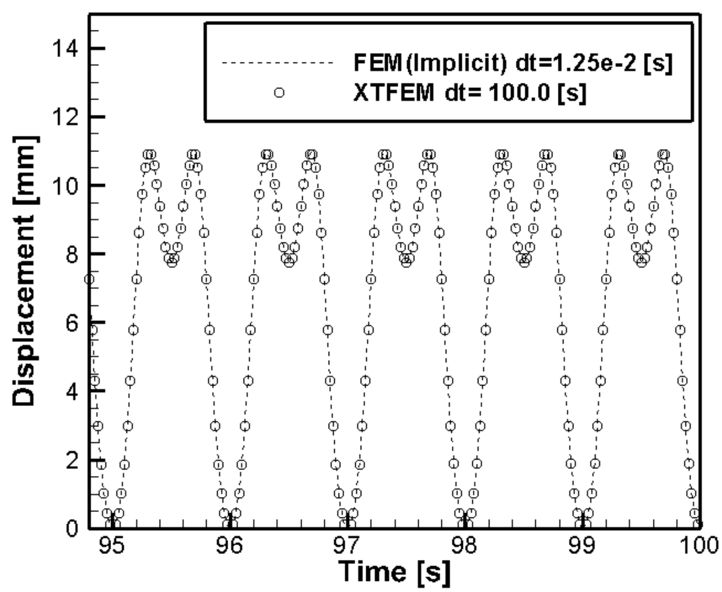

Figure 21. Displacement histories of the top side of the plate with cyclic loading of double frequencies by regular FEM (ABAQUS, implicit) and nonlinear XTFEM

6.2 Nonlinear space-time FEM with finite strain viscoelastic constitutive model

In this section, the results of nonlinear viscoelastic space-time FEM are shown and discussed. The result is verified by comparing with ABAQUS [22], one of the most widely used FEM commercial software.

For the strain energy potential, the modified Mooney-Rivlin model (equation (106)) is used for W_0 in equation (112). The material parameters are chosen as $C_{10} = 1.0\left[\mathrm{MPa}\right]$, $C_{01} = 0.5\left[\mathrm{MPa}\right]$ and $k = 500\left[\mathrm{MPa}\right]$ for all numerical examples in this section. The number of Prony series (equation (109)) is one, so that

$$\gamma\left(t\right) = \gamma_\infty + \gamma_1 \exp\left(-\frac{t}{\tau_1}\right). \tag{203}$$

6.2.1 2D plate subjected to uniaxial loading

To verify the results, the simple thin plate model is used. The plate is a square with 50 mm edges. The thickness is 1 mm and 2D plane stress condition is assumed. In spatial domain, the standard Q4 element is used and the model has 25 nodes and 16 elements. The bottom edge is fixed in vertical direction and the left edge is fixed in horizontal direction. Figure 22 shows the image of the mesh structure and boundary condition. In the temporal domain, quadratic temporal shape function (equation (22)) is used.

At first, the constant strain rates 10, 1.0 and $0.1\left[1/\mathrm{s}\right]$ are applied on the top edge. For the Prony series parameters, $\gamma_\infty = \gamma_1 = 0.5$ and $\tau_1 = 1.0\left[\mathrm{s}\right]$ are used. To verify the nonlinear space-time FEM result, it is compared with the explicit regular FEM by using the commercial FEM software ABAQUS. Figure 23 shows the stress-strain curves with different strain rates. The case of high strain rate ($10\left[1/\mathrm{s}\right]$), the stress-strain curve is very close to that of complete hyperelastic constitutive model. On the other hand, in the case of slow strain rate ($0.1\left[1/\mathrm{s}\right]$), stress value becomes close to a half of hyperelastic case. This is reasonable because $\gamma_\infty = 0.5$ in this case. Also, by comparing with ABAQUS results with nonlinear space-time FEM, it is concluded that the predictions from the space-time FEM code are correct.

Next, an example with step strain is demonstrated. In this example, $\gamma_\infty = \gamma_1 = 0.5$ and $\tau_1 = 1.0\left[\mathrm{s}\right]$ are used as Prony series parameters. The strain history and the stress response are shown in Figure 24. From these plots, the nonlinear space-time and regular FEM also show good agreement in the stress relaxation process. Furthermore, the nonlinear space-time FEM can capture exact step strain. In contrast, the large step strain cannot be well captured by regular FEM. Instead, it has to be approximated by a ramp strain with short rise time. This example demonstrates the advantage of space-time FEM in dealing with jump.

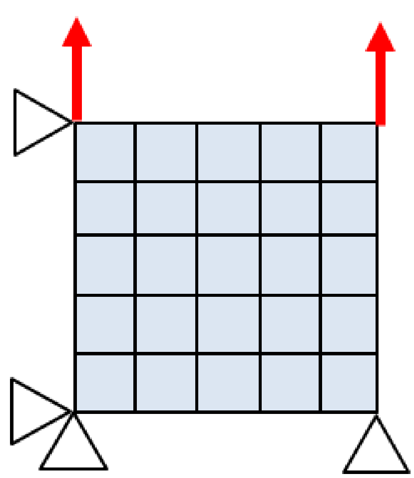

Figure 22. The FEM model and boundary conditions for the 2D plate problem.

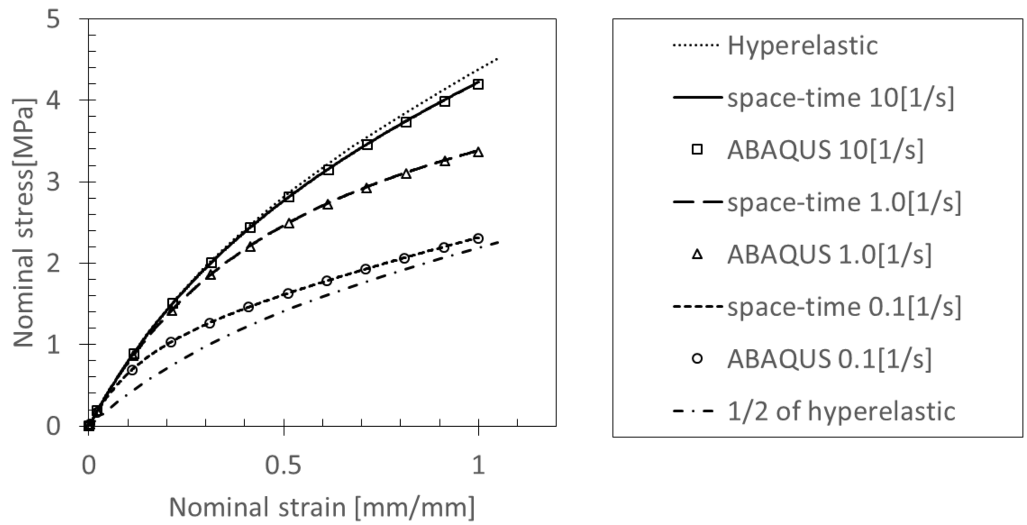

Figure 23. Comparison of stress-strain curves with different strain rates

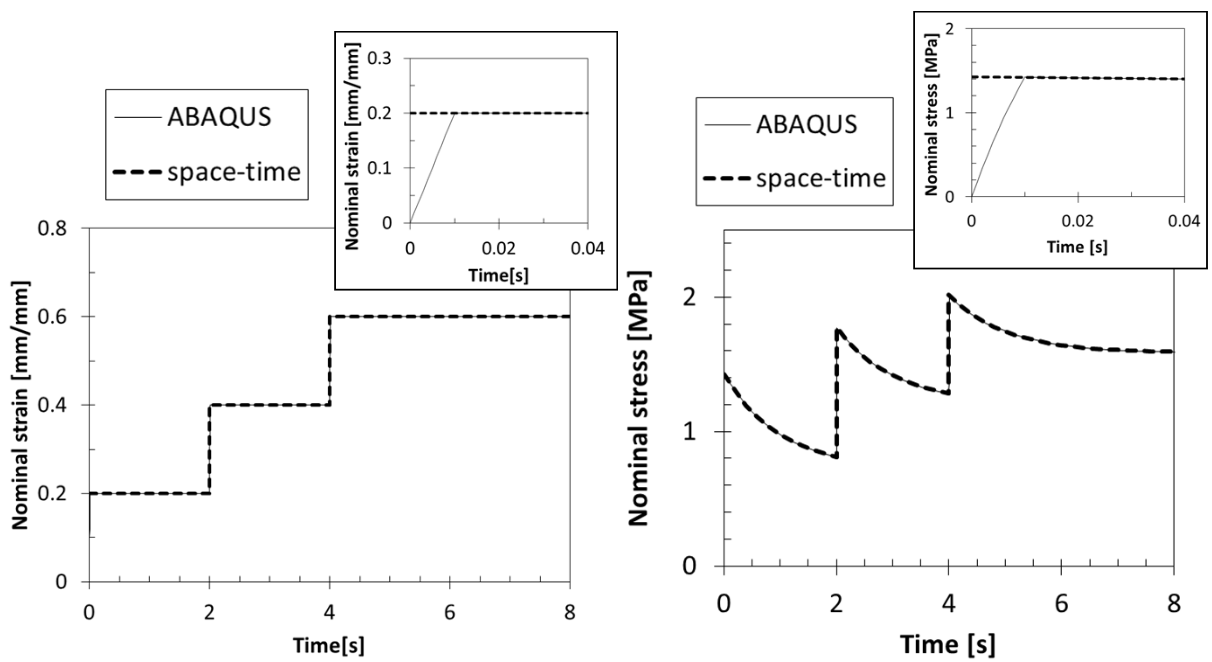

(a) (b)

Figure 24. (a) Strain history of step strain and (b) stress response(The small plots are the enlarged one at the time when the first step strain is given)

Figure 25 shows the given strain history and the stress-strain curve of the case that the sinusoidal strain history is given. In this example, $\gamma_\infty = 0.2$, $\gamma_1 = 0.8$ and $\tau_1 = 1.0\,[\mathrm{s}]$ are used as Prony series parameters. The amplitude of sinusoidal strain is $0.1\,[\mathrm{mm/mm}]$ and the frequency is $1.0\,[\mathrm{Hz}]$. In this example, five temporal time steps are used in one cycle, so that $\Delta t = 0.2\,[\mathrm{s}]$. Figure 25 shows that the nonlinear space-time FEM interpolates deformation smoothly by using temporal shape function.

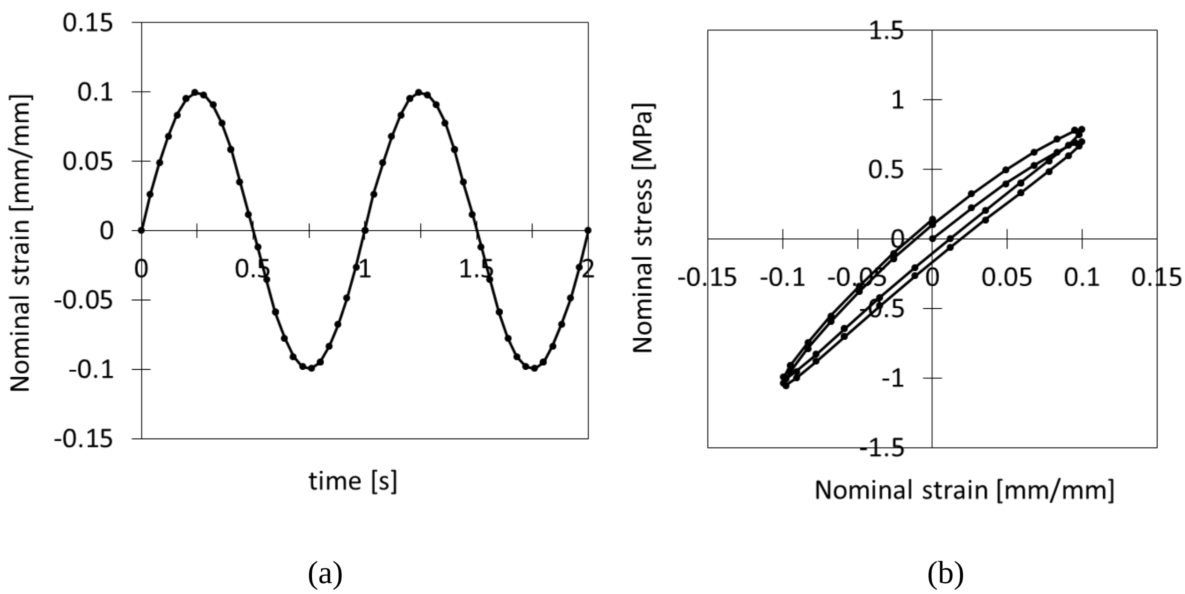

Figure 25. (a) strain history (sinusoidal strain) and (b) stress-strain plot (hysteresis curve).

6.2.2 Indentation and stress relaxation of plate

In this subsection, the indentation of a plate is considered. Figure 26 shows the mesh structure and the size and position of the indenter. In this model, the bottom edge is fixed and the symmetric condition at the plane $x = 0$ is assumed. Also, the thickness is $1.0\,[\mathrm{mm}]$ and the 2D plane stress condition is assumed. For the Prony series parameters, $\gamma_\infty = \gamma_1 = 0.5$ and $\tau_1 = 1.0\,[\mathrm{s}]$ are used. It is assumed that the indenter is rigid and the friction coefficient between the material and indenter is infinite. Figure 27 shows the compressive displacement history of the indenter.

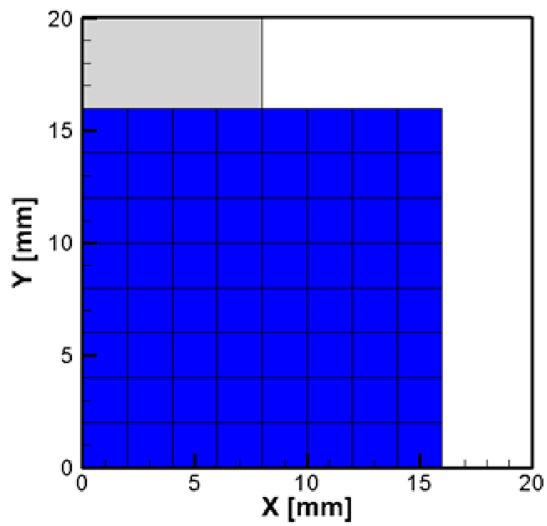

Figure 26. FEM model and indenter.

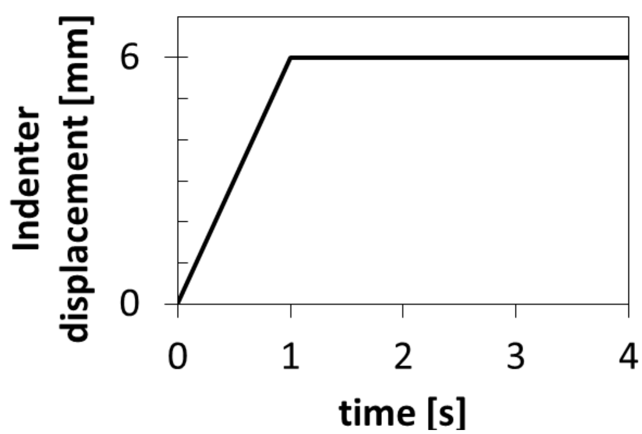

Figure 27. Compressive displacement history of the indenter.

Figure 28 demonstrates the deformation and Mises stress of the plate. It can be seen that the deformation, strain and stress responses of finite strain viscoelastic material can be well captured by using this nonlinear space-time FEM based on TDG formulation.

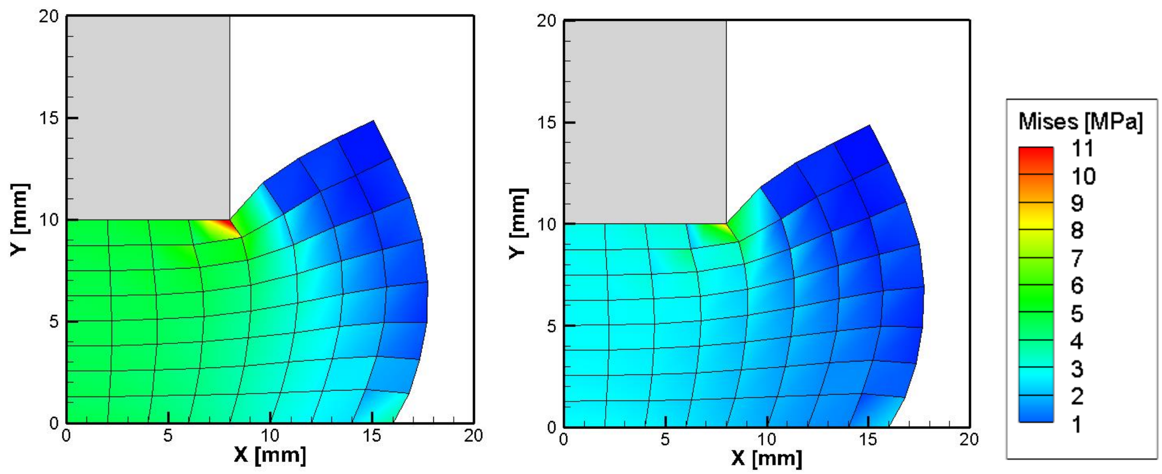

(a) $t = 1.0\left[\mathrm{s}\right]$. (b) $t = 3.0\left[\mathrm{s}\right]$.

Figure 28. Deformation and contour plot of Mises stress at different time point.

6.3 Nonlinear space-time FEM with CDM constitutive model

In this section, the predicative capability of the nonlinear space-time FEM coupled with the CDM constitutive model described in section 3.4 is demonstrated. First of all, uniaxial tests of rubber specimen are carried out to calibrate the model parameters. Simulations based on the calibrated material model are then performed for a different case of a single notch rubber specimen subjected to cyclic loads. To validate the simulation prediction, the computational results are compared with experimental results of uniaxial tension and low cycle fatigue test of rubber samples with single notch.

6.3.1 Material and experimental set up

For the experimental study, samples of carbon filled synthetic rubber has been supplied by Bridgestone Corporation, a Japanese tire company. The experiments are conducted on an Instron 5969 dual column testing system at room temperature.

6.3.2 Uniaxial tension test and calibration of CDM model parameters

The rubber specimen is designed by following ASTM D412 and the geometry is shown in Figure 29. For uniaxial loading and unloading, triangular cycle with cross-head speed of $\pm 10[\mathrm{mm/s}]$ is imposed. CDM model parameters are calibrated by comparing experimental stress-strain responses with those solved from the CDM constitutive model.

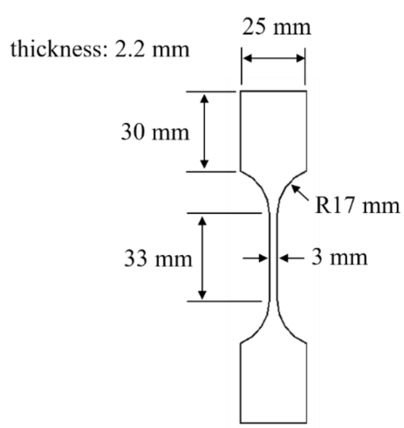

Figure 29. Geometry of rubber specimen.

The calibrated model parameters are given in Table 2. Figure 30 and Figure 31 provides the comparison between the model prediction based on the parameters and the experimental results. Figure 30 shows the stress history at the triangular cycle with strain range $0 \sim 250[\%]$.

We can see that the decline of stress peaks comes from the softening phenomena is well captured by CDM with the calibrated parameters. Figure 31 shows the nominal strain at failure and the fatigue life from experimental results and predictions from the calibrated CDM model. It can be concluded that stress softening behavior, elongation at the failure and fatigue life in relatively low cycle are consistent with CDM model predictions.

Table 2. CDM material parameters for the synthetic rubber.

C_{10} [MPa]	C_{01} [MPa]	k [MPa]	C_{20} [MPa]	C_x [MPa]	γ	σ_s [MPa]	S [MPa]	s	D_c
0.06	1.2	500	0.3	6.5	1.0	0.3	9.0	13.5	0.2

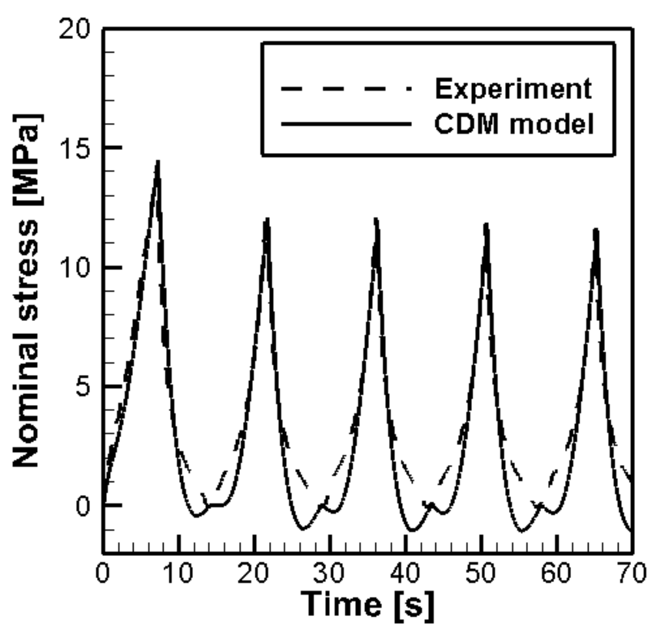

Figure 30. Calibration of CDM model for a synthetic rubber (nominal stress history).

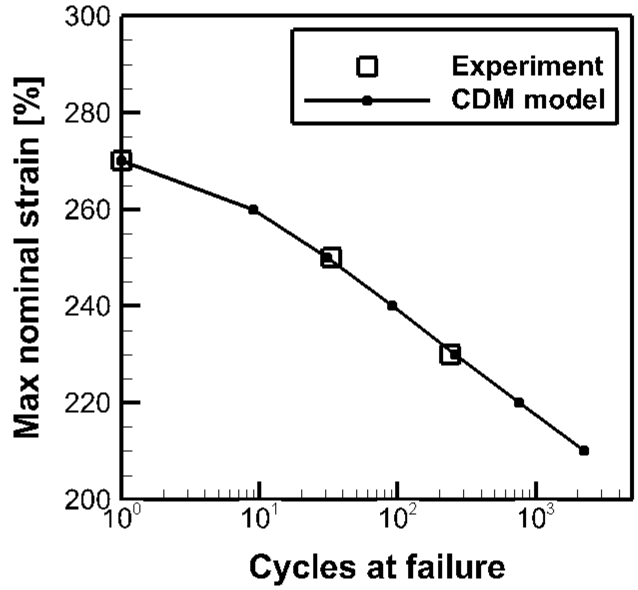

Figure 31. Calibration of CDM model for a synthetic rubber (Low cycle fatigue life [R-ratio is zero]).

6.3.3 Numerical and experimental results of the uniaxial tension tests of notched sample.

To validate the robustness of the nonlinear space-time FEM with the calibrated CDM model, computational and experimental results are presented in this section for the case of a notched specimen subjected to uniaxial tension. The rubber material is the same as that described in subsection 6.3.2 and the same set of CDM parameters have been employed in this case. The geometry of the notched specimen is shown in Figure 32 along with a representative spatial mesh. For computational implementation, a convergence study on the spatial element mesh size is first conducted. The nominal stress rate $0.68[\mathrm{MPa/s}]$ is imposed at the two ends of specimen. Figure 33 shows a relationship between maximum nominal stress at failure and the mesh size. It can be seen the stress value at failure converged to the value of $5.92[\mathrm{MPa}]$ in the case of element size of $0.35[\mathrm{mm}]$ near the notch root region. As such, we have used $0.35[\mathrm{mm}]$ mesh density at notch root region in this study. It is also noted that the computed stress value of $5.92[\text{MPa}]$ compares favorably with the experimentally measured value of $6.08[\text{MPa}]$.

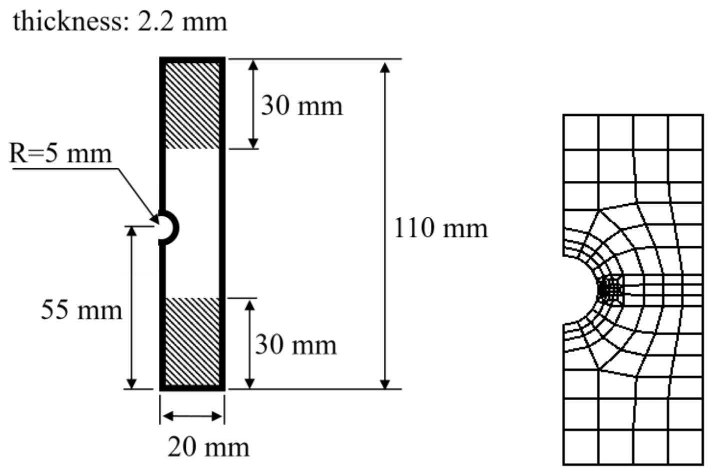

Figure 32. Geometry of the notched rubber specimen and mesh structure for FEM. (The shaded regions at the top and bottom are grabbed by jigs of testing machine.)

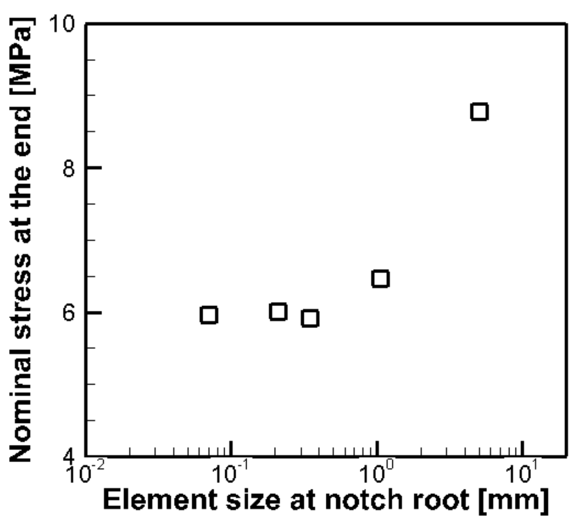

Figure 33. The relationship between the mesh size at the notch root and the nominal stress at the failure.

Next, computational predictions of fatigue failure are compared with experimental results. Triangle wave cyclic loading with constant cross-head speed $10\left[\text{mm/s}\right]$ for both loading and unloading is imposed (Figure 34 (a)). At the same time, the maximum and minimum nominal stress values at the end are controlled in the experiment (Figure 34 (b)). The value of the maximum stress is chosen to be in the range of $3.0 \sim 6.0\left[\text{MPa}\right]$ and the minimum stress is kept at $0\left[\text{MPa}\right]$. The number of cycles at failure is recorded. Figure 35 provides a comparison on the maximum nominal stress vs number of cycles to failure between the experiment and simulation. As can be seen, simulation yields good agreement with experiment for the range of the stress ratios applied. Due to the limitation of the experiment instrumentation, the maximum load cycles applied is 1244 and the corresponding predicted cycle is 1408 under the same loading condition. To further demonstrate the robustness of the simulation approach, other simulation cases of maximum applied stress of 2.73, 2.50, 2.40 and 2.23 [MPa] are carried out. To accelerate the computation of these higher cycle cases, the Jacobian matrices $\left[\dfrac{\partial \mathbf{G}}{\partial \mathbf{d}_n}\right]$ in equation (65) are stored over a cycle and reused for following cycles. Since the damage accumulation in each time step is extremely small, this recycling of Jacobian matrices can give enough convergence. Due to the relatively low stress, the number of cycles to failure is given as 21985, 104656, 236252 and 1083614.

It is thus concluded that the nonlinear space-time FEM with CDM can predict both fracture and fatigue life.

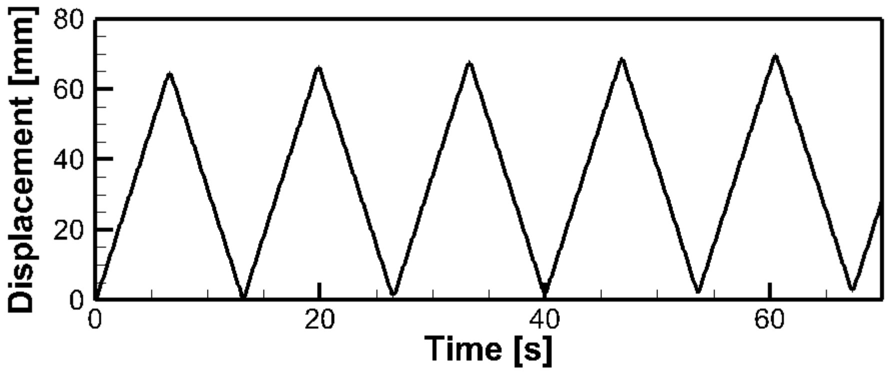

(a) Displacement history of cross-head.

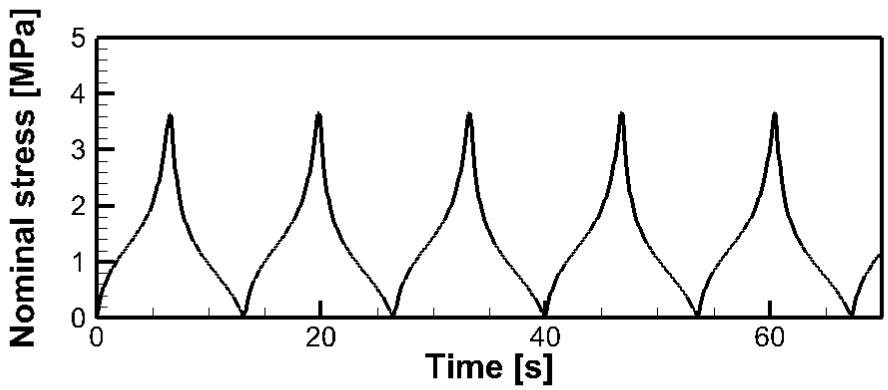

(b) Nominal stress history at the end of specimen.

Figure 34. An example of loading condition. (In (a) displacement history of the cross-head, cross-head speed at both loading and unloading are constant. In (b) stress history, maximum and minimum stress values are fixed.)

6.4 Fracture prediction based on non-ordinary state-based peridynamics

In this section, the performance of non-ordinary state-based peridynamics is demonstrated before moving to the coupled simulation of space-time FEM and peridynamics. Some examples of failure prediction of composite materials are shown in the following subsections.

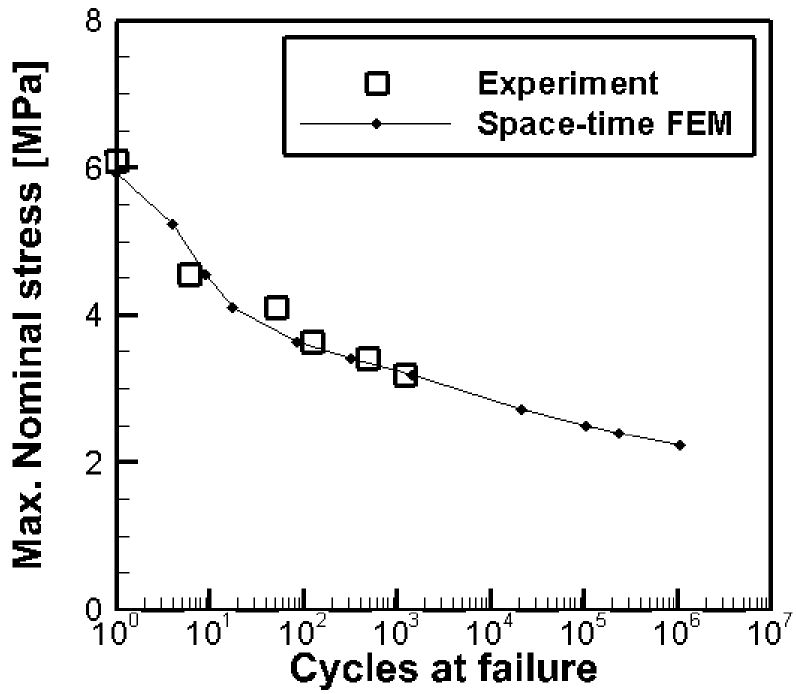

Figure 35. The comparison of experimental and computational results of low cycle fatigue of the notched specimen.

6.4.1 2D composite plate with circular inclusions

Here, failure prediction of 2D composite plate with circular inclusions is conducted. The peridynamics models of the composites are shown in Figure 36. There are four sets of number (*N*) and radius (*R*) of the inclusions, $(N, R[\text{mm}]) = (12, 6.0)$, $(24, 4.2)$, $(36, 3.5)$ and $(48, 3.0)$. Each set has three models with different random distributions of inclusions so that there are totally twelve models. The volume ratio of inclusions is constant (13.6 %) in all models.

The modified Mooney-Rivlin hyperelastic constitutive model (equation (106)) is used for the matrix part of the composites. The Mooney-Rivlin material parameters are chosen as $C_{10} = 1.0[\text{MPa}]$, $C_{01} = 0.5[\text{MPa}]$ and $k = 100[\text{MPa}]$. The mass density of the matrix is

$\rho_M = 930\left[\mathrm{kg/m^3}\right]$. On the other hand, the inclusions are assumed to be linear elastic and roughly ten times stiffer than the matrix part. For the inclusion Young's modulus $E = 88\left[\mathrm{MPa}\right]$ and the Poisson's ratio $\nu = 0.49$ are used. The mass density of the inclusion is set as $\rho_I = 9300\left[\mathrm{kg/m^3}\right]$ to keep the wave speed same as that of the matrix part in this example problem.

The shape of the composite plates is a square with the edges of 100 [mm] and the thickness is 1.0 [mm]. The peridynamics particles are equally spaced in the horizontal and vertical directions. The distance of the neighbor particles is 1.0 [mm] and total number of particles is 10000. The horizon size is defined as $\delta = 3.0\left[\mathrm{mm}\right]$. The non-ordinary state-based peridynamics is stabilized by following the procedure shown in section 4.3 and the stabilization parameter $G = 1.0$ is used. For failure prediction, the stretch at a failure of the bond is given as $\lambda_f = 1.5$. In other words, if $\left|\underline{\mathbf{Y}}\langle\boldsymbol{\xi}\rangle\right|/\left|\boldsymbol{\xi}\right| > \lambda_f$, then the bond $\boldsymbol{\xi}$ is broken.

In terms of the boundary conditions, the bottom edge of the composite plate is fixed and the uniaxial tension is given by applying the constant velocity $v = 10\left[\mathrm{mm/s}\right]$ to the top edge. For the time integration, the velocity Verlet scheme is used with the time step size of $1.0^{-6}\left[\mathrm{s}\right]$. Figure 37 shows an example of crack propagation. We observe that the crack avoids the inclusions in this example. The stress-strain curves of composite materials are plotted in Figure 38. All the paths of stress-strain curve are almost same because the volume ratio of inclusions is constant in all composite models. On the other hands, Figure 39 shows the relationship between tensile strength and radius of inclusions. The composite with smaller inclusion has higher strength. This is because the smaller inclusion composite is more uniform than the composite with larger inclusion and it is known that generally a failure happens at the weakest point in the material.

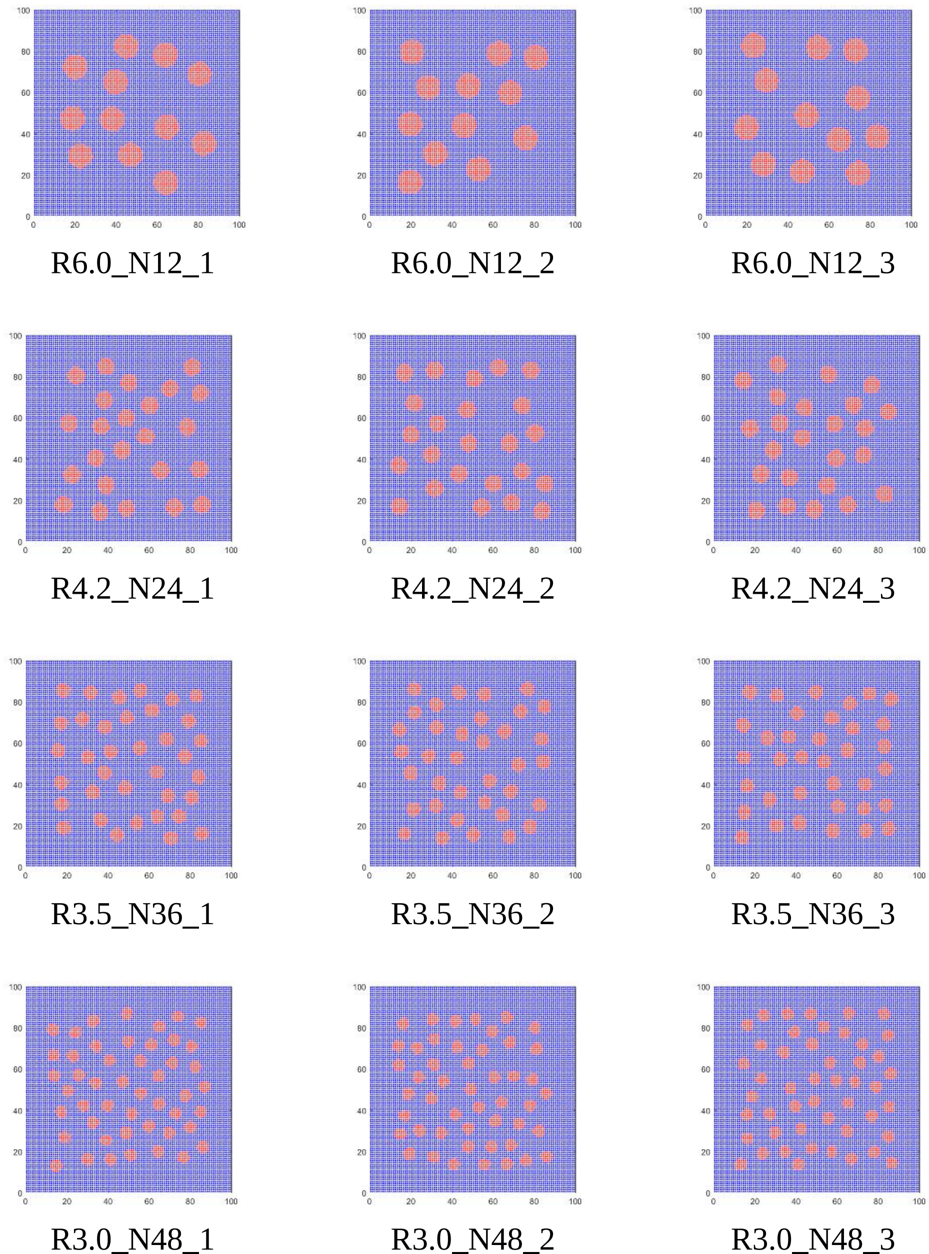

Figure 36. PD Models of 2D composite plate with circular inclusions.

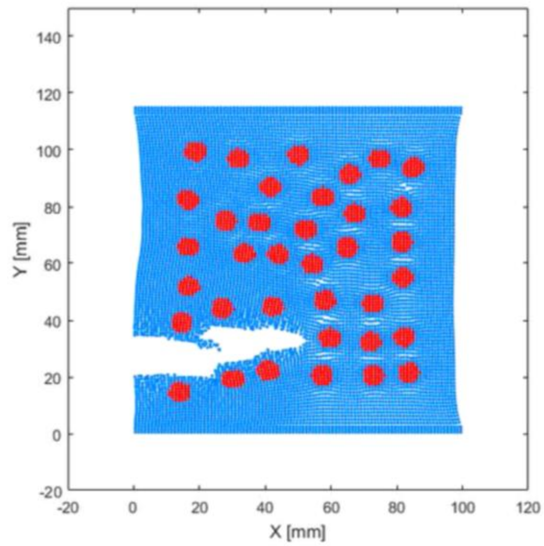

(a) Crack length 50 [mm].

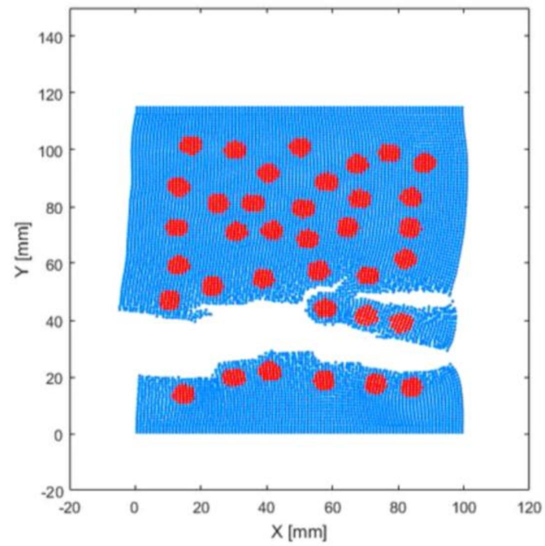

(b) Crack length 100 [mm].

Figure 37. An example of crack propagation in a composite with circular inclusions. (N36_R3.5_3).

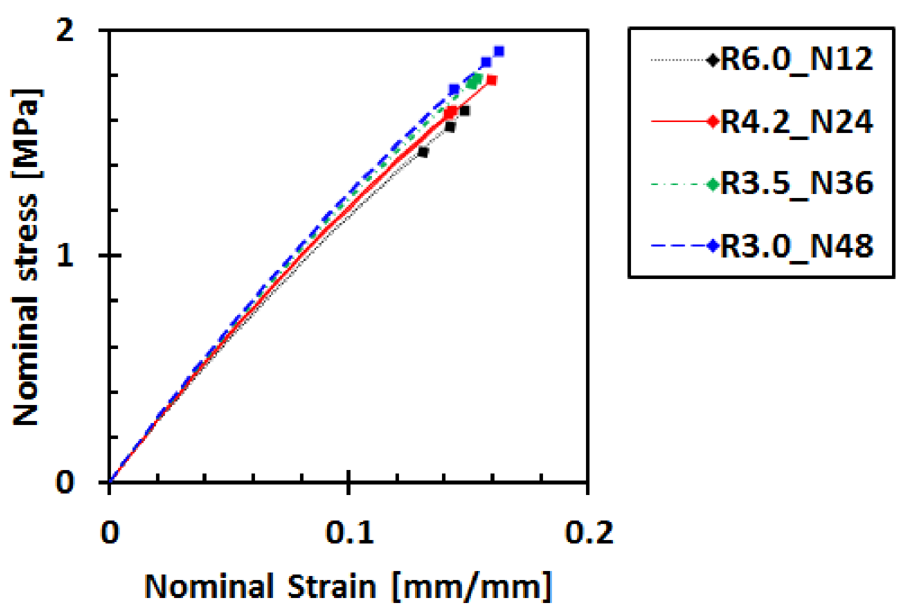

Figure 38. Stress-strain curves of composites with circular inclusions.

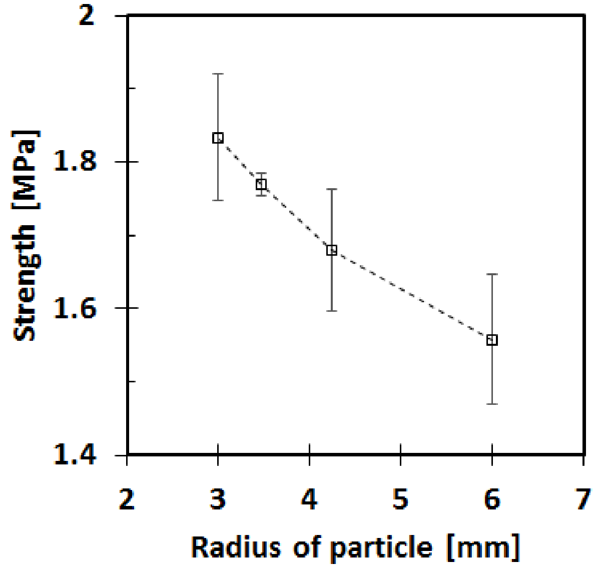

Figure 39. The relationships between tensile strength and radius of inclusions in a composite.

6.4.2 2D composite plate with fibers

The fracture simulations of the composite material with fibers are demonstrated in this subsection. The 2D plate is reinforced by eight fibers as shown in Figure 40. The materials of the matrix and fiber part are same as those of matrix and inclusions of the composite in subsection 6.4.1. The critical stretch of the bonds between particles in the matrix is defined as $\lambda_f^{MM} = 1.5$. In this example, the breakage of the bond at interface of the materials is also allowed. The simulations are conducted with two different interfacial critical stretch $\lambda_f^{MI} = 1.5$ and $\lambda_f^{MI} = 1.05$. The other parameters with regard to the model, boundary condition and computation are same as those of subsection 6.4.1.

Figure 41 shows the crack initiation and propagation of the fiber composite with strong interfacial strength. First, the crack initiates at the point between the ends of fibers. Then, the crack propagates while avoiding the fibers. The result of weak interfacial strength case is shown in Figure 42. In this case, the crack initiation happens at the end of fiber and the separation of the matrix and fibers can be observed after crack propagation.

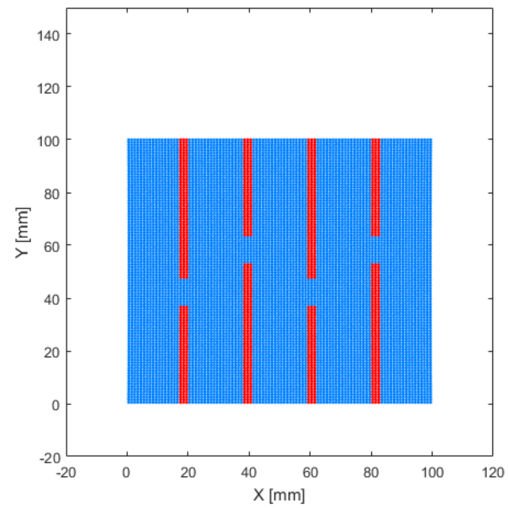

Figure 40. The PD model of 2D composite plate with fibers.

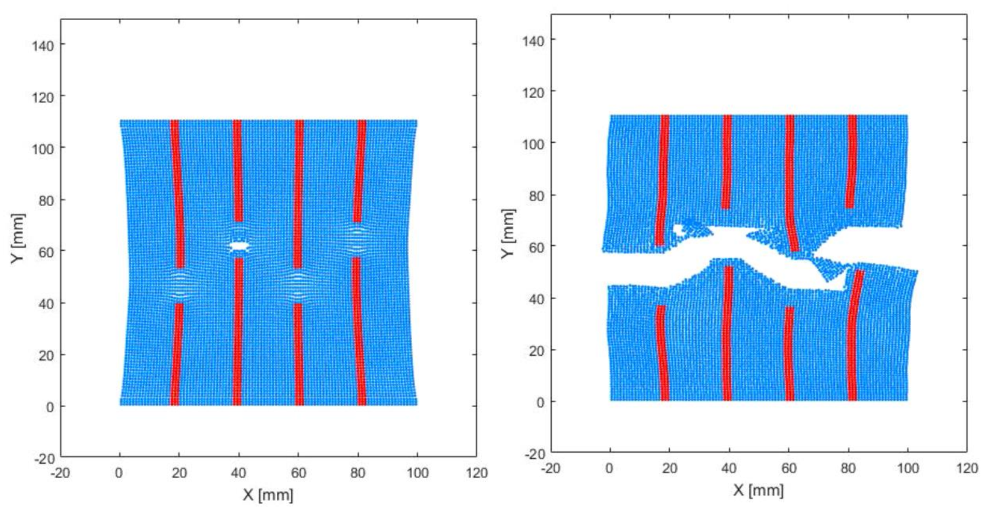

(a) Crack initiation. (b) Failure.

Figure 41. Crack initiation and propagation of the composite with fibers. (The case of strong interfacial strength $\lambda_f^{MI} = 1.5$).

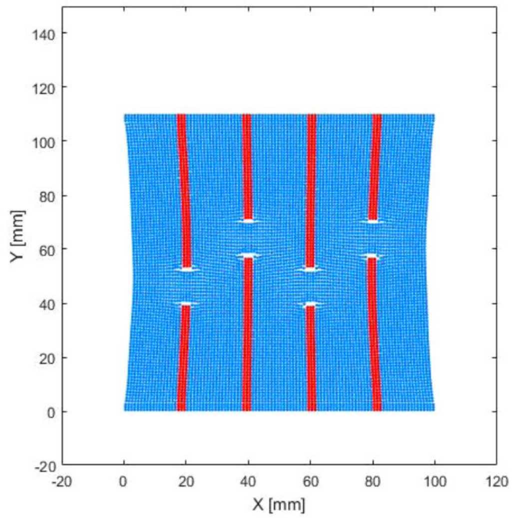

(a) Crack initiation.

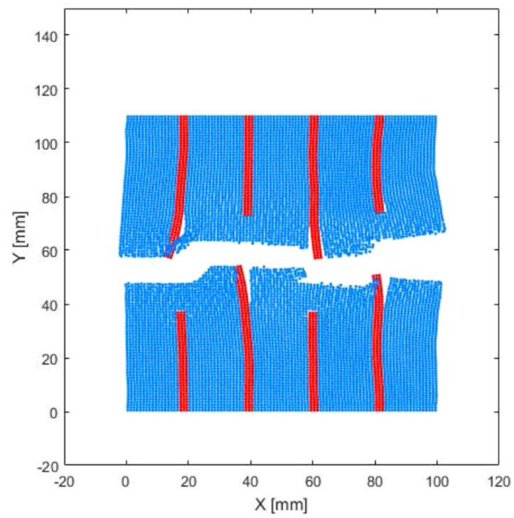

(b) Failure.

Figure 42. Crack initiation and propagation of the composite with fibers. (The case of weak interfacial strength $\lambda_f^{MI} = 1.05$).

6.5 Multiscale crack propagation simulation by coupling non-ordinary state-based peridynamics coupling with space-time FEM

6.5.1 The setup of the multiscale crack propagation simulation

In this section, numerical examples of the coupled space time/NOPD simulation are demonstrated. Crack propagation of the thin glass plate with an initial crack is considered. The space-time FEM with discontinuity enrichment is applied for whole domain to predict the deformation of the global region. Also, the NOPD region is spanned around the crack tip to simulate crack propagation. In this case, linear elastic constitutive model is assumed. For NOPD, the theory and implementation described in section 4.1 and 4.2 are applied. The space-time FEM and NOPD frameworks are combined by following coupling procedure in section 5.1.

Figure 43 shows the dimension of glass plate with an initial crack. The plate is a square with $90\left[\text{mm}\right]$ edges. It has a horizontal initial crack of $20\left[\text{mm}\right]$ at the middle of the left edge.

The thickness is set as $1[\mathrm{mm}]$ and 2D plane stress condition is assumed in the computation. The bottom edge is fixed in both horizontal and vertical direction. Several loading conditions are applied on the top edge and crack propagation is predicted for each loading condition.

For the material, the linear elastic constitutive model is assumed in which Young's modulus $E = 74[\mathrm{GPa}]$, Poisson's ratio $\nu = 0.22$, and the mass density $\rho = 2480\left[\mathrm{kg/m^3}\right]$ are chosen from typical parameters of glassy materials.

The initial configuration of coupling model of space-time FEM and peridynamics is shown in Figure 44. The global domain is discretized by a structured mesh with 81 elements and 100 nodes in space. The dashed line and triangle nodes indicate the initial crack and nodes with Heaviside step function enrichment. As a result, there are two enriched elements and six additional nodes initially. In addition, each coupled element has $12 \times 12 = 144$ PD particles, so that the particle spacing in peridynamics is $\Delta p = 5/6 \approx 0.83[\mathrm{mm}]$. The radius of horizon is $\delta = 2\Delta p$ in this case. The influence function is defined as the unity so that $\omega(|\xi|) = 1$. The stretch at the failure of the bond is defined as $\lambda_f = 1.0005$.

As explained in section 5.1, crack in the global domain is represented by enrichment shape functions in the extended space-time FEM and crack propagation is computed by peridynamics simulation, with boundary conditions obtained from the space-time FEM result. If crack passes through an FEM element, the element is enriched and peridynamics coupling domain moves along with crack tip.

In non-ordinary state-based peridynamics computation, the stabilization method shown in section 4.3 is applied. The stabilization constant in equation (186) is given as $G = 0.5$.

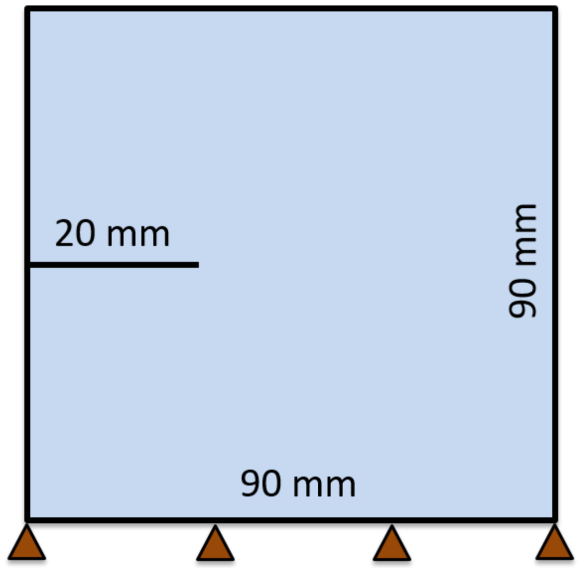

Figure 43. The dimension of thin glass plate with the initial crack at the middle. (Thickness is $1[\mathrm{mm}]$).

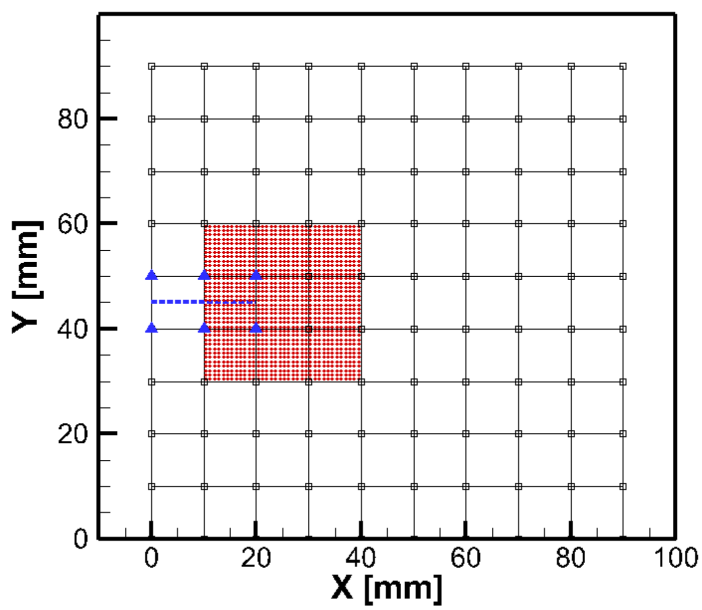

Figure 44. Initial configuration of FE mesh, peridynamics particles, crack and enriched nodes.

The time steps of space-time FEM and peridynamics is given as $\Delta t_{ST} = 1.0^{-5}\left[\mathrm{s}\right]$ and $\Delta t_{PD} = 1.0^{-9}\left[\mathrm{s}\right]$. Due to the large differences in the time step, the computational time of the space-time FEM part is quite small in the total computation and it is expected that we can drastically reduce computational cost by using this coupling method.

For verification, the result is compared with full scale NOPD simulation. Figure 45 shows the initial configuration of full scale NOPD model. There are totally $108 \times 108 = 11664$ particles. All other parameters are same as peridynamics part in the coupling code so that $\Delta p = 5/6 \approx 0.83\left[\mathrm{mm}\right]$, $\delta = 2\Delta p$, $\omega\left(\left|\xi\right|\right) = 1$, $\lambda_f = 1.0005$, $G = 0.5$ and $\Delta t = 1.0^{-9}\left[\mathrm{s}\right]$.

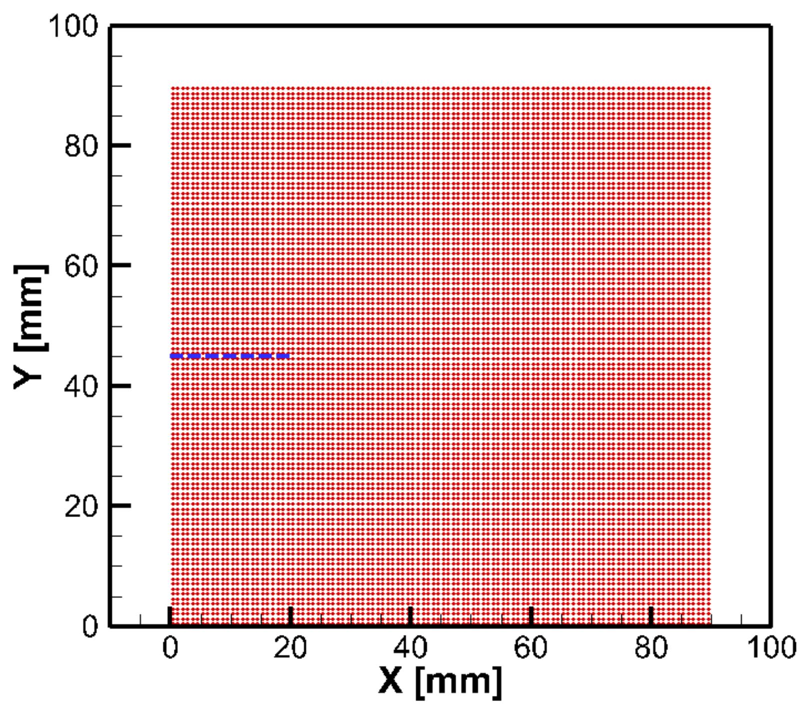

Figure 45. Initial configuration of full peridynamics model.

6.5.2 Multiscale crack propagation simulation results

The crack propagation of glass plate is simulated for two loading cases. In the first case, the constant tensile stress rate $\dot{\sigma}_y = 100\left[\mathrm{MPa/s}\right]$ is applied on the top edge of the plate shown in Figure 43. This loading condition is expected to result in a horizontally opening crack, which is known as mode I crack.

Figure 46 shows the crack propagation process of the coupling simulation. It can be seen that the peridynamics coupling region moves along the crack tip and the number of enriched nodes (denoted by triangular nodes) increases. The crack propagation process of full peridynamics simulation is shown in Figure 47. Similar to the coupling simulation, the crack propagates horizontally in full peridynamics. Figure 48 shows the comparison of the crack path between coupling simulation and full peridynamics. In mode I case, the crack path becomes horizontally and the both simulation shows good agreement.

Figure 49 illustrates the comparison of crack length history. At first, the crack length values of both simulation rise at almost same time. However, after that, the result of coupling simulation shows a little delay. In the coupling simulation, a small growth of the crack in an element does not affect the FEM part and the boundary condition for the peridynamics region because the new enrichment is done only when the crack grows over the element. On the other hand, the bond breaking immediately affects for the whole domain in full peridynamics simulation. In this case, the result may be improved by, for example, refining the mesh structure of FEM domain or using tip enrichment that can consider the singular stress field around crack tip [45]. Based on the results presented in this section, it can be concluded that the coupled simulation of space-time FEM and non-ordinary state-based peridynamics shows good agreement with the full peridynamics result in case of mode I fracture problem.

In the second case, the constant shear stress rate $\dot{\tau}_{xy} = -100\,[\mathrm{MPa/s}]$ is applied on the top edge of the plate shown in Figure 43. The displacement of the top edge is enforced to be zero in *y*-direction. This situation is referred to as crack sliding mode or mode II crack.

Figure 50 shows the crack propagating process of the coupling simulation. Because of shear loading, the crack grows in a diagonal direction. The peridynamics coupling region moves and enriched element is added along with the crack tip. The crack propagation process of full NOPD simulation is shown in Figure 51. Similar to the coupled simulation, the crack propagates diagonally in full peridynamics. Figure 52 shows the comparison of the crack path between coupled simulation and full peridynamics. In this mode II case, as we saw, the crack path becomes diagonal and the angles of the crack direction are almost the same.

Figure 53 illustrates the comparison of crack length history. In this case, the crack grows a little faster in the coupling simulation. This difference seems to be due to the same reason as discussed in the case of mode I. Similarly, it can be improved by refining the FE mesh or introducing the tip enrichment. In addition, vibrations of particles in coupled simulation have been observed in both mode I and II cases. This phenomenon comes from the stress wave reflection in the small coupling domain. Boundary condition treatments like matching boundary condition (MBC) [73, 74] and perfect matched layer (PML) [75] can be implemented to eliminate the artificial reflections.

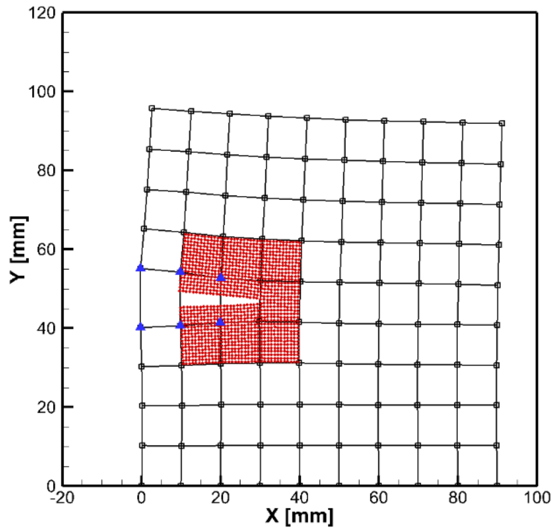

(a) $t = 0.043455\,[\mathrm{s}]$.

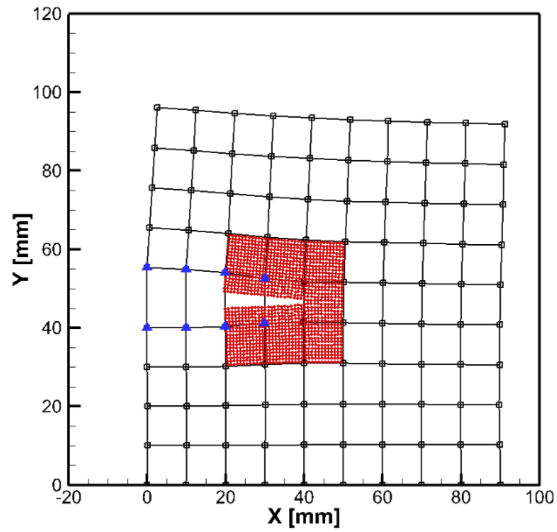

(b) $t = 0.043465\,[\mathrm{s}]$.

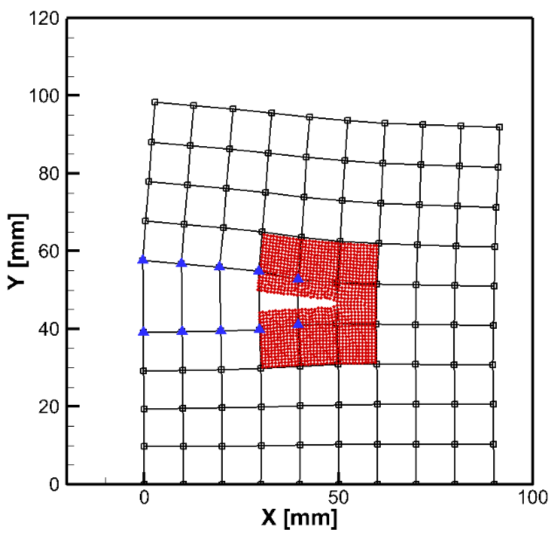

(c) $t = 0.043474\,[\mathrm{s}]$.

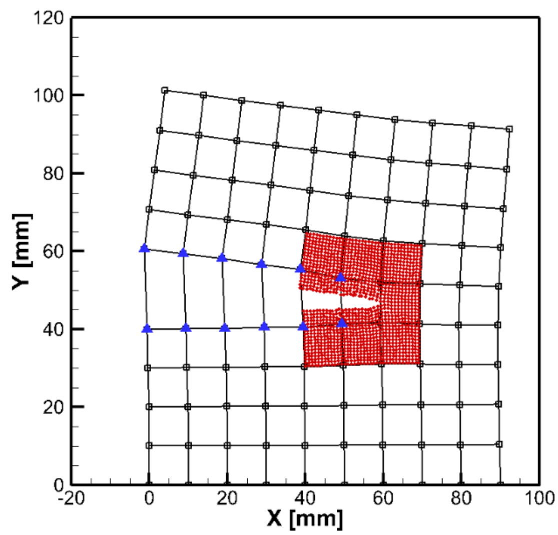

(d) $t = 0.043482\,[\mathrm{s}]$.

Figure 46. Crack propagation of coupling simulation of mode I (displacement scaling factor is 500).

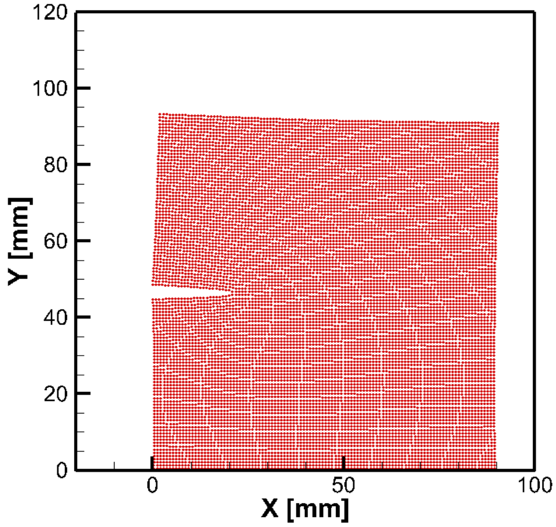

(a) $t = 0.029212\,[\mathrm{s}]$.

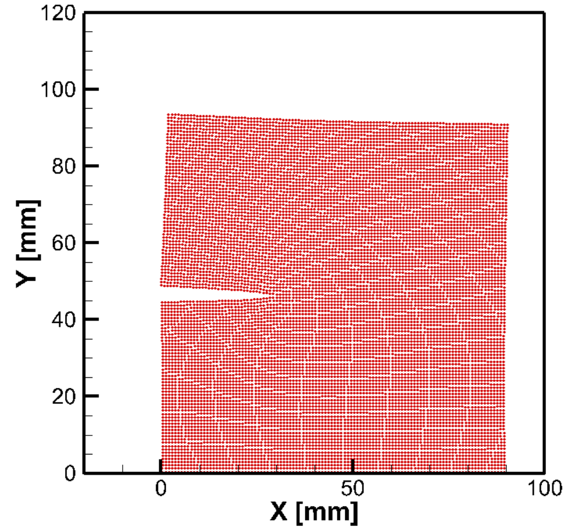

(b) $t = 0.029226\,[\mathrm{s}]$.

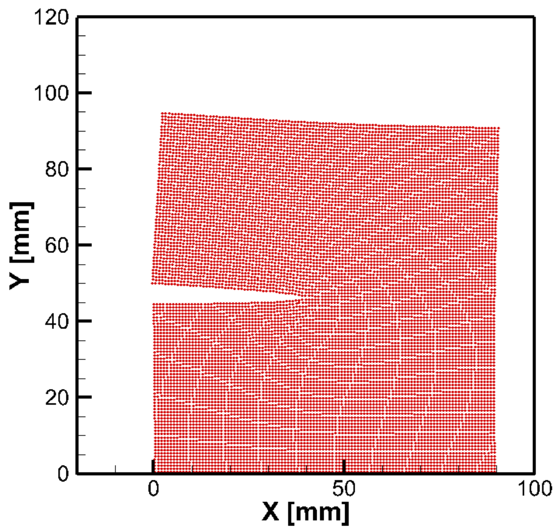

(c) $t = 0.029240\,[\mathrm{s}]$.

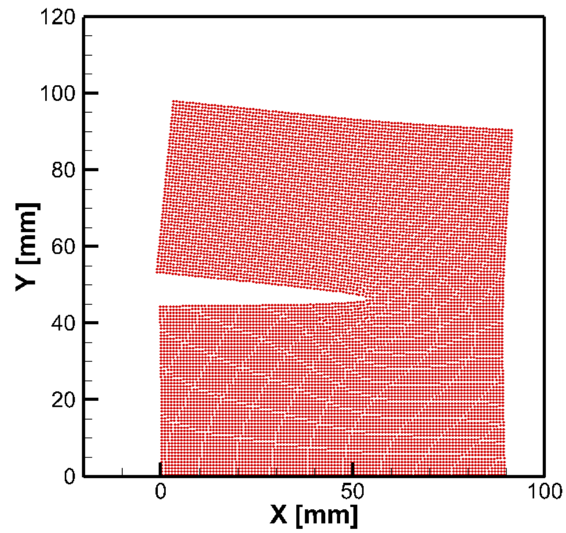

(d) $t = 0.029256\,[\mathrm{s}]$.

Figure 47. Crack propagation of full peridynamics simulation of mode I (displacement scaling factor is 500).

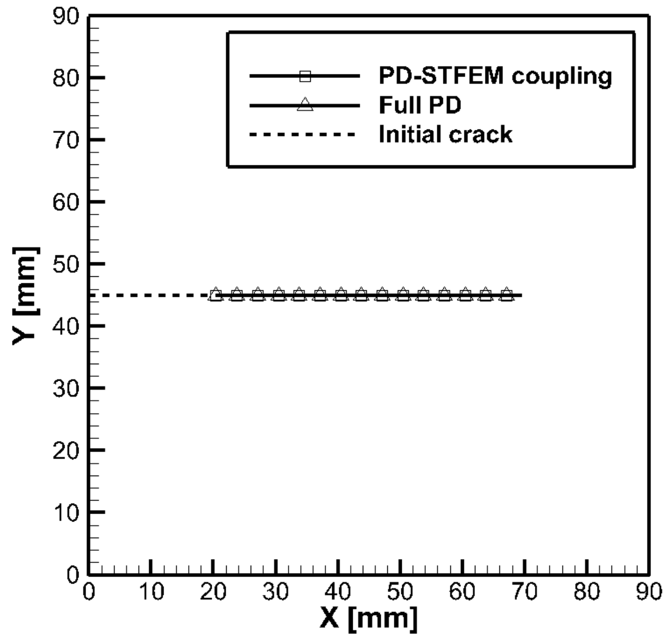

Figure 48. Crack path of mode I.

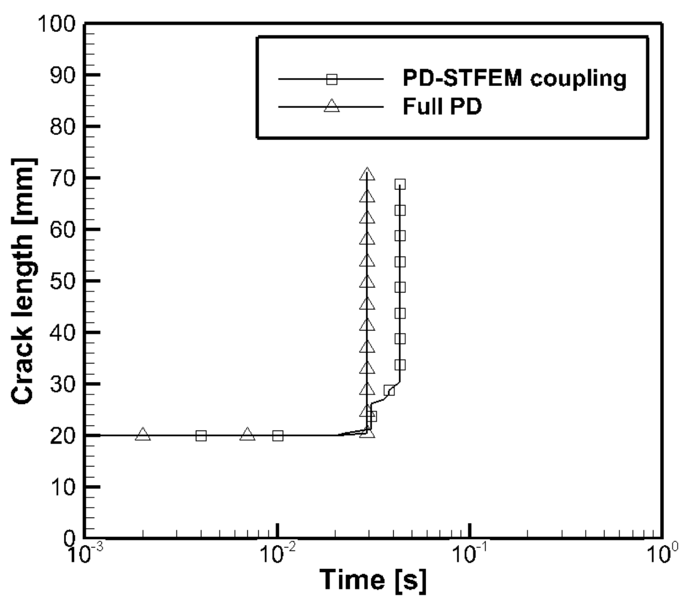

Figure 49. Crack length history of mode I.

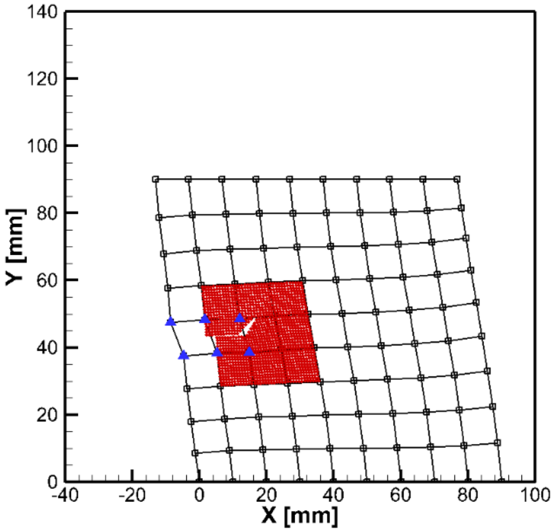

(a) $t = 0.056704\left[\mathrm{s}\right]$.

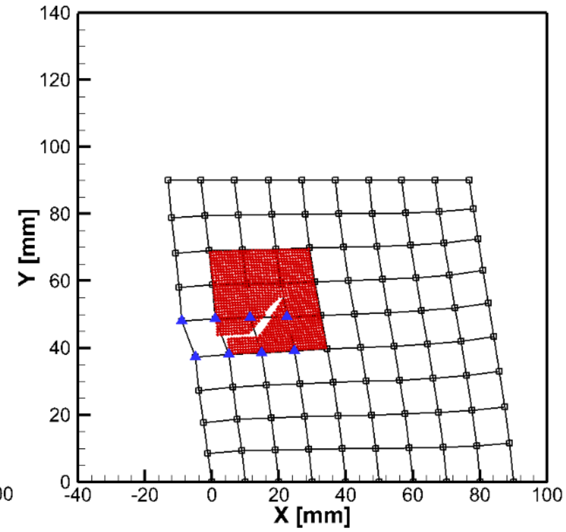

(b) $t = 0.056712\left[\mathrm{s}\right]$.

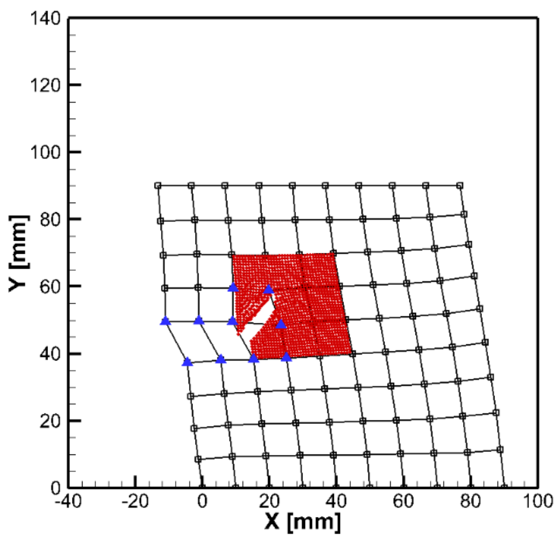

(c) $t = 0.056716\left[\mathrm{s}\right]$.

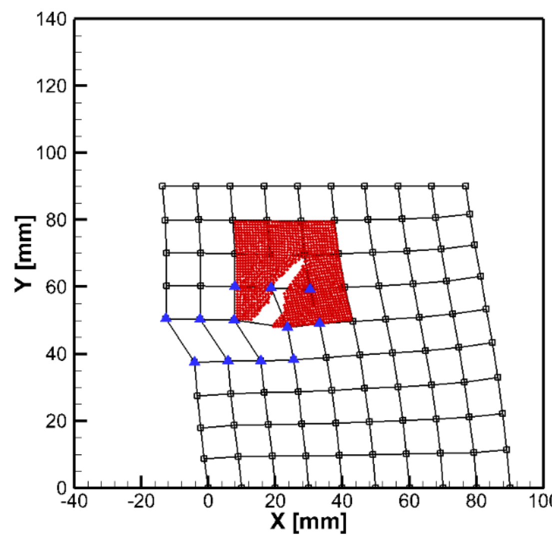

(d) $t = 0.056723\left[\mathrm{s}\right]$.

Figure 50. Crack propagation of coupling simulation of mode II (displacement scaling factor is 500).

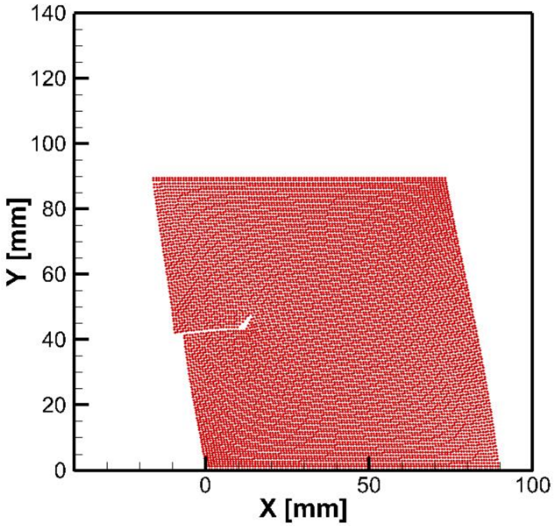

(a) $t = 0.071176\,[\mathrm{s}]$.

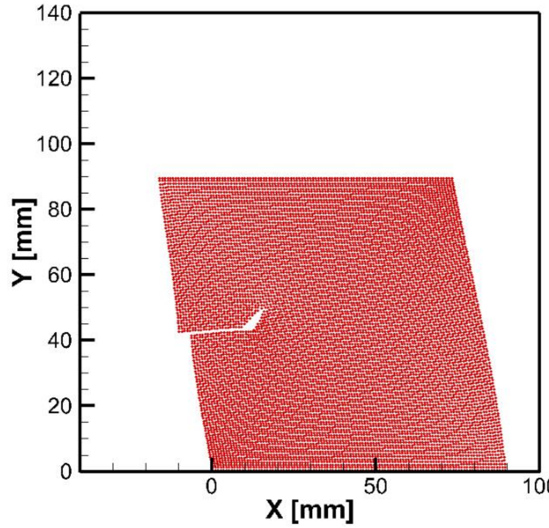

(b) $t = 0.071180\,[\mathrm{s}]$.

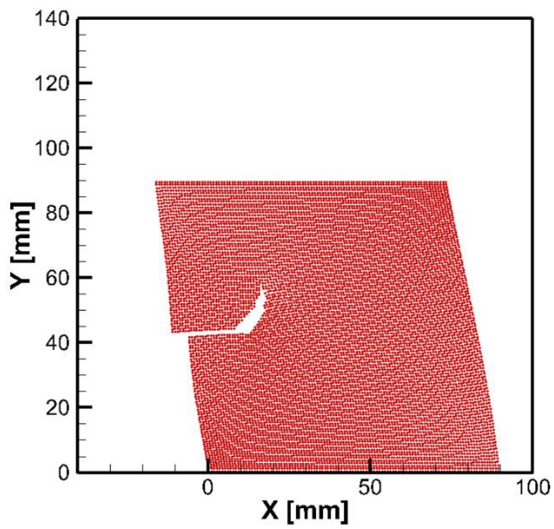

(c) $t = 0.071185\,[\mathrm{s}]$.

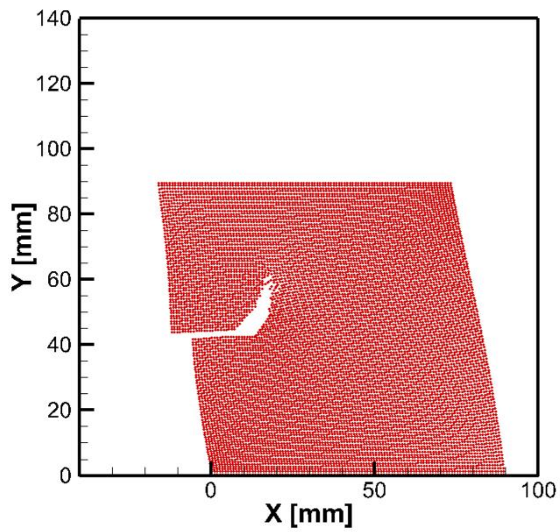

(d) $t = 0.071188\,[\mathrm{s}]$.

Figure 51. Crack propagation of full peridynamics simulation of mode II (displacement scaling factor is 500).

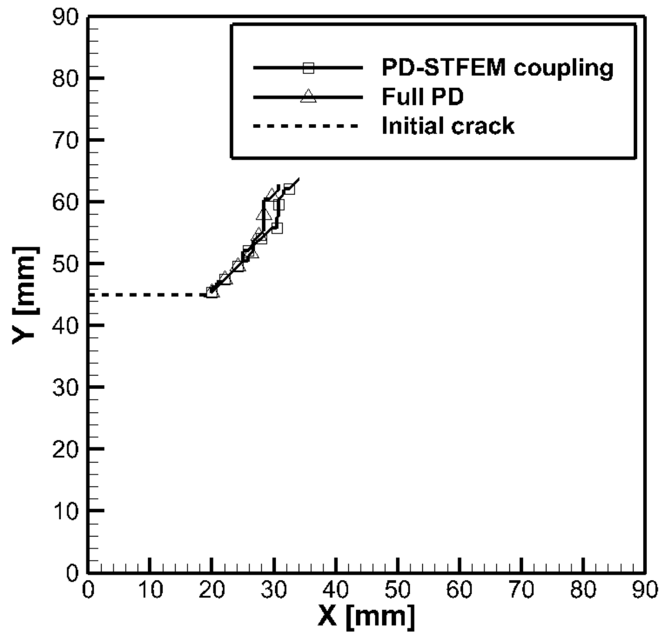

Figure 52. Crack path of mode II.

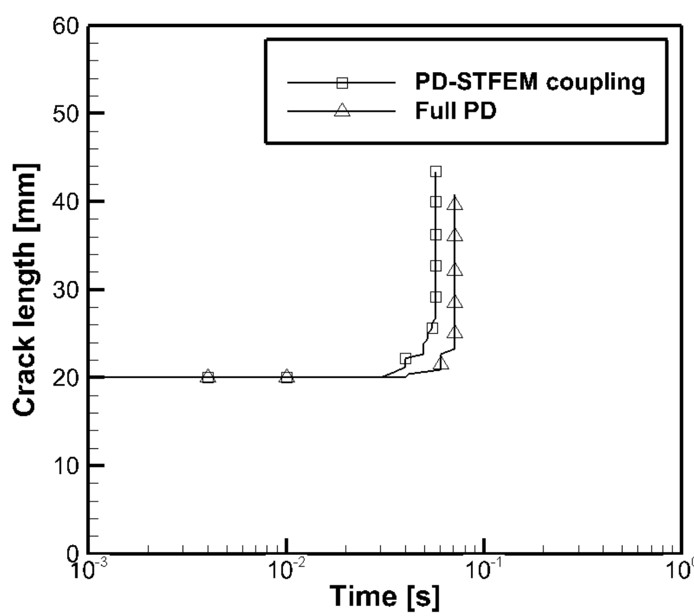

Figure 53. Crack length history of mode II.

6.6 Non-ordinary state-based peridynamics with the time integration based on time discontinuous Galerkin formulation.

6.6.1 1D bar subjected to step loading

In this section, we demonstrate the performance of non-ordinary state-based peridynamics with the time integration based on time discontinuous Galerkin formulation by following the theory shown in section 5.2. The deformation of 1D bar with step loading is simulated. The dimension of the bar and loading condition are shown in Figure 54. The material of the bar is assumed to be linear elastic. The Young' modulus and mass density is given as $E = 200\left[\mathrm{GPa}\right]$ and $\rho = 7860\left[\mathrm{kg/m^3}\right]$. The evenly spaced 101 particles are placed in 1D non-ordinary state-based peridynamics model and the size of horizon is one particle distance. For comparison, the time integration of non-ordinary state-based peridynamics is done by the velocity Verlet and time discontinuous Galerkin formulation. For the velocity Verlet, the time step is determined as $dt = 1.0\times10^{-7}\left[\mathrm{s}\right]$ based on Courant-Friedrichs-Lewy condition [64]. For time discontinuous Galerkin approach, the time step is set as $dt = 1.0\times10^{-6}\left[\mathrm{s}\right]$.

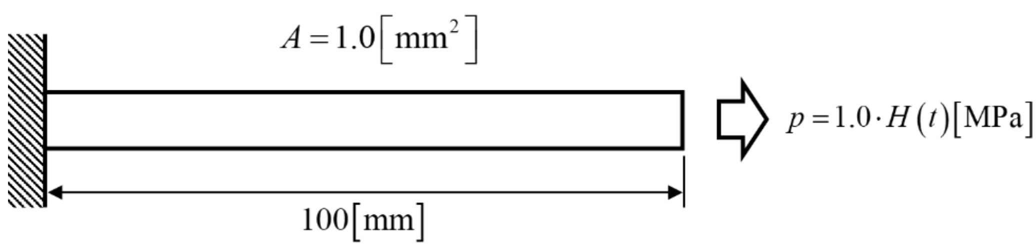

Figure 54. 1D bar subjected to step loading.

The displacement history of the middle point of the bar is shown in Figure 55. The results are compared with the theoretical solution and both results show good agreement. At the peak of the displacement, some oscillation can be observed in both the velocity Verlet and time discontinuous Galerkin method. However, it can be seen that the time discontinuous Galerkin result shows smaller oscillation even it uses larger time increment. Through this simple example, the advantage of the coupling of non-ordinary state-based peridynamics and time discontinuous Galerkin formulation is shown.

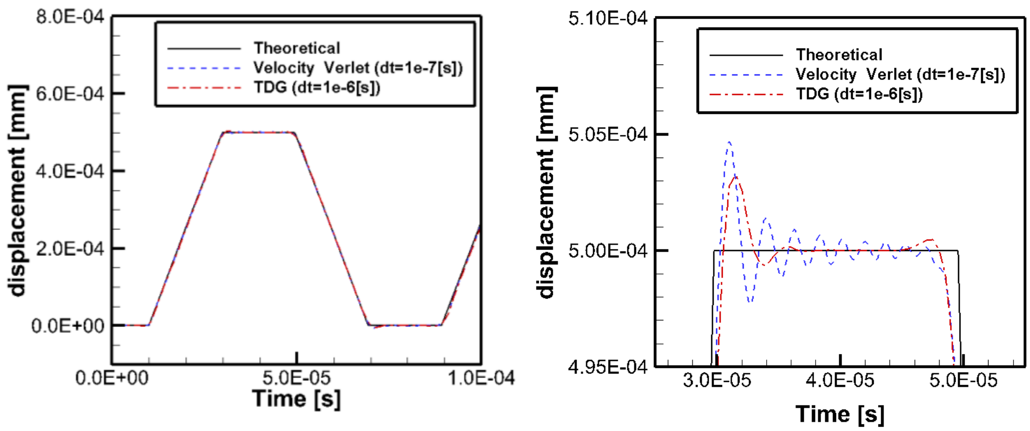

Figure 55. The displacement history at the middle of the bar.

CHAPTER 7

CONCLUSION AND FUTURE WORK

7.1 Conclusion

In summary, this dissertation presents two key contributions to the field of failure prediction in solids. The first is the development of nonlinear space-time FEM based on time discontinuous Galerkin formulation. The second is a multiscale fracture simulation approach established by coupling space-time FEM with non-ordinary state-based peridynamics.

The major goal for developing nonlinear space-time FEM is to capture failure and responses in nonlinear solids. After an outline of the formulation, its robustness is demonstrated in the cases of modified Mooney-Rivlin hyperelastic and finite strain viscoelastic constitutive models. Based on these implementations, a computational framework for fatigue life prediction in rubbery material based on the integration of nonlinear space-time FEM employing TDG formulation with continuum damage constitutive model is presented. This development is motivated by the challenge associated with traditional FEM in capturing cyclic failure that is coupled with finite deformation in nonlinear solids. The unique capability of space-time FEM in discretizing in the temporal domain effectively captures the temporal nonlinearities associated with the structure/material response. Coupling with the hyperelastic/CDM constitutive model further ensures that the basic mechanisms of progressive damage evolution due to the cyclic loads are properly accounted for. Verification and validation of the proposed method is carried out via two steps: First of all, comparisons are made to results obtained from both explicit and implicit time integration algorithms that are typically employed in conventional FEM approaches. It has been demonstrated that space-time FEM approach is accurate and employs time step size much larger than those used in explicit time integration. While implicit time integration algorithm is capable of handling time step sizes of the same orders of magnitude, it fails to provide accurate predictions of the nonlinear dynamics response. Furthermore, lack of interpolation in the temporal domain renders both explicit and implicit time integration inappropriate for applications that involve both temporal nonlinearities and large number of load cycles. The second part of the verification and validation focuses on the application to fatigue life predictions in rubbery materials. A CDM model with calibrated material parameters has been established for synthetic rubber based on comparison to the experiments. Life predictions on single notched specimens are modelled with this calibrated damage model and nonlinear space-time FEM. The simulation prediction yields good agreement with the fatigue experiments on single notched specimen of the same configurations. The capability of the method in modeling cyclic failure coupled with both geometric and material nonlinearity is thus demonstrated.

The major goal for coupling space-time FEM with NOPD is to improve the predicative capability for dynamic fracture problems by integrating the multi-temporal scale approximation with a nonlocal meshfree-based approach. More specifically, the NOPD region is prescribed in the neighborhood of a crack tip and debonding from NOPD simulation is used to initiate and propagate the crack. With the evolving crack front, the NOPD simulation region is dynamically adjusted to minimize the computational expense in tracking the crack tip. Based on the NOPD representation of the crack, enrichment function employing discontinuous representations are established for elements that are completely breached by the crack. Numerical performance of the coupling space-time FEM/NOPD simulation is demonstrated through solving crack propagation problems of glass plate with an initial crack for both the mode I and II cracks.

Verification of the numerical result is done by comparing with full peridynamics simulation. It has been shown that the both coupling prediction and full scale peridynamics results agree with each other. The computational cost of multi scale coupling simulation, however, is much less than that of full scale peridynamics.

7.2 Future work

Future efforts are directed towards in several directions: First of all, we propose that the temporal resolutions in nonlinear space-time FEM can be further enhanced by introducing enrichments [39] based on physical insights into the applications. In this work, the enrichment has been applied for hyperelastic constitutive model. This implementation can be extended to damage model and shall further improve the accuracy as well as efficiency in handling applications with large number of load cycles. Secondly, it is well known that failure in many engineering material systems are microstructural sensitive. Therefore, the continuum damage model can be extended to incorporate microstructure mechanisms through either a hierarchical or concurrent multiscale approach to fully capture the multiple length scales that are associated with material failure at extended temporal scale. Finally, the multiscale failure prediction based on coupling space-time FEM with peridynamics can be extended to nonlinear material fatigue problem by combining with nonlinear space-time FEM framework also shown in this work.

REFERENCES

[1] National Highway Traffic Safety Administration, “Two-ply laminate fatigue life of new, field-retrieved, and laboratory-aged light-vehicle tires,” 2013.

[2] W. V Mars and A. Fatemi, “Factors that affect the fatigue life of rubber: a literature survey,” *J. Rubber Chem. Technol.*, vol. 77, no. 3, pp. 391–412, 2004.

[3] W. Mars and A. Fatemi, “A literature survey on fatigue analysis approaches for rubber,” *Int. J. Fatigue*, vol. 24, no. 9, pp. 949–961, 2002.

[4] J. H. Fielding, “Flex life and crystallization of synthetic rubber,” *Ind. Eng. Chem.*, vol. 35, no. 12, pp. 1259–1261, 1943.

[5] A. A. Griffith, “The phenomena of rupture and flow in solids,” *Philos. Trans. R. Soc. london. Ser. A, Contain. Pap. a Math. or Phys. character*, vol. 221, pp. 163–198, 1921.

[6] A. G. Thomas, “Rupture of rubber. V. Cut growth in natural rubber vulcanizates,” *J. Polym. Sci.*, vol. 31, no. 123, pp. 467–480, 1958.

[7] J. R. Rice, “A path independent integral and the approximate analysis of strain concentration by notches and cracks,” *J. Appl. Mechnics, Trans ASME*, vol. 35, pp. 379–386, 1968.

[8] J. Lemaitre, “A continuous damage mechanics model for ductile fracture,” *J. Eng. Mater. Technol.(Trans. ASME)*, vol. 107, pp. 83–89, 1985.

[9] S. Cantournet, R. Desmorat, and J. Besson, “Mullins effect and cyclic stress softening of filled elastomers by internal sliding and friction thermodynamics model,” *Int. J. Solids Struct.*, vol. 46, no. 11–12, pp. 2255–2264, 2009.

[10] J. Lemaitre and R. Desmorat, *Engineering damage mechanics: ductile, creep, fatigue and brittle failures*. Berlin: Springer, 2005.

[11] L. Mullins and N. R. Tobin, “Stress softening in rubber vulcanizates. Part I. Use of a strain amplification factor to describe the elastic behavior of filler-reinforced vulcanized rubber,” *J. Appl. Polym. Sci.*, vol. 9, no. 9, pp. 2993–3009, 1965.

[12] B. Wang, H. Lu, and G. Kim, “A damage model for the fatigue life of elastomeric materials,” *Mech. Mater.*, vol. 34, no. 8, pp. 475–483, 2002.

[13] M. C. Boyce and E. M. Arruda, “Constitutive models of rubber elasticity: a review,” *Rubber Chem. Technol.*, vol. 73, no. 3, pp. 504–523, 2000.

[14] R. S. Rivlin and D. W. Saunders, “Large elastic deformations of isotropic materials. VII. Experiments on the deformation of rubber,” *Math. Phys. Eng. Sci.*, vol. 243, no. 865, pp. 251–288, 1951.

[15] M. Mooney, “A theory of large elastic deformation,” *J. Appl. Phys.*, vol. 11, no. 9, pp. 582–592, 1940.

[16] O. H. Yeoh, “Some forms of the strain energy function for rubber,” *Rubber Chem. Technol.*, vol. 66, no. 5, pp. 754–771, 1993.

[17] R. W. Ogden, “Large deformation isotropic elasticity-on the correlation of theory and experiment for incompressible rubberlike solids,” *Proc. R. Soc. London A Math. Phys. Eng. Sci.*, vol. 326, pp. 565–584, 1972.

[18] R. W. Ogden, *Non-linear elastic deformations*, First ed. New York: Dover Publications, Inc, 1984.

[19] E. M. Arruda and M. C. Boyce, “A three-dimensional constitutive model for the large stretch behavior of rubber elastic materials,” *J. Mech. Phys. Solids*, 1993.

[20] R. W. Ogden, “Volume changes associated with the deformation of rubber-like solids,” *J. Mech. Phys. Solids*, vol. 24, no. 6, pp. 323–338, 1976.

[21] I. Fried and A. R. Johnson, “A note on elastic energy density functions for largely deformed compressible rubber solids,” *Comput. Methods Appl. Mech. Eng.*, vol. 69, no. 1, pp. 53–64, 1988.

[22] SIMULIA, “ABAQUS Theory Manual 6.14.” 2014.

[23] J. C. Simo, “On a fully three-dimensional finite-strain viscoelastic damage model: Formulation and computational aspects,” *Comput. Methods Appl. Mech. Eng.*, vol. 60, no. 2, pp. 153–173, 1987.

[24] J. H. Argyris and D. W. Scharpf, “Finite elements in time and space,” *Nucl. Eng. Des.*, vol. 10, no. 4, pp. 456–464, 1969.

[25] I. Fried, “Finite-element analysis of time-dependent phenomena,” *AIAA J.*, vol. 7, no. 6, pp. 1170–1173, 1969.

[26] J. T. Oden, “A general theory of finite elements. II. Applications,” *Int. J. Numer. Methods Eng.*, vol. 1, no. 3, pp. 247–259, 1969.

[27] W. H. Reed and T. R. Hill, “Triangular mesh methods for the neutron transport equation. Los Alamos: Report LA-UR-73-479,” 1973.

[28] P. Lesaint and P.-A. Raviart, “On a finite element method for solving the neutron transport equation,” in *Mathematical aspects of finite elements in partial differential equations* , de Boor C, Ed. New York: Academic press, 1974.

[29] T. J. R. Hughes and G. M. Hulbert, “Space-time finite element methods for elastodynamics: formulation and error estimates,” *Comput. Methods Appl. Mech. Eng.*, vol. 66, pp. 339–363, 1988.

[30] G. M. Hulbert and T. J. R. Hughes, “Space-time finite element methods for second-order hyperbolic equations,” *Comput. Methods Appl. Mech. Eng.*, vol. 84, no. 3, pp. 327–348, 1990.

[31] G. M. Hulbert, “Time finite element methods for structural dynamics,” *Int. J. Numer. Methods Eng.*, vol. 33, no. September 1990, pp. 307–331, 1992.

[32] T. J. R. Hughes and J. R. Stewart, “A space-time formulation for multiscale phenomena,” *J. Comput. Appl. Math.*, vol. 74, no. 1–2, pp. 217–229, 1996.

[33] X. D. Li and N.-E. Wiberg, “Structural dynamic analysis finite element method by a time-discontinuous Galerkin finite element method,” *Int. J. Numer. Methods Eng.*, vol. 39, no. 12, pp. 2131–2152, 1996.

[34] J. Melenk and I. Babuska, “The partition of unity finite element method: basic theory and applications,” *Comput Methods Appl Mech ENg*, vol. 139, pp. 289–314, 1996.

[35] J. Chessa and T. Belytschko, “Arbitrary discontinuities in space-time finite elements by level sets and X-FEM,” *Int. J. Numer. Methods Eng.*, vol. 61, no. 15, pp. 2595–2614, 2004.

[36] S. U. Chirputkar and D. Qian, “Coupled atomistic/continuum simulation based on extended space-time finite element method,” *CMES*, vol. 24, pp. 185–202, 2008.

[37] D. Qian and S. U. Chirputkar, “Bridging scale simulation of lattice fracture using enriched space-time Finite Element Method,” *Int. J. Numer. Methods Eng.*, 2014.

[38] Y. Yang, S. Chirputkar, D. N. Alpert, T. Eason, S. Spottswood, and D. Qian, “Enriched space-time finite element method: A new paradigm for multiscaling from elastodynamics to molecular dynamics,” *Int. J. Numer. Methods Eng.*, 2012.

[39] S. Bhamare, T. Eason, S. Spottswood, S. R. Mannava, V. K. Vasudevan, and D. Qian, “A multi-temporal scale approach to high cycle fatigue simulation,” *Comput. Mech.*, vol. 53, no. 2, pp. 387–400, 2014.

[40] R. Zhang, L. Wen, S. Naboulsi, T. Eason, V. K. Vasudevan, and D. Qian, “Accelerated multiscale space–time finite element simulation and application to high cycle fatigue life prediction,” *Comput. Mech.*, vol. 58, no. 2, pp. 329–349, 2016.

[41] J.-H. Song, H. Wang, and T. Belytschko, “A comparative study on finite element methods for dynamic fracture,” *Comput Mech*, vol. 42, pp. 239–250, 2008.

[42] X. P. Xu and A. Needleman, “Numerical simulations of fast crack growth in brittle solids,” *J. Mech. Phys. Solids*, 1994.

[43] G. Camacho and M. Ortiz, “Computational modeling of impact damage in brittle materials,” *Int. J. Solids Struct.*, vol. 33, no. 20, pp. 2899–2938, 1996.

[44] T. Belytschko and T. Black, “Elastic crack growth in finite elements with minimal remeshing,” *Int. J. Numer. Meth. Engng*, vol. 45, pp. 601–620, 1999.

[45] N. Moes, J. Dolbow, and T. Belytschko, “A finite element method for crack growth without remeshing,” *Int . J . Numer . Meth . Engng*, vol. 46, pp. 131–150, 1999.

[46] S. A. Silling, “Reformulation of elasticity theory for discontinuities and long-range forces,” *J. Mech. Phys. Solids*, vol. 48, no. 1, pp. 175–209, 2000.

[47] S. A. Silling and E. Askari, “A meshfree method based on the peridynamic model of solid mechanics,” 2005.

[48] S. A. Silling, M. Epton, O. Weckner, J. Xu, and E. Askari, “Peridynamic states and constitutive modeling,” *J. Elast.*, 2007.

[49] B. Kilic and E. Madenci, “Coupling of peridynamic theory and the finite element method,” *J. Mech. Mater. Struct.*, vol. 5, no. 5, 2010.

[50] W. Liu and J. W. Hong, “A coupling approach of discretized peridynamics with finite element method,” *Comput. Methods Appl. Mech. Eng.*, 2012.

[51] T. Belytschko, W. K. Liu, B. Moran, and K. Elkhodary, *Nonlinear finite elements for continua and structures*, 2nd ed. John Wiley & Sons, 2014.

[52] D. Kincaid and W. Cheney, *Numerical Analysis: Mathematics of Scientific Computing*, Third ed. 2002.

[53] Intel, “Intel ® Math Kernel Library Developer Reference (Revision: 082),” 2017.

[54] T. Strouboulis, I. Babuska, and K. Copps, “The design and analysis of the Generalized Finite Element Method,” *Comput. Methods. Appl. Mech. Engrg.*, vol. 181, pp. 43–69, 2000.

[55] M. H. Sadd, *Elasticity -Theory, application, and Numerics*, 3rd ed. Academic Press, 2014.

[56] W. M. Lai, D. H. Rubin, D. Rubin, and E. Krempl, *Introduction to continuum mechanics*, 4th ed. Butterworth-Heinemann, 2009.

[57] L. Kachanov, "Time of the rupture process under creep conditionsle," *Akad. Nauk. SSR. Otd Tekh, Nauk*, vol. 8, pp. 26–31, 1958.

[58] J. Lemaitre, "Evaluation of dissipation and damage in metals submitted to dynamic loading," in *International Conference on the Mechanical Behaviour of Materials*, 1971.

[59] C. Miehe and J. Keck, "Superimposed finite elastic-viscoelastic-plastoelastic stress response with damage in filled rubbery polymers. Experiments, modelling and algorithmic implementation," *J. Mech. Phys. Solids*, vol. 48, no. 2, pp. 323–365, 2000.

[60] J. Lemaitre, J. P. Sermage, and R. Desmorat, "A two scale damage concept applied to fatigue," *Int. J. Fract.*, vol. 97, pp. 67–81, 1999.

[61] J. Lemaitre and I. Doghri, "Damage 90: a post processor for crack initiation," *Comput. Methods Appl. Mech. Eng.*, vol. 115, pp. 197–232, 1994.

[62] T. L. Warren, S. A. Silling, A. Askari, O. Weckner, M. A. Epton, and J. Xu, "A non-ordinary state-based peridynamic method to model solid material deformation and fracture," *Int. J. Solids Struct.*, vol. 46, no. 5, pp. 1186–1195, 2009.

[63] C. T. Wu, "Kinematic constraints in the state-based peridynamics with mixed local/nonlocal gradient approximations," *Comput. Mech.*, 2014.

[64] R. Courant, K. Friedrichs, and H. Lewy, "Über die partiellen Differenzengleichungen der mathematischen Physik," *Math. Ann.*, vol. 100, no. 1, pp. 32–74, 1928.

[65] D. J. Littlewood, "Simulation of dynamic fracture using peridynamics, finite element modeling, and contact," in *IMECE 2010*, 2010.

[66] C. T. Wu and B. Ren, "A stabilized non-ordinary state-based peridynamics for the nonlocal ductile material failure analysis in metal machining process," *Comput. Methods Appl. Mech. Eng.*, 2015.

[67] M. S. Breitenfeld, P. H. Geubelle, O. Weckner, and S. A. Silling, "Non-ordinary state-based peridynamic analysis of stationary crack problems," *Comput. Methods Appl. Mech. Eng.*, 2014.

[68] S. A. Silling, "Stability of peridynamic correspondence material models and their particle discretizations," *Comput. Methods Appl. Mech. Eng.*, vol. 322, pp. 42–57, 2017.

[69] F. Bobaru, J. T. Foster, P. H. Geubelle, and S. A. Silling, *Handbook of peridynamic modeling*. CRC Press, 2016.

[70] E. Madenci and Erkan Oterkus, *Peridynamic theory and its applications*. New York: Springer, 2014.

[71] T. P. Fries and T. Belytschko, “The extended/generalized finite element method: An overview of the method and its applications,” *Int. J. Numer. Methods Eng.*, vol. 84, pp. 253–304, 2010.

[72] Y. Chandra, I. Stanciulescu, L. N. Virgin, T. G. Eason, and S. M. Spottswood, “A numerical investigation of snap-through in a shallow arch-like model,” *J. Sound Vib.*, vol. 332, no. 10, pp. 2532–2548, 2013.

[73] X. Wang and S. Tang, “Matching boundary conditions for diatomic chains,” *Comput. Mech.*, vol. 46, no. 6, pp. 813–826, 2010.

[74] X. Wang and S. Tang, “Matching boundary conditions for lattice dynamics,” *Int. J. Numer. Methods Eng.*, vol. 93, no. 12, pp. 1255–1285, 2013.

[75] R. A. Wildman and G. A. Gazonas, “A perfectly matched layer for peridynamics in two dimensions,” *J. Mech. Mater. Struct.*, vol. 7, no. 8–9, pp. 765–781, 2012.

BIOGRAPHICAL SKETCH

Shogo Wada obtained his BS degree in Mechanical Engineering in 2007 from Tokyo Institute of Technology in Japan. He continued his studies at Tokyo Institute of Technology and received his MS in 2009. After his graduation, he was hired as a staff engineer for a Japanese tire manufacturer, Bridgestone Corporation. He was responsible for tire durability. After working there for five years, he received a Bridgestone scholarship and started PhD course work in Mechanical Engineering at The University of Texas at Dallas in 2014.

CURRICULUM VITAE

Shogo Wada

sxw141830@utdallas.edu

EDUCATION:

M.S. Mechanical Engineering, 2009, Tokyo Institute of Technology, Tokyo, Japan

B.S. Mechanical Engineering, 2007, Tokyo Institute of Technology, Tokyo, Japan

EXPERIENCE:

2009-2014 Staff engineer, Tire Research Department, BRIDGESTONE Co., Tokyo, Japan

HONORS RECEIVED:

2015-2016 The Louis Beecherl, Jr. Graduate Fellowship,

The University of Texas at Dallas, Richardson, TX

RESEARCH INTERESTS:

- Computational and experimental solid mechanics.
- Linear and nonlinear finite element method.
- Failure and fatigue analysis.

PUBLICATIONS AND CONFERENCE PROCEEDINGS

[1] Wakako ARAKI, Shogo WADA, Jun IIJIMA, Tadaharu ADACHI, Yoshihiro ARAI, "Elastic Modulus of Sol-Gel Silica Glass: Porosity and Skelton Character", Abstracts of XV International Sol-Gel Conference, (2009), p.370.

[2] Wakako ARAKI, Shogo WADA, Tadaharu ADACHI, "Viscoelasticity of Epoxy Resin/Silica Hybrid Materials with an Acid Anhydride Agent", Journal of Applied Polymer Science, Vol.108 (2008), pp.2421-2427.

[3] Wakako ARAKI, Shogo WADA, Tadaharu ADACHI, "Morphology and Viscoelasticity of Hybrid Nanocomposites Prepared via Sol-Gel Process", Proceedings of the US-Japan Conference on Composite Materials 2008, (2008), p.NAN-7-1-NAN-7-6.